UNIVERSITY OF
BIRMINGHAM

EFFECT OF SENSITISATION ON THE CORROSION FATIGUE PROPERTIES OF AA5456-H116

James Gunson

A thesis submitted to university of Birmingham for the degree of

Masters of Research (MRes)

Materials and Metallurgy
University of Birmingham
September 2010

Acknowledgments

Special thanks go to Dr. Brian. J. Connolly for all his help and guidance in completing this study.

I would also like to acknowledge Chris Cooper and Richard Doyle for their support during my experimentation.

I am also very grateful to Dave Price for his help and maintenance of the Dartec Fatigue testing machine.

Finally I would like to thank ALCOA for providing me with the material.

Abstract

The marine environment is highly aggressive towards most materials. However, the service life of aluminium in such aggressive marine environments can be exceptionally long. Aluminium sheets and plates of the Aluminium-Magnesium (5xxx) series are extensively used in naval structures. This is due to its good mechanical strength, formability, seawater corrosion resistance, and weldability. However, susceptibility to intergranular corrosion (IGC) and stress corrosion cracking (SCC) of 5xxx alloys with greater than 3wt.% of magnesium alloys can and does occur after prolonged thermal exposure to elevated temperatures, similar to those that occur in service. Various studies have shown that 'sensitisation' causes the formation and coarsening of electrochemically reactive β-phase at the grain boundaries, due to magnesium segregation, and that it does indeed cause the matrix to become susceptible to IGC. However, there has been little to no examination as to the effects of this grain boundary precipitation and the resultant corrosion susceptibility on the fatigue lifetimes of Al-Mg alloys.

To establish the effects of sensitisation on the properties of AA5456-H116 standardised testing in the form of nitric acid mass loss testing (NAMLT) and electrochemical evaluation to confirm the increase in IGC and localised corrosion susceptibility as a result of increased precipitation of reactive β-phase at grain boundaries. The microstructure was also characterised metallographically, to observe grain boundary precipitation and the effects of sensitisation time. It was observed that increasing sensitisation time at 150^{o}C lead to an increase in β-phase precipitation and resultant decrease in IGC and localised corrosion susceptibility.

In order to characterise the effects of sensitisation on the fatigue properties of pre-corroded AA5456-H116, S-N curves were generated and a systematic fractrographical analysis or fractured samples was undertaken. A decrease in fatigue lifetime as sensitisation time at 150^{o}C increased was shown. A complete examination of pit morphology using various microscopic techniques in order to investigate more clearly the morphology of pit that is likely to cause failure before that what is normal fatigue lifetime for as-received AA5456-H116. It was observed that there is an increase in the size, depth and density of pitting with more IGC present on and beneath the surface.

Increased sensitisation time at 150^{o}C effectively renders the microstructure of AA5456-H116 susceptible to IGC and localised corrosion (in the form of pitting), which in turn modifies the local stress and ultimately shortens the fatigue life and lowers the threshold stress for crack initiation and propagation.

Table of Contents

1. Introduction

This thesis sets out to investigate the relationship between sensitisation and corrosion fatigue properties of Al-Mg alloys, specifically AA5456-H116. In order to do this it is important to firstly outline the properties of aluminium-magnesium, and the effects of heat treatment and environment on the properties.

Chapter 2.2 will look at the mechanisms of segregation which involves the movement of Magnesium to grain boundaries. Chapter 2.3 investigates the factors affecting sensitisation, in particular the time and temperature at which documentable grain boundary precipitation of β-phase has occurred. Chapter 2.4 reviews the precipitation kinetics of Aluminium-Magnesium alloys and more specifically precipitation at grain boundaries. Chapter 2.5 will give an overview as to the corrosion properties both prior to sensitisation and how they are affected after sensitisation. In particularly pitting mechanisms and inter-granular corrosion of Al-Mg alloys will be examined. Finally, Chapter 2.6 and 2.7 will underline the fatigue and corrosion fatigue properties of both Al-alloys and more specifically 5xxx series alloy. Included is a review of how pitting corrosion in Al-alloys can lead to crack initiation and a reduction in fatigue lifetime.

The literature review will provide a detailed outline as to the current understanding of the effects of sensitisation on the properties of Al-Mg alloys, this will show the need to characterise specifically the pit morphology and the fatigue lifetimes of AA5456-H116 after sensitisation.

Chapter 3 will outline in detail the experimental work undertaken in this thesis. This section will present the material composition and the perspective sensitisation treatments. Also summarised are the material preparation and the test conditions for microstructural characterisation. The fatigue test matrix and the immersion testing conditions are also presented.

Chapter 4 presents and discusses all of the results obtained from the experimentation. Chapter 4.1 looks at the micro-structural characterisation, including investigating the microstructure in the as-received condition and the hardness of AA5456-H116 as a function of sensitisation time. Chapter 4.2 presents evidence of enhanced susceptibility to corrosion with increasing sensitisation time. Along with nitric acid mass loss testing and phosphoric acid etching the electrochemical behaviour serves to present conclusive evidence as to the relationship between sensitisation and the corrosion properties of

AA5456. Lastly, chapter 4.2 contains the results of optical pit documentation after sensitisation and immersion. Chapter 4.3 serves to document the results of fatigue testing of sensitised and immersed AA5456. Wöhler diagrams are presented, to document the fatigue lifetime, while fractographic analysis of the fracture surface attempts to understand the mechanisms of failure and the effect of sensitisation on the corrosion fatigue properties. Finally, chapter 4.4 shows the morphology of pits selected on the basis of their depth in correlation with those observed in chapter 4.3. Through confocal laser scanning microscopy and cross section analysis the pits can be fully characterised and the mechanisms for crack initiation understood.

Chapter 5 summarises the results and presents the conclusions from the thesis, explaining the effect of sensitisation on the corrosion fatigue properties of AA5456-H116.

2. Literature Review

2.1 Introduction to Aluminium-Magnesium Alloys

Aluminium Magnesium (Al-Mg) alloys are a widely used series of wrought non-heat treatable aluminium alloys. Strengthening is achieved mostly by solution hardening by retaining magnesium in solid solution, dispersoid hardening and strain hardening, most commonly cold working. Fully work-hardened 5xxx series alloys can achieve the uppermost strength possible in aluminium alloys (without precipitation hardening) [1], with yield strengths exceeding 300MPa and tensile strengths close to 500 MPa [2]. Figure 2.1 shows the effect of increase in wt.% of magnesium in solid solution (up to 4.5wt. %), on the properties of Al-Mg Alloy. As a result of their good mechanical properties, high corrosion resistance and desirable weldability, Al-Mg alloys find a wide variety of applications from beverage cans to high-speed ship hulls.

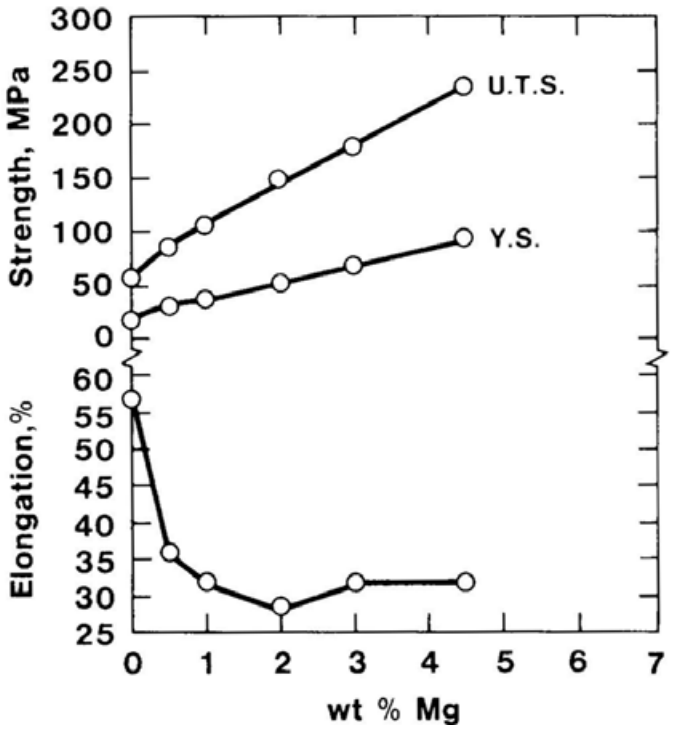

Figure 2.1 Effect of Magnesium in solid solution on the properties of Al-Mg Alloy [1]

Commercial content of magnesium ranges from 0.5 to 12wt. % [2], the higher the magnesium content the higher the strength and formability of the alloy. Magnesium has a high solid solubility in aluminium, up

to 15.35 wt. % at 451 ºC (binary eutectic temperature). However, the rate of solid solubility decreases rapidly with decreasing temperature (approximately 1.7% at room temperature[3]). This drop in solubility results in the precipitation of β-phase from the α solid solution. Furthermore, the rate of this decomposition of the super saturated solid solution (SSSS) is very slow at room temperature. High levels of cold work and exposures to elevated temperatures are known to increase this precipitation process. Precipitates nucleate preferentially on grain boundaries, then at dislocations and finally throughout the aluminium bulk matrix. The binary equilibrium phase diagram for Al-Mg is shown in Figure 2.2. Alloys in the 5xxx series all contain different additions (between 0.1 – 2 wt%) of a variety of elements including, silicon, iron, copper, manganese and chromium.

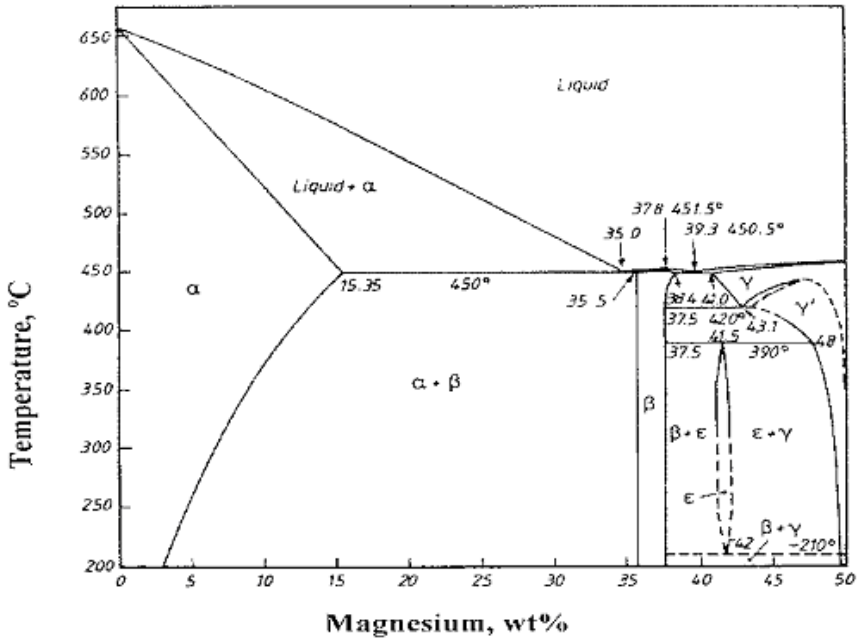

Figure 2.2 Aluminium Magnesium binary equilibrium phase diagram [3]

Solute atoms such as magnesium can also have a significant effect on the work hardening behaviour of an alloy. Schmidt and Miller[4] suggested that solute atoms can improve work hardening by a number of possible mechanisms; those which apply to Al-Mg alloys include, decreasing the rate of recovery, increasing the rate of dislocation multiplication and improving the efficiency of dislocations as barriers to ion flow, therefore improving strength.

Strengthening of Al-Mg alloys is mainly achieved via work hardening, particularly in the form of H116 and H32 tempers. Deformation causes the dislocation content of the metal to increase, and when dislocation generation and multiplication occur faster than annihilation by dynamic recovery, dense

dislocation ‘tangles’ are formed. This reduces the mean free dislocation slip distance, thus giving increased strength[1]. Cold working is particularly effective at increasing strength, since recovery processes are thermally activated. However, increases in strength are only gained at the expense of formability.

2.2 Segregation in Aluminium-Magnesium Alloys

The process of segregation achieves either solute depletion or enrichment in the region of grain boundaries. This local element alteration can have a pronounced affect on an alloy's properties. Magnesium segregation to grain boundaries in Al-Mg alloys makes them highly vulnerable to inter-granular corrosion (IGC) and associated stress corrosion cracking (SCC) [5-8].

2.2.1 Segregation Mechanisms and Observations

Two main mechanisms have been proposed to explain the movement of impurity atoms to grain boundaries; equilibrium segregation and non-equilibrium segregation[9-12]. Within the literature both mechanisms have been applied to the segregation of Magnesium in Al-Mg alloys.

Equilibrium segregation indicates that the process of segregation has reached thermodynamic equilibrium. This process consists of solute incoherent atoms segregating to grain boundaries or the surface in accordance with the statistics of thermodynamics (every microscopic process is balanced by its opposite) in order to reduce the overall free energy of the entire system[9]. In crystalline materials equilibrium segregation is limited to a narrow region, which is restricted by the elastic strain field of the grain boundary, and will vary with grain boundary type[11]. A mono-layer of impurity atoms would be expected to form if enough impurity was present and sufficient energy was introduced. Below the solvus temperature segregation is limited by a decrease in the rate of diffusion. Magnesium is confined to precipitation; therefore it is unable to segregate to grain boundaries.

The equilibrium theory fails to predict segregation for many binary alloys that are thought to undergo equilibrium segregation, which led to the development of a non-equilibrium segregation mechanism [10]. This theory is associated with a concentration gradient for vacancies between the grain centres and boundaries being established [13]. If an alloy undergoes a heat-treatment where non-equilibrium conditions are produced, in particular quenching, then vacancy concentrations can vary in different regions of the microstructure. Grain boundaries are effective vacancy sinks that contribute to a low vacancy concentration; at the same time the grain interiors remain super saturated with vacancies. The resultant concentration gradient leads to vacancy migration towards grain boundaries. Solute enrichment or solute segregation is a direct result of this vacancy migration, as some solute (impurity) atoms within vacancies are dragged towards grain boundaries [12]. In 5xxx series alloys, this concentration gradient may cause Magnesium atoms to be dragged to boundaries via vacancy migration.

Magnesium segregation in 5xxx and 7xxx series alloys that have been rapidly quenched to prevent grain boundary precipitation have been studied using electron energy loss measurements (EELS). Both Cundy et al.[14] for an Al- 7w.t% Mg alloy solution heat-treated at 540 ºC and Doig and Edington [15] for an Al-5.2Zn–3.2Mg alloy solution heat-treated at 500 ºC observed broad segregation bands (approximately 100-200nm) on both sides of the grain boundary. Interestingly, Cundy et al. only observed this segregation band in the Al-7Mg alloy solution heat treatment (SHT) at 540 ºC and not in the same alloy heated to 350 ºC. It can be assumed that this is probably caused by vacancy drag as a result of the quenching experienced during the SHT [11], thus following the non-equilibrium model of segregation.

Scamans documented a far narrower segregated region while observing magnesium segregation on fracture surfaces caused by gallium liquid metal embrittlement. Using X-ray photo-electron spectroscopy (XPS) it was observed that magnesium segregation reduced as the solution heat treatment temperature was increased from 350 ºC to 550 ºC [16], thus supporting the equilibrium segregation mechanism.

In the as-quenched condition magnesium segregation can only occur as an equilibrium process (favoured at low solution heat treatment temperatures). In contrast non-equilibrium processes occurs at moderately high temperatures. These segregation profiles are established by high temperature heat treatments; however, they are modified by the growth of grain boundary precipitates during ageing or during quenching at slow rates. Work by Vetrano et al.[17] and Jones et al. [5] utilising various experimental techniques, including, XPS, EDS and AES, has shown magnesium enrichment at grain boundaries after various ageing treatments (i.e.175^{o}C for 1, 10, 24, 50, and 100 hrs).

2.3 Precipitation in Al-Mg Alloys

The precipitation sequence of Al-Mg alloys has been comprehensively studied using a variety of techniques [23-25]. The following four stage precipitation sequence has been suggested:

SSSS α → GP Zones → β´´ → β´ → β

where SSSS α is the super saturated solid solution of Mg in Al.

Guinier-Preston (GP) zones are very thin plates (approximately one or two atoms thick) made up of solute rich clusters which are elongated along [100] directions. GP zones have been observed at the beginning of ageing at room temperature up to the critical temperature range between 45 and 50°C, above which GP zones change to form spherical particles β'' that have an $L1_2$ structure. The composition of β'' particles is Al_3Mg. The $L1_2$ structure indicates that the Al and Mg atoms are alternately aligned in 3D periodicity along the [100] directions [23, 25].

Annealing causes the GP zones and the β´´ particles to dissolve forming β´ semi-coherent phase precipitates at around 100°C [24]; β' precipitates possess a hexagonal structure and nucleate at structural heterogeneities such as grain boundaries and vacancies, causing an adjacent solute depleted zone around them [26]. However, there is evidence that despite the presence of vacancies β' precipitates do not actually nucleate at such vacancy type defects (e.g dislocation loops) [27]. Surrounding this solute-depleted zone there is another layer (10 nm), which is vacancy-depleted and in which no precipitation occurs. Recent work has shown that the most crucial hardening is achieved via the formation of these intermediate β´ particles [23]. During the latter stages of aging, at higher temperatures (up to 200°C), Magnesium depletion of the matrix becomes almost complete, and the transformation of β´ precipitates leads to the formation of the stable β phase. Above 250°C β phase forms directly from the decomposition of the Aluminium matrix supersaturated solid solution [28]. Its composition is believed to be largely similar to that of β´ (i.e. Mg_2Al_3) [27].

2.3.1 Grain Boundary Precipitation in 5xxx alloys

In commercial 5xxx alloys there are numerous other alloying elements; most notably, chromium, silicon, iron and manganese. Iron and zirconium are sometimes added to increase the recrystallisation temperature; silicon to improve the fluidity; manganese or chromium to correct for the corroding effect of iron. Copper is added to reduce pitting corrosion by enhancing general corrosion; zinc has little or no effect on corrosion but enhances castability and strength. If iron, iron plus manganese or iron plus chromium is above 1-2% (depending on magnesium content), intermetallic particle of $FeAl_3$, $(FeMn)Al_6$, $(FeMn)_3Si_2Al_{15}$, $(FeCr)Al_7$, or $(FeCr)_4Si_4Al_{13}$ may form. These intermetallics do not have a substantial effect on strength but affect appreciably the formability, fatigue resistance and surface finish. The claim that magnesium additions reduce the size of $FeAl_3$ is doubtful. Silicon usually forms Mg_2Si, mostly insoluble, especially in the alloys with more than 3-4% magnesium. Iron may form Fe_2SiAl_8 in low-magnesium, high-silicon alloys; $FeAl_3$ in the absence of chromium or manganese; $(FeMn)Al_6$ or $(FeMn)_3Si_2Al_{15}$ when manganese is present; $(FeCr)Al_7$ or $(FeCr)_4Si_4Al_{13}$ when chromium is present. Copper has been detected as $CuMgAl_2$ and Cu_2FeAl_7. Zinc is seldom out of solution and then forms $Mg_3Zn_3Al_2$; titanium, boron and beryllium are mostly in solution. Various studies have found the existence of these inter-metallic particles at grain boundaries [17, 29-30].

Grain boundary precipitation of the anodically active β-phase (Mg_2Al_3) has been shown in numerous studies [17, 21, 31-32]. However the amount of β-phase precipitation along grain boundaries differs significantly. For example, Searles observed discontinuous grain boundary β-phase precipitates for AA5083 (Al-4.5wt%Mg) aged in the temperature range 150°C for 82.5 hrs and However, continuous grain boundary β-phase precipitates have been observed for alloys with high Mg contents from 8 to 11 wt% aged in the temperature range 200°C for 2 years [39], most likely due to the length of senstistation.

2.4 Sensitisation of Aluminium-Magnesium Alloys

5xxx series alloys containing more than 3 wt. % Mg can, under certain conditions, form β-phase precipitates, which preferentially decorate the grain boundaries. β-phase has a large lattice parameter (a = 2.824 nm and a unit cell of 1168 atoms) [18]. This form of precipitate can render the microstructure susceptible to IGC if the material is subjected to a corrosive environment. Since this grain boundary precipitate causes the material to be sensitive to corrosion it is often referred to as 'sensitisation'. The degree of susceptibility increases with magnesium content, time and temperature, and amount of cold working. In general there are two ways for sensitisation of Al-Mg alloys to occur. These are sensitisation during processing or sensitisation during service. β-phase is slow to precipitate in fully annealed material; the rate of precipitation is faster for deformed material as the increased dislocation density facilitates the diffusion of Mg [18].

The greatest susceptibility has been associated with alloys that are described as forming continuous precipitates of β-phase along their grain boundaries [18,19] . However, IGC has also been shown to occur in alloys with discrete non-continuous precipitate pathways [6]. Care must be taken when analysing results as many examples within the literature of "continuous" precipitation observed within Al-Mg alloys, have been inferred from optical metallography of etched surfaces [8]. Direct observations using transmission electron microscopy (TEM) of Al alloys with <7 % Mg tend to show discrete particles with extensive strain fields which, can lead to the boundaries appearing to be continuously decorated [5, 20].

β-phase is strongly anodic relative to the Al-Mg matrix (see table 2.1); therefore it corrodes selectively at a rapid rate [21]. It should also be noted that following segregation, the resulting Mg-rich regions have been found to be anodic to the matrix even prior to precipitation [18]. This suggests that visible precipitates may not necessarily be a requirement to create a continuous active pathway at the grain boundaries. Because of this susceptibility to inter-granular attack, combining a damaging environment with the presence of an acting stress of sufficient intensity can cause sensitised material to fail in service through SCC.

Numerous studies[17,19,20-22] have illustrated the effects of time and temperature of heating on the susceptibility of Al-Mg alloys to sensitisation, predominantly using SCC testing (these will be discussed in a later section). Searles et al. utilised constant-extension rate testing (CERT) to look at the degree of sensitisation of various heat-treated samples of AA5083, showed that the measured ductility, while immersed in 3.5% NaCl, depended greatly on the sensitisation time [21]. A minimum ductility was

reached after 189 hours at 150ºC suggesting maximum sensitisation was reached. Times exceeding this showed slight improvements in ductility.

Figure 2.3 shows weight loss (Nitric Acid Mass Lost Testing, NAMLT) data for AA5083 H116 (4.9 wt. % Mg) sensitised at temperatures ranging from 80-200ºC for durations of up to 336hrs[22]. In accordance with ASTM Standard G67-04 [69] samples with weight loss greater than 25 mg/cm^2 are highly susceptible to inter-granular attack. Below 15 mg/cm^2 it can be said that the material is inter-granular resistant. It can be seen that samples heated at 175ºC reach a maximum around 200 hours. As the solvus temperature is approached, a 'continuous', or closely spaced precipitate distribution transforms into coarser randomly distributed precipitates throughout the matrix and grain boundary phases, therefore "stabilising" the alloy [7].

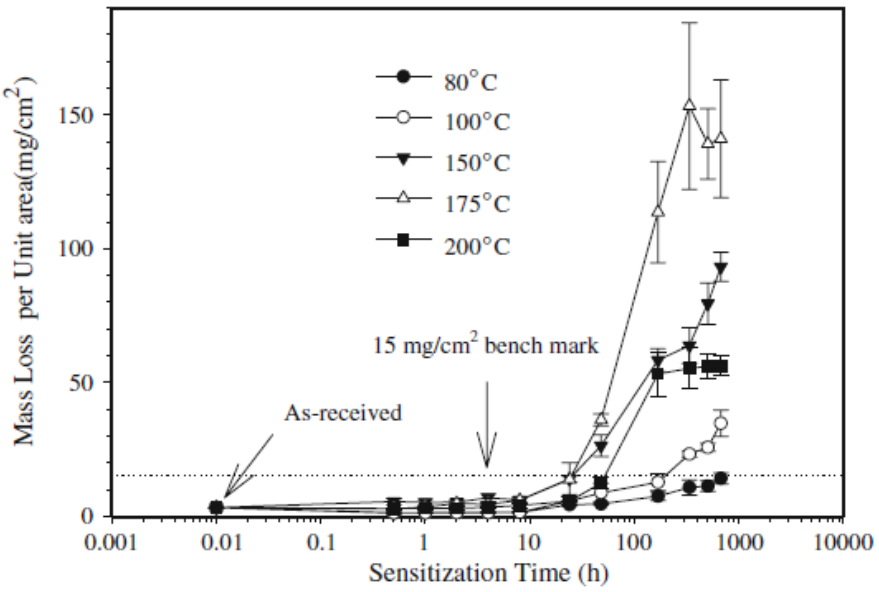

Fig. 2.3 Effect of sensitisation time and temperature on IGC susceptibility of AA5083 H116[22].

2.5 Corrosion of Aluminium Alloys

Aluminium is a highly reactive material that is readily oxidised. However, in practice, it possesses excellent corrosion resistance, due to the formation of a thin, protective oxide film of alumina (Al_2O_3) on its surface, as shown in Equation 2.1.

The oxide film formed on aluminium in air at ambient temperatures is only around 1-5 nm thick [2, 33], and if damaged, re-grows very rapidly. It passivates the aluminium and inhibits corrosion because of it is resistantance to dissolution and effective insulation [34]. An effective insulator prevents electrons produced by oxidation of the metal from reaching the oxide/solution interface, where the cathodic reduction of oxygen (equation 2.2) and water (equation 2.3) can take place. Restricting these cathodic reactions reduces the amount of anodic oxidation of the metal that can occur.

Corrosion of aluminium is an electrochemical process that involves the dissolution of metal atoms; it can only take place once the protective oxide film has been dissolved or damaged. Aluminium's oxide film is stable in neutral conditions, but soluble in acidic (Eq 2.4) and alkaline (Eq 2.5) environments. The stability of aluminium's oxide film is expressed by the potential vs pH diagram [34], as shown in Figure 2.4.

Equation 2.1 Passivation: $2Al_{(s)} + 3H_2O_{(l)} \rightarrow Al_2O_{3(s)} + 6H^+_{(aq)} + 6e^-$

Equation 2.2: Cathodic oxygen reduction: $O_{2(g)} + 2H_2O_{(l)} + 4e^- \rightarrow 4OH^-_{(aq)}$

Equation 2.3: Cathodic water reduction: $2H_2O_{(l)} + 2e^- \rightarrow 2OH^-_{(aq)}$

Equation 2.4: In acidic conditions: $Al_2O_{3(s)} + 6H^+_{(aq)} \rightarrow 2Al^{3+}_{(aq)} + 3H_2O_{(l)}$

Equation 2.5: In alkaline conditions: $Al_2O_{3(s)} + 3H_2O_{(l)} + 2OH^-_{(aq)} \rightarrow 2Al(OH)_4^-{}_{(aq)}$

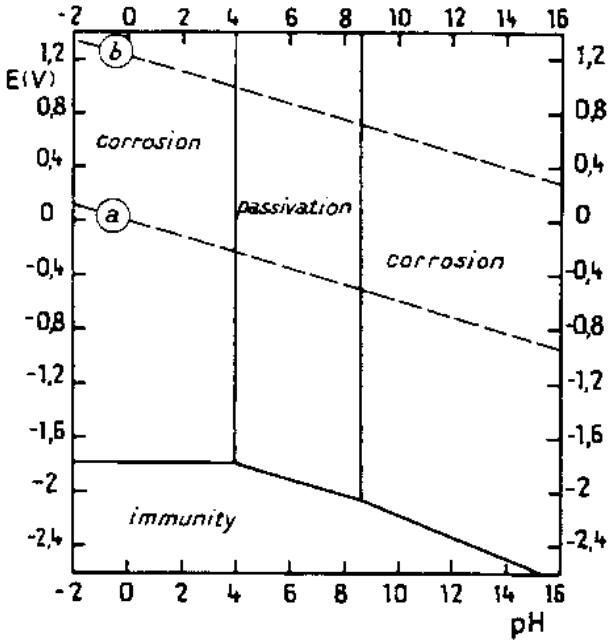

Figure 2.4: Theoretical regions of corrosion, immunity and passivation for aluminium at 25ºC in the presence of water.[34]

Generally, aluminium's protective film is stable in the pH range of 4 - 8.5 (Figure 2.4). Conversely, this range can be altered by the presence of substances that can react with the metal forming soluble complexes or insoluble salts. Once outside the limits of its protective oxide film, aluminium corrodes in aqueous environments, because it is soluble in many acidic and alkaline environments. Corrosion takes place via the following anodic reactions:

Equation 2.6: Dissolution: $Al_{(s)} \rightarrow Al^{3+}_{(aq)} + 3e^-$

Equation 2.7: Hydrolysis: $Al^{3+}_{(aq)} + H_2O_{(l)} \rightarrow AlOH^{2+}_{(aq)} + H^+_{(aq)}$

Equation 2.8: Alkaline dissolution: $Al_{(s)} + 4OH^-_{(aq)} \rightarrow Al(OH)_4^-{}_{(aq)} + 3e^-$

High purity aluminium is highly corrosion resistant; however, it is soft and possesses a very low yield strength [2]. Therefore aluminium is often alloyed with various other elements to improve its mechanical properties. Unfortunately, the presence of such elements, whether alloying additions or impurities, can have a negative effect on the corrosion resistance. The resultant corrosion potential of adding some of these major alloying elements to pure aluminium is shown in Figure 2.5. It can be seen that additions of magnesium and zinc serve to reduce aluminium's corrosion potential, while additions of manganese, copper and silicon result in an increase in solution potential.

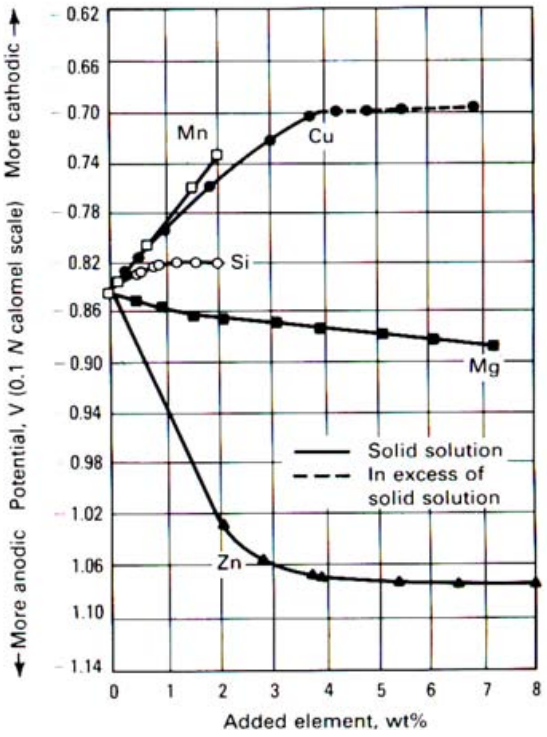

Figure 2.5: Effects of principal alloying elements on the electrolyte-solution potential of aluminium. Potentials are for solution-treated and quenched high-purity binary alloys in a solution of 53g/L NaCl plus 3 g/L H_2O_2 at 25ºC [19].

The equilibrium solubility of many metals in aluminium is very low; therefore alloying additions as well as impurities often form intermetallic particles. These particles have semi conductive oxide films and are therefore more effective sites for the cathodic reactions as opposed to the insulating alumina film of the aluminium matrix. Intermetallic particles can also act as initiation sites for localised corrosion [33, 35-36].

Intermetallic particles that are more electrochemically active than the matrix, such as Al_3Mg_2, $MgZn_2$, and Mg_2Si acts as anodes and undergo dissolution, while particles that are more noble than the aluminium matrix such as Al_3Fe and Al_2Cu act as cathodes. When particles are situated at or adjacent to grain boundaries, inter-granular corrosion can develop. Table 2.1 shows corrosion potentials, in NaCl solution, of various common intermetallic particles present in aluminium alloys. It is clear that the corrosion potential depends on the concentration of chloride anions.

Table 2.1: Corrosion potentials (average values) for intermetallic particles commonly found in aluminium alloys, also including pure metals [37].

Stoichiometry	*Corrosion potential (mV, SCE) in NaCl solutions*		
	0.01M	0.1M	0.6M
Al_3Fe	-493	-539	-566
Al_2Cu	-592	-665	-695
Al_3Zr	-752	-776	-801
Al_6Mn	-839	-779	-913
Mg_2Al_3	-1124	-1013	-1162
$MgZn_2$	-1001	-1029	-1095
Mg_2Si	-1355	-1538	-1536
Al_2CuMg	-956	-883	-1061
Al	-679	-823	-849
Mg	-1601	-1586	-1688
Mn	-1315	-1323	-1318
Si	-450	-441	-452
Cu	-117	-232	-220

2.5.1 Pitting Corrosion of Aluminium

Pitting corrosion is a form of highly localised corrosion occurring on the metal surface. It typically occurs as a process of anodic dissolution, which results in the formation of cavities in an otherwise passive surface. It is generally accepted that the process of pitting should be viewed as two separate stages; initiation and propagation. It is well known that pits can initiate at metallurgical heterogeneities in alloys. However, a number of mechanisms have been put forward to explain the failure of the passive oxide in the presence of aggressive species such as chloride ions. These include penetration, which involves the transport of aggressive anions through the passive film to the metal/oxide interface where dissolution is promoted; absorption, which is based upon oxide thinning occurring locally because of locally adsorbed species that cause the local electric field strength to increase, eventually leading to complete breakdown and the formation of a pit; and finally film breaking with chloride migrating to the metal/oxide interface and forming a metal chloride phase that cracks the overlying oxide as a result of its larger specific volume, the chloride phase then provides a ready source of chloride ions to stabilize pit growth from the very outset of pit development [33].

Figure 2.6 shows the mechanism of pit propagation. Pitting is an autocatalytic process, meaning once a pit begins to propagate the resultant chemistry that is developed in the surrounding area is such that continued pit growth is sustained [33]. Rapid metal dissolution occurs in the presence of chloride ions, producing Al^{3+} (equation 2.6). A localised reduction in pH occurs as a result of hydrolysis (equation 2.7) of Al^{3+} cations, which promotes a further increase in the rate of dissolution. The high cation production of these reactions then causes Cl^- ions to electromigrate into the pit to maintain charge balance within the pit. The acidic chloride environment generated is highly aggressive and serves to further propagate pit growth [33] and prevents repassivation.

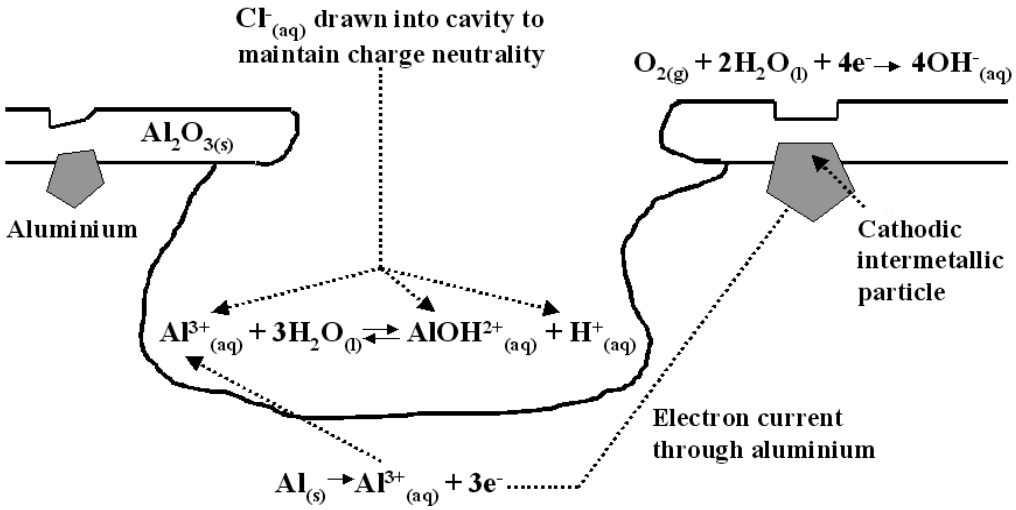

Figure 2.6: Diagram illustrating the mechanism of pitting corrosion in aluminium[68]

2.5.2 Inter-granular Corrosion of Aluminium Alloys

Inter-granular corrosion (IGC) is another form of selective localised attack that develops at grain boundaries. IGC is often considered to be more detrimental than pitting, as it can lead to Stress Corrosion Cracking (SCC) in the presence of stresses. However, it should be noted that resistance to IGC does not always accurately predict an alloy's resistance to SCC [19].

IGC occurs when the anodic reactivity of the grain boundaries or their adjacent areas is greater than that of the grain interiors, usually due to differences in composition. The mechanism and location of this anodically active grain boundary path varies between the different aluminium alloy systems. For example, in 2xxx series alloys, it is the existence of a narrow copper depleted region either side of copper-rich grain boundary phases [19], while in 5xxx series alloys, it is the precipitation of a reactive

grain boundary phase known as β-phase (Mg_2Al_3), that causes IGC susceptibility [6, 21, 33]. In 7xxx series alloys that contain copper, it is copper depleted regions along the grain boundaries that are responsible [38], while in copper-free 7xxx series alloys, it is believed to be the existence of reactive zinc and magnesium precipitates on the grain boundaries that causes IGC. Traditionally, 6xxx series alloys were thought of as being resistant to this type of attack [19], however, when the alloy contains an excessive amount of silicon, inter-granular corrosion increases because of the cathodic nature of the insoluble constituent [39].

2.5.2.1 Evaluation of Inter-granular Corrosion in 5xxx alloys

Visual observations of inter-granular corrosion are generally not particularly reliable for screening tests for susceptibility, probably owing to the long induction time for the development of IGC. For this reason, testing for IGC susceptibility has traditionally relied upon techniques that involve immersion in various acid solutions. ASTM standard G67-04 [69], Nitric Acid Mass Loss Testing (NAMLT), provides a quantitative measure of susceptibility to inter-granular attack of Al-Mg alloys. This technique consists of immersing test samples in concentrated nitric acid at 30ºC for 24 hours and measuring the mass loss per unit area; this NAMLT number then relates to the degree of IGC susceptibility. Relatively continuous precipitation of grain boundary β-phase leads to a preferentially attacked network, in severe cases causing whole grains to detach from the bulk. Grain fall out of this type creates substantial weight losses in the order of 25 to 75 mg cm^{-2}. Samples that lose <15 mg cm^{-2} can be thought of as being resistant to IGC. When β-phase is precipitated in a discrete manner, intermediate levels of weight loss occur [39]. A more basic screening test consists of etching a sample in 10% phosphoric acid for 90 seconds at 60ºC. This technique indicates the most susceptible grain boundaries. Furthermore, etching in this solution has been shown to highlight the presence of anodic β-phase [7, 40].

2.5.2.2 Factors Effecting the IGC Susceptibly of Al-Mg Alloys

According to several theories [8,39], susceptibility to IGC is a prerequisite for susceptibility to SCC and treatment of Al-alloys to improve resistance to SCC often leads to improvements in IGC resistance [39]. Sprowls and Brown [8] documented the relationship between the microstructures of Al-Mg alloys and the associated susceptibility to IGC and SCC (Figure 2.7).

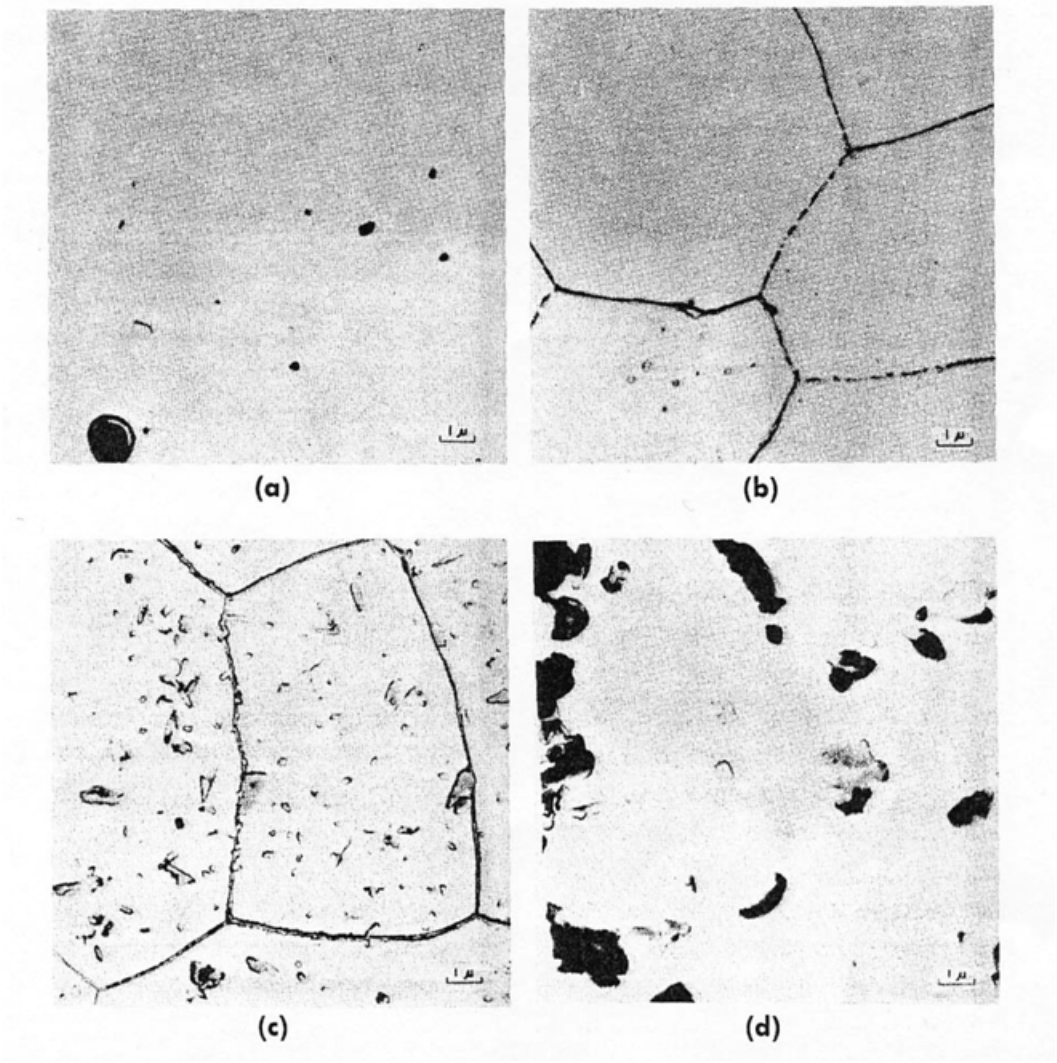

Fig 2.7 Microstructures of alloy 5356-H112 after treatment to produce varying degrees of susceptibility to SCC. (a) cold rolled 20%: highly resistant. (b) cold-rolled 20%, then heated for 1 yr at 100°C; highly susceptible. (c) cold-rolled 20% then heated 1 year at 150°C; slightly susceptible. (d) cold-rolled, then heated 1 year at 205°C; highly resistant.[39]

Figure 2.7 shows four different microstructures in an alloy containing 5% Magnesium. These microstructures represent differing degrees of susceptibility to SCC ranging from highly susceptible to resistant. The treatments that provide high resistance are those that produce microstructures either free of precipitate distributed along grain boundaries (a) or with precipitate distributed evenly within the grains (d). Essentially those that produce IGC resistant microstructures are also highly resistant to SCC; particularly in the latter case as corrosion across boundaries is minimised because the presence of precipitate or depleted regions throughout the microstructure increases the total area of anodic regions to that of cathodic ones, thereby reducing the corrosion current on each anodic region.

Experiments looking at heat-treated AA5182 utilised both phosphoric acid etch response and the NAMLT tests to measure various heat treated samples susceptibility to IGC [41]. It was shown that no clear grain boundary attack occurred in phosphoric acid for the samples with NAMLT values below 20 mg cm^{-2}. In contrast for the sensitised samples with NAMLT values over 24 mg cm^{-2}, the amount of grain boundary attack was found to rise rapidly in correlation with increasing NAMLT numbers. As expected in sensitised samples at a NAMLT of 49 mg cm^{-2}, grain boundary corrosion was very severe and appeared to occur at almost all grain boundaries. The NAMLT results concurred well with the microstructural observations in phosphoric acid etch [41]. Yuan also showed that following subsequent slow strain rate testing (SSRT) to gain SCC data, it was clear that susceptibility of sensitised AA5182 to SCC correlated well with the ASTM [69] NAMLT criteria; when NAMLT values were below 30 mg cm^{-2}, samples were resistant to SCC; and when NAMLT values were above 40 mg cm^{-2}, samples were highly susceptible to SCC. This work clearly highlights the close relationship between NAMLT testing and the more basic phosphoric acid etches tests, and the correlation between these two IGC susceptibility tests and that of true SCC behaviour.

Oguocha et al. [22] showed that the susceptibility of AA5083-H116 to IGC, using NAMLT, increased with sensitisation temperature and time. Susceptibility of AA5083 to IGC at 150 and 175ºC is greater than at 200ºC, thus indicating the existence of a critical sensitisation temperature somewhere between 150 and 200ºC. Various studies have used temperatures of between 150°C and 200°C in order to produce sensitisation [17,20-21,67-68].

There are numerous studies [5, 21, 49-52] and reviews that have investigated the effects of sensitisation on the IGC, SCC and hardness of Al-Mg alloys. However, there is a lack of evidence documenting the relationship between corrosion fatigue behaviour and sensitisation. This study aims to produce conclusive, accurate results that document this relationship.

2.5.3 Stress Corrosion Cracking of Al-Mg alloys

Despite not undertaking any stress corrosion cracking experimentation in this thesis it is important to assess the effects of sensitisation on the stress corrosion cracking susceptibility as many studies have highlighted the effect on various 5xxx series alloys while attempting to understand the effects on susceptibility of IGC. A number of studies [21, 49, 50] have concluded that it is the preferential grain boundary decoration of the anodically reactive precipitate Mg_2Al_3 that forms the susceptible path of attack, similarly to that which makes 5xxx series alloys susceptible to IGC. The studies mentioned have

used similar methods that will be undertaken in this thesis to fully understand and document the relationship between sensitisation and corrosion fatigue (for the mechanisms of SCC see Appendix A.1).

2.5.3.1 Observations of SCC in Al-Mg Alloys

Recently using slow strain rate testing (SSRT) Chang and Chuang [49] showed rapid SCC of sensitised samples of super-plastically formed AA5083SP. This was attributed to the anodic dissolution of a continuous distribution of grain boundary β-phase. A subsequent annealing treatment at 345°C for 1 hour, which removed the continuous nature of the grain boundary β-phase, was found to eliminate this SCC vulnerability. Similarly, Popovic [50] found that a sensitised Al-Mg alloy containing 6.8 wt. % Mg was also susceptible to SCC in SSRT tests. This observation was also attributed to anodic dissolution of the reactive grain boundary β-phase precipitates along the planes of localised deformation.

Further research on sensitised AA5083 supports the anodic dissolution mechanism of SCC. Searles at al. [21] showed that the coverage (observed through TEM analysis) of grain boundaries by anodically active β-phase closely correlated with the strain to failure measured from constant-extension rate tests conducted in 3.5 % NaCl. Furthermore they showed that sensitised AA5083 samples were susceptible to SCC when β-phase was active (at potentials above its breakdown potential), however they were highly resistant to SCC when the β-phase was passive, essentially stopping the anodic dissolution mechanism. Passivity was achieved via selection of a potential (-980 mV SCE) that was known to be slightly below the measured breakdown potential of β-phase (-940 mV SCE). It was observed that under this passive potential control, over 90 % of the ductility was recovered for all samples tested.

A similar study by Jones et al. [6] concluded that crack advance was due to anodic dissolution of β-phase, however they suggested a role of hydrogen induced crack growth when explaining the SCC of grain boundaries that do not shown continuous decoration of β-phase. It was noted that even if hydrogen embrittlement was involved, anodic dissolution of the β-phase was probably needed to provide the corrosion that results in hydrogen reduction.

The rate of anodic dissolution is known to be affected by environmental factors such as aeration, chloride concentration and pH. Therefore it can be argued that monitoring the effect these parameters have on SCC can provide evidence to support the role of anodic dissolution in the SCC of Al-Mg alloys.

2.5.3.2 Effects of Sensitisation on SCC Susceptibility of 5xxx alloys

Al-Mg alloys are candidates for components that require moderate strength, formability, and weldability. Alloy AA5456 is an Al-Mg alloy with a nominal concentration of 5.1 wt % Mg, which meets these goals; however, alloys with greater than about 3 % Mg have shown susceptibility to corrosion and stress corrosion cracking (SCC) following low-temperature heat treatments or thermal exposures. This corrosion and SCC susceptibility have been related to the precipitation of the Mg-rich β phase at grain boundaries of Al-Mg alloys.

Recently, Davenport et al. [51] investigated the IGC and SCC of sensitized AA5182 using (SSRT) and found that the IGC and SCC susceptibility of the alloy depended strongly on sensitisation time and temperature. They also found that the degree of susceptibility to attack for a boundary depended on its crystallographic orientation, with low angle boundaries showing more resistance to attack than their high angle counterpart.

Apart from β phase precipitation, segregation of elemental magnesium to grain boundaries during elevated temperature exposure of Al–Mg alloys has also been observed. Baer et al. [52] showed through Auger Electron Spectroscopy (AES) and TEM that although alloys with magnesium segregation and Al_3Mg_2 precipitates on the grain boundaries were more susceptible to corrosion cracking, the segregated magnesium had little effect on the actual cracking process.

This view was supported by Jones et al. [5] who investigated the role of magnesium in the stress corrosion cracking of an AA5083-H321 alloy using AES and Analytical Electron Microscopy (AEM). They found that elemental magnesium that segregated to grain boundaries did not contribute to SCC of the alloy. Crack–particle interactions during intergranular stress corrosion of AA5083-H321 and Al_3Mg_2 were studied by Jones et al. using electrochemical measurements and TEM. Samples were solution heat treated, quenched, and aged for 100hrs and were tested in both chromate and chromate-free 3.5 wt.% NaCl solution, and the result showed that β phase particles were converted to Al_2O_3 particles on which cracks transversed around. AA5083 alloy with H116 temper is specially rolled to avoid grain boundary precipitation and hence improve the resistance of standard AA5083 to IGC and SCC [53]. However, in spite of this control, it may still be vulnerable to sensitisation when exposed to elevated temperatures for a long time.

2.6 Fatigue of Aluminium Alloys

Fatigue is a form of failure that occurs when a material is subjected to fluctuating/cyclic and dynamic stresses [54]. In general one or more cracks initiate in the material, and these grow until complete failure occurs. Fatigue failure is found after a period of stress or strain cycling where the length of the period is dependent on the load applied. Failure occurs at stress levels lower than the designated ultimate tensile stress, and often, below the yield stress for that material at a static load. Fatigue fracture can be characterised by its catastrophic nature (i.e. the lack of warning provided due to little, if any, gross plastic deformation). The fracture surface is always perpendicular to the direction of applied stress and the failure process begins with the initiation of a crack usually at a point of high stress concentration. Propagation of a crack then advances with each cycle until a critical size is reached [55].

Although disputes exist with respect to a proper definition of crack initiation, it is accepted that a majority of the time is spent on the crack initiation phase in the high cycle fatigue regime. High strength alloys (e.g. 7xxx series) often have small critical flaw sizes and as a result, most of the lifetime of the structures made from these alloys is spent in initiating fatigue cracks. Knowledge and predictions of the crack initiation life are important for the assessment of the fatigue life of a structural component.

Fatigue resistance (i.e. resistance to failure) in 5xxx series alloys increases proportionally to the strength with magnesium content. As in other aluminium alloys, fatigue resistance is very sensitive to testing methods, heterogeneity of the alloy, notches, holes, surface quality, corrosion and atmosphere.

By using a servo-hydraulic fatigue machine to produce a cyclic load in the form of sine waves it is possible to plot a stress-life curve. The amplitude of stress or nominal stress, σ_a or S_a, is commonly plotted versus the number of cycles until failure, N_f, to produce an S-N curve. A group of fatigue tests providing S-N curves may be all run at zero mean stress, or all at some specific non-zero mean stress, σ_m. Also common are S-N curves utilising a constant value of the maximum and minimum applied stress ratio, R. A logarithmic scale is used for the number of cycles to failure because they change rapidly with stress levels and may range over several orders of magnitude.

2.7 Corrosion Fatigue of Aluminium Alloys

Corrosion fatigue is the combination of cyclic loading and corrosion. This is often a problem if a component is cyclically loaded while operating in aggressive environments. Detrimental effects of corrosion on crack initiation and crack growth under fatigue loading depend on the type of material and environment. Systematic effects have been recognised but these effects are not generally applicable to all material/environment combinations. Corrosion fatigue effects are usually associated with the material dissolution at the material surface and at the crack tip. At the material surface it will shorten the crack initiation period and substantially reduce the fatigue limit. At the crack tip this will accelerate crack growth which in addition may be increased by some weakening of the cohesive strength of the material at the crack tip. Corrosion damage of the material surface and noteworthy corrosion pits, can lead to a large reduction of the fatigue limit.

Aluminium alloys like many steels, have relatively low corrosion fatigue strengths [56]. Fatigue strengths of Aluminium alloys are lower in such corrosive environments as seawater and other salt solutions than in air, especially when elevated by low-stress, long duration tests. Corrosive environments produce smaller reductions in fatigue strength in more corrosion resistant alloys such as 5xxx and 6xxx series alloys than in less corrosion resistant alloys (i.e. 2xxx and 7xxx). However, sensitisation of 5xxx series alloys renders them more susceptible to corrosion, therefore decreasing the fatigue strength. Localized corrosion of an aluminium surface, such as pitting or intergranular corrosion, provides stress risers and greatly lowers fatigue life.

Corrosion–fatigue interactions have been modelled by considering corrosion pits as surface cracks whose growth rates are determined by the pitting kinetics [57]. A fatigue crack initiates from the corrosion pit either when the pit grows to a critical size at which the stress intensity factor, ΔK, reaches the threshold for fatigue cracking, ΔK^{th} , or when the fatigue crack growth rate exceeds the pit growth rate [58]. A recent study of the aluminium alloy 2024-T3 has shown that both these criteria are needed for adequately describing the transition from pitting to fatigue crack growth [40]. It should be noted that these investigations are based upon fatigue testing of pristine specimens in a corrosive environment during which fatigue and corrosion damage accumulate simultaneously. Golden et al. [59] have shown that prior corrosion pitting reduced the fatigue strength of aluminium alloys 2024-T3 and 2524-T3 at 10^5 cycles by approximately 40%.

Menzemer et al. [60] studied the influence of environment on the fatigue crack growth of AA5456-H116. They found that fatigue crack growth rates were found to be approximately 3 times greater in

environments of water vapour compared to that in oxygen. Fatigue/fracture surface morphology revealed that the difference in macroscopic material behaviour was reflected well in the local mechanisms governing crack growth through the microstructure. In the oxygen environment, cracks preceded a combination of macroscopic void coalescence, mechanical slip and decohesive rupture. However, in the environment of water vapour, stable crack growth was associated with the formation of ductile and brittle striations.

2.7.1 Pitting Corrosion Leading to Crack Initiation in Aluminium Alloys

Pitting (localised) corrosion leading to fatigue crack initiation and crack growth is considered to be among the most significant damage mechanisms in aging structures [61]. Prior corrosion related fatigue process consists mainly of pitting nucleation, pit growth, transition from pitting to fatigue crack initiation, short crack growth and long crack growth. Pits almost always initiate at a surface heterogeneity, primarily at inclusions and second phase constituent particles. However, they can also occur at flaws, mechanical damage or dislocations clusters [61]. Aluminium alloys contain numerous constituent particles, which play an important role in corrosion pit formation. The presence of localised corrosion pits modifies the local stress and may ultimately shorten the fatigue life and lower the threshold stress for crack initiation and propagation (see Figure 2.8).

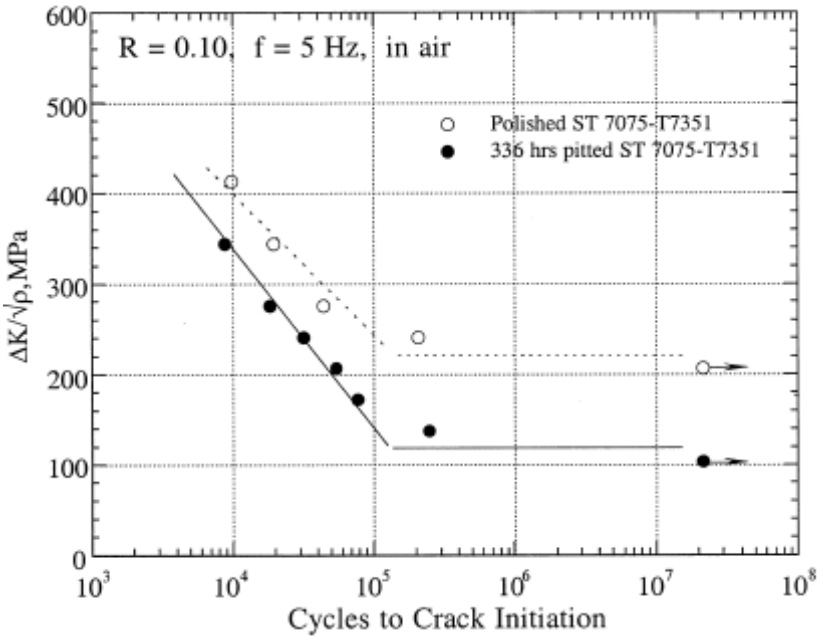

Figure 2.8 Effect of pre-existing corrosion pits on fatigue crack initiation in S-T oriented 7075-T7351 [62]

Even low-levels of pitting corrosion on aluminum structures (7xxx series) resulting from saltwater spray and/or salt fog is the precursor to corrosion fatigue degradation [62]. A number of studies have investigated fatigue performance of aluminium alloys that are susceptible to pitting corrosion [57, 62-63]. Pao et al. reported that pre-existing corrosion pits have an important adverse effect on fatigue crack initiation life. They claimed that corrosion pits were formed by electrochemical reactions between the constituent particles and the surrounding matrix. Sankaran et al. [63] conducted an investigation to evaluate the relationship between the average pit depth and initial crack size, and proposed a model to predict fatigue life. The investigation of high-cycle fatigue regions on 7075-T6 revealed that corrosion pitting accelerates crack initiation and promotes multiple-site damage. They concluded that the effects of pitting corrosion on the fatigue lives of alloys such as 7075 can be related to the effects of equivalent stress concentration factors that are routinely used in structural design. Similarly, DuQuesnay et al. [64] carried out fatigue experiments on pre-corroded aluminium alloy 7075-T6511 plate specimens. They showed that pit depth is the main parameter determining corrosion fatigue life.

Dolley et al. [65] investigated the fatigue life of the 2024-T3 and T4 aluminium alloys was reduced significantly due to the presence of pitting corrosion. Corrosion pits acted as pre-existing flaws in the material to nucleate fatigue cracks. The reduction in fatigue life depended upon the pre-corrosion time and in turn the initial pit size. As longer pre-corrosion times led to deeper initial pits, the fatigue life was reduced significantly as compared to the fatigue life of the un-corroded material. It was evident from post-fracture fractography that all of the fatigue cracks initiated at corrosion pits.

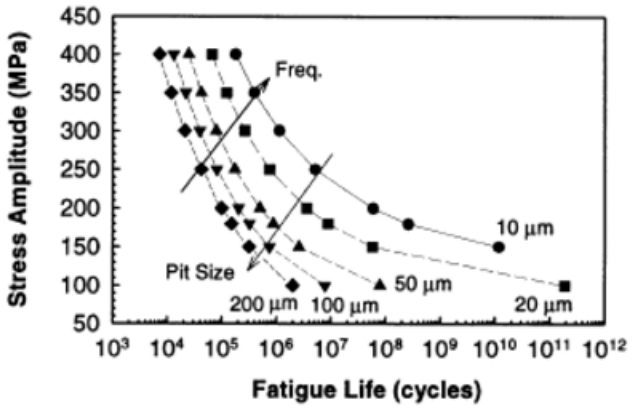

Fig. 2.10 The effect of corrosion pit depth on the fatigue life in 2024-T3 aluminium alloy [65].

Similarly, Jones et al. [66] investigated the interaction between pitting corrosion, grain boundaries, and constituent particles during corrosion fatigue of 7075-T6 aluminium alloy and concluded that some

level of inter-granular attack was always associated with pitting corrosion. The size of a pit relates to the probability of pit-to-crack transition. The shape (surface area and depth) of the pit affects the rate of pit-to-crack transition. Proximity of pits to one another influences the rate of pit-to-crack transition. Characterization of pitting growth rates, as well as pit depths and population distributions, for 2024-T3 and 7075-T6 aluminium alloys was performed. The size of the critical pit (the pit associated with the fatigue crack origin) was usually not the largest pit.

2.8 Aims of Project

There are numerous studies and reviews that have investigated the effects of sensitisation on the IGC, SCC and hardness of Al-Mg alloys. However, there is a lack of evidence documenting the relationship between corrosion fatigue behaviour and sensitisation of 5xxx series, this study aims to research and document this relationship through the use of a number of the techniques discussed in the literature.

After reviewing the literature it appears that there is a need to firstly characterise the microstrucural properties of the material in the form of hardness testing. This will provide a basic understanding whether or not sensitisation affects the mechanical properties of AA5456-H116. Next it is important to characterise the corrosion properties of AA5456-H116. Through the use of a number of techniques already discussed in the literature (i.e. NAMLT), along with electrochemical and immersion techniques, it will be possible to understand the effects of sensitisation have on the corrosion properties, both in terms of susceptibility to pitting and inter-granular corrosion.

Following on from the corrosion properties this thesis will examine the effects of sensitisation, combined with their effects on corrosion susceptibility, on the fatigue properties of AA5456-H116. Fatigue testing will involve both lifecycle analysis and fractographic examination of fatigue surfaces. After reviewing the corrosion fatigue properties of sensitised AA5456-H116 it is important to fully understand the mechanism of failure. This will involve full inspection of pre-fatigued specimens to examine in more detail the typical pit that causes crack initiation. Using confocal laser scanning microscopy (CLSM) to examine the morphology of surface pitting in its more extreme form it is possible to fully characterise the pit depth and area.

3. Experimental Procedure

3.1 Materials

3.1.2 'As received' AA5456-H116

The commercial AA5456-H116 that was used in this work was supplied by ALCOA Technical Centre, USA in the form of rolled plate with a through thickness of 6 mm. The composition of the alloy is given in Table 3.1.

Table 3.1 The composition of alloy AA5456-H116

Composition	Mg	Cu	Mn	Fe	Cr	Si	Zn	Ti	Ni
AA5456 - H116	5.09	0.04	0.66	0.1	0.08	0.07	0.003	0.016	0.003

The H116 temper designation indicates that the alloy has undergone a work hardening only. The designation signifies that the alloy has undergone less than 12% work hardening (or quarter hardening). In addition, this temper condition means that the alloy has not been formerly stabilised, such as a H3 temper would be. However, a degree of stabilisation is achieved through a controlled cooling process (~5°/min) following casting onto a belt.

3.1.3 Heat Treatments

To induce segregation of Mg to grain boundaries and subsequent precipitation of β-phase, different artificial aging treatments were utilised in an attempt to simulate sensitisation. Table 3.3 summarises all the heat-treated condition of AA5456 used in this study, in the order they appear.

Table 3.2: Summary of the heat-treated conditions. In all cases, the heat treatments were performed on AA5456-H116.

Alloy	**Heat Treatment Conditions**			
AA5456-H116	150°C for various times (hours)			
	10	25	50	100

3.2 Sample Preparation

3.2.1 Samples for Metallographic Observation

Specimens of AA5456-H116 were sectioned in the longitudinal (L), long-transverse (T), and short-transverse (S) directions. They were then ground down to a 4000 grade finish with successive grades of SiC paper and mechanically polished down to a 1 μm finish with diamond suspension.

3.2.2 Samples for Nitric Acid Mass Loss Testing (NAMLT)

Samples for NAMLT testing were prepared in accordance with the ASTM standard G67-04 [69]. Samples were cut that were 50 mm (parallel to the longitudinal direction) by 5 mm (transverse direction) and the plate thickness of 6 mm in the short transverse direction. All edges were then smoothed up to 4000 SiC paper and the samples were number engraved. All 3 dimensions were then measured to the nearest 0.02 mm and the total surface area was calculated. Specimens were then fully immersed in 5 % NaOH at 80ºC for 1 minute, then washed and de-smutted in concentrated HNO_3 for 30 seconds. After being allowed to thoroughly dry, the cleaned specimens were weighed to an accuracy of ±0.1 mg. Samples were then immersed in the test solution (see section 3.5.3).

3.2.3 Samples for Localised Corrosion and Electrochemical Measurements

Samples were selected from the heat-treated conditions of AA5456-H116 (see table 3.2). For electrochemical testing the top surface of each heat treated sample was used as the droplet cell test area. All samples that underwent immersion testing were fully submerged and all sides of the material were exposed to localised corrosion. All samples were machined from the same rolled plate, in the same transverse direction with original plate thickness of 6mm. All samples for both electrochemical testing and localised corrosion were polished down to a 1 μm finish using progressively finer SiC paper and diamond paste suspensions (as described previously).

3.2.4 Micro Hardness Testing

Micro hardness profiling was performed using a Mitutoyo MVK-H1 hardness-testing machine; with a load of 50g. 10 measurements were collected at each 2 mm^2 point across the top plate to ensure an accurate representation.

3.3 Evaluation of Inter-granular Corrosion Susceptibility

3.3.1 Nitric Acid Mass Loss Testing

Nitric acid mass loss testing (NAMLT) is a standard method (ASTM G67-04 [69]) for quantitative testing of intergranular corrosion susceptibility of 5xxx series (Al-Mg) alloys. NAMLT comprises of immersing prepared specimens (section 3.2.2) in concentrated nitric acid at 30°C (85 °F) for 24 hours and calculating the mass loss per unit area, as a measure of intergranular susceptibility. According to the standard, if the mass loss is over 25 mg cm^{-2}, the sample will become susceptible to intergranular corrosion, whereas if the mass loss is below 15 mg cm^{-2}, the sample will be resistant to intergranular corrosion. When the mass loss is between 15-25 mg cm^{-2}, a further metallographic examination is advised. The experiments were conducted in duplicate for each heat-treatment condition (see table 3.2) for AA5456-H116.

3.3.2 Phosphoric Acid Etching

Phosphoric acid etching is another method to assess the degree of susceptibility to intergranular corrosion. Samples were prepared according to section 3.2.3. All sides except the top plate were masked using a corrosion resistant stopping lacquer. The sensitised samples were etched in a solution of 10 % phosphoric acid at 60ºC for approximately 90 seconds. Grain boundary etching in this solution has been used as an indication of the presence of the β-phase [7].

3.3.3 Electrochemical Tests - 'Droplet Cell' Potentiodynamic Measurements

The experimental apparatus is similar to a normal 3-electrode cell (such as the conventional electrochemical cell) except, through the use of a capillary, a controlled amount of solution is brought in contact with the metal. For each test, the open circuit potential (OCP) was monitored for 300 seconds and then a potentiodynamic sweep was carried out from the OCP at a rate of 1 mV/s. Anodic and cathodic polarization (vs. Ag/AgCl electrode) tests were performed separately, starting respectively at -10 mV and +10 mV from the OCP. All measurements were carried out in naturally aerated 0.6 M NaCl solution which was acidified to pH 3.5 through dropwise addition of HCl.

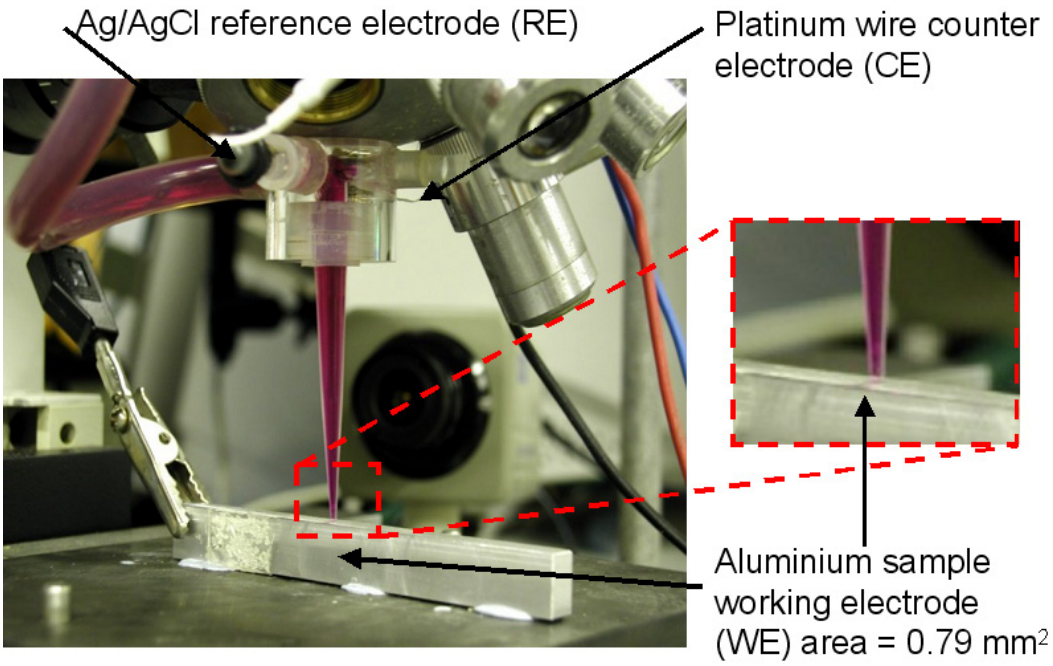

Figure 3.6: 'Droplet cell' electrochemical apparatus for localised (small scale) electrochemical measurements.

3.4 Fatigue Testing

Four point bend fatigue testing, to generate S-N curves, was performed in laboratory air at room temperature, R = 0.1 at 15Hz. Both sides of the sample and the edges were polished to 1 μm, the edges were also rounded to prevent cracks initiating. Samples were prepared in accordance with section 3.2.3 and then rinsed with de-ionised water before fatigue testing. Testing was performed using a hydraulic powered Dartec fatigue testing machine, with a 10 kN load cell and a 4 point bend rig (loading span of 10mm).

The fatigue test matrix included testing:

- The fatigue lifetimes in laboratory air of as received and longest heat treatment of 100 hours at 150^{o}C

- The effects of full immersion pre-exposed for a period of 336 hours in pH 3, 3.5% NaCl on as-received and all heat treated conditions fatigue lifetimes (performed in lab air).

- The effects of an alternate immersion pre-exposed for a period of 336 hours in pH 3, 3.5% NaCl on as –received and all heat treated conditions fatigue lifetimes (performed in lab air).

Three measurements across the specimen length were made of thickness and width, and the averages were used in Equation 4.1 to calculate the desired maximum work load for each specimen:

(3.1)

Where:

f is load (N)
σ is the stress (MPa)
w is the average width of sample (m)
t is the average thickness of sample (m)
a is the distance between middle roller and outside roller

3.5 Evaluation of Pitting Corrosion

3.5.1 Immersion Testing in 3.5% NaCl

Samples were prepared in accordance with section 3.2.3. All full Immersion and alternate tests were performed in naturally aerated conditions 3.5% NaCl acidified to pH3, for 336 hours. The room temperature was recorded at between 23 - 24°C. Pit densities and depth were collected by counting pits and pit depths (using the microscope micrometer) in 1mm^2 areas on the top plate using optical microscopy (see ASTM G46-94 [70]). The information was taken on four randomly selected areas of each heat treated condition as well as alternate and full immersion to provide an average.

3.5.2 Confocal Laser Scanning Microscopy

Confocal Laser Scanning Microscopy (CLSM) was conducted using an Olympus LSM. Full and alternate immersion samples (see section 3.6.1) were ultrasonically cleaned using de-ionised water, and then de-greased using acetone. Particle analysis[1] was performed on three randomly selected areas of pitting on the top plate, to give pit area, surface area and volume along with area ratio, which was calculated using:

(3.2)

Where:

$\mathbf{A_p}$ = Total area of pits (µm)

$\mathbf{A_{total}}$ = 120 x 96 µm

[1] The process of confocal examination involved a step approach whereby the bottom of the pit is selected and scanned to the surface of the pit using a line of sight approach. After a surface/tilt modifier is applied this creates a flatter surface, from which the measurements are taken. Finally, pits are selected using parameters that discount those below 50 pixels in size.

4. Effect of Sensitisation on Properties of AA5456

In this chapter, AA5456-H116 in its as-received condition will firstly be characterised microstructurally. Next, the hardness as a function of sensitisation time will be looked at in order to get an understanding as to the effects on the mechanical properties of AA5456.

Following this, the corrosion behaviour of AA5456-H116 and all of the subsequent heat treatments will be studied in order to determine the effects of sensitisation on corrosion susceptibility. NAMLT testing and phosphoric acid etching will be used to document the relationship between sensitisation and inter-granular corrosion. Micro-electrochemical and immersion techniques will be used to assess resistance to both pitting and IGC.

The following chapter will characterise the effects of sensitisation and subsequent localised corrosion have on the fatigue lifetime of AA5456-H116. By generating Wöhler diagrams the effects of sensitisation on the fatigue lifetime of AA5456-H116 can be documented. Following this the thesis will undertake a detailed fractographic examination of the fracture surfaces of failed specimens in order to understand the mechanisms of failure and investigate the effects of sensitisation time.

The final part of this chapter will focus on the documenting more accurately the extent of corrosion after sensitisation treatment of AA5456-H116. Through the use of confocal laser scanning microscopy it is possible to determine the typical pit morphology (i.e. pit volume, surface area and depth) that results in failure.

4.1 Microstructural Characterisation of AA5456

The AA5456-H116 grain structure is typical of a rolled aluminium product. It appears that along the rolling direction (long-short, L-S) the grains are elongated and more compact. These can be accepted as the high angle grain boundary grains. The size of the elongated grains is 200-300 μm in the T direction and the more equiaxed grains are approximately 10-50 μm in the S-T direction.

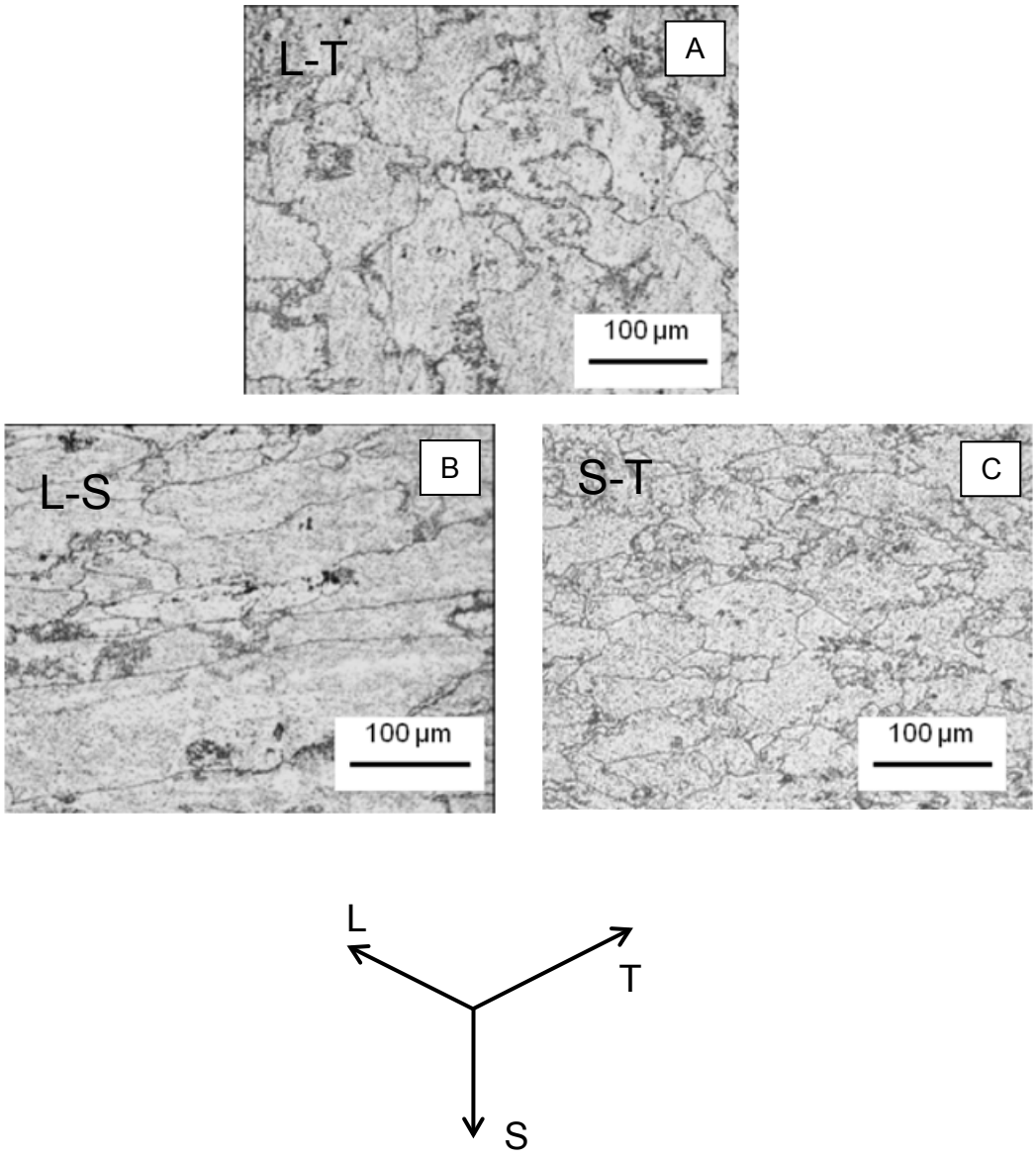

Fig 4.1A,B and C. Showing the microstructure of as-received AA5456-H116 etched in Kellers for 30 seconds.

4.1.2 Micro Hardness Testing

Figure 4.2 shows the variation in the hardness of AA5456-H116 with sensitization time at 150°C. The hardness values, measured along the rolling direction, decreased with increasing sensitization time.

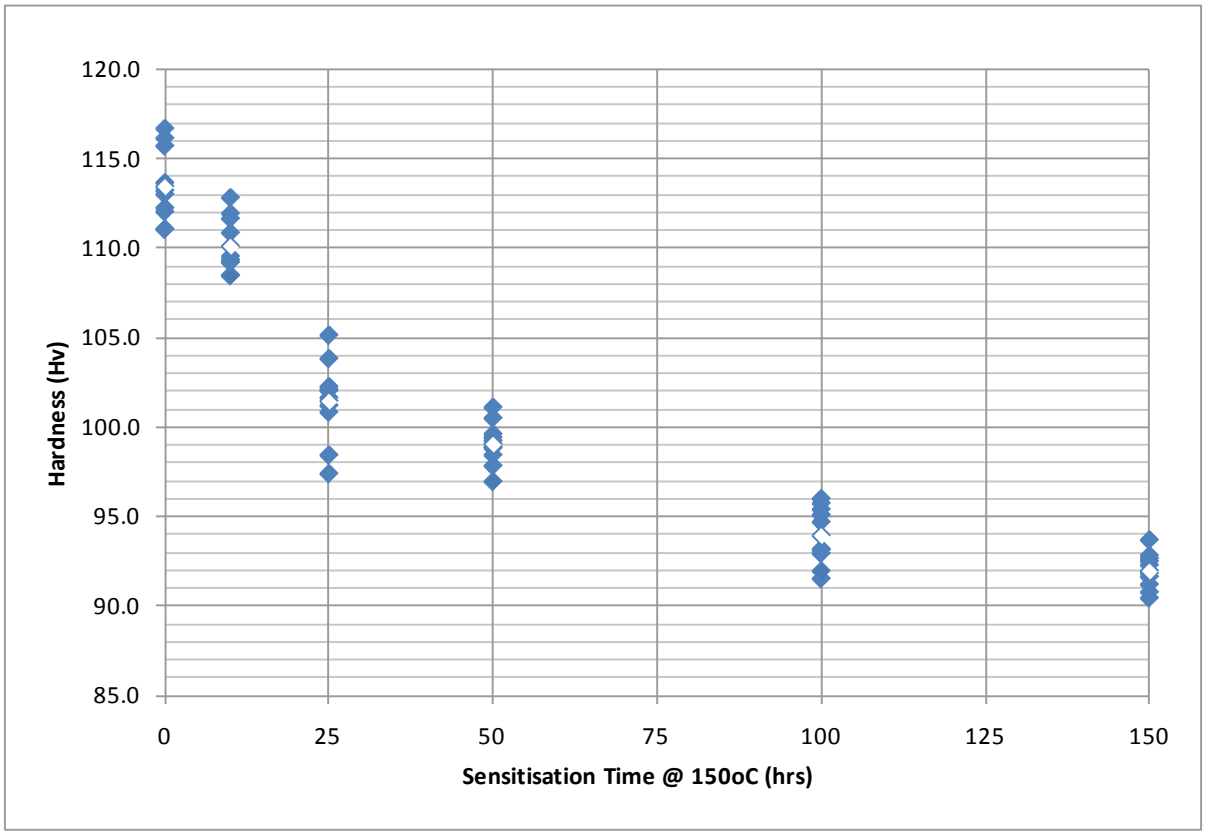

Fig. 4.2 Hardness (Hv) as a function of Sensitisation Time at 150°C

The reduction in hardness with increasing sensitization time can be attributed partly to reduction in the density of dislocations during recrystallisation of the cold-worked as-received specimens. It is generally known that the degree of recrystallisation in metallic alloys depends on annealing temperature and time. The density of dislocations could therefore decrease as new grains are formed during the sensitization heat treatment.

The reduction in hardness with increasing sensitization temperature and time can also be attributed to the precipitation of the Mg-rich phase and segregation of Mg atoms at grain boundaries, which draws solute Mg atoms away from the α-matrix. Consequently, as the concentration of solute Mg atoms decreases during sensitization the remaining Mg atoms still in solid solution become ineffective

obstacles to the movement of dislocations. A number of studies have reported that a decrease in solute atoms in solid solution could lead to a decrease in mechanical properties in 5xxx series alloys [18,22,51,68].

4.2 Corrosion Properties of AA5456-H116

4.2.1 Microstructural Characterisation

In this section, post-sensitisation AA5456-H116 will be identified microstructurally to document the effects of sensitisation time at 150°C on the corrosion susceptibility. A number of experimental techniques (see, Section 3) were used in order to fully understand the effects of sensitisation on the microstructure of AA5456-H116, all of which document the resistance to inter-granular corrosion.

4.2.1.1 Phosphoric Acid Etching

Phosphoric acid etching is a quick and simple screening test to detect the susceptibility to intergranular corrosion (IGC). It reveals the presence of β-phase through grain boundary etching in 10 % H_3PO_4.

The degree of sensitisation of all five heat-treatment conditions is shown following phosphoric acid etching in Figure 4.3 (A-E). No significant grain boundary attack can be seen in the as-received condition. The sample heated for 10 hours at 150°C (Figure 4.3B) shows slightly more localised attack compared to the as-received sample (Figure 4.3A). Obvious grain boundary attack can be seen for the remaining three sensitised conditions. More severe grain boundary attack is evident for the 100 hours sensitisation (fig 4.3 E) when compared to samples sensitised for 25 hours and 50 hours (Figure 4.3 C and D). It should be noted that the attack in the all sensitised samples is consistent with the respective grain structures of each sample (see figure 4.1).

These microstructures in figure 4.3 represent varying degrees of susceptibility ranging from highly susceptible to highly resistant, depending on sensitisation time at 150°C. Treatments that provide high resistance to Inter-granular Corrosion and therefore Stress Corrosion Cracking (SCC) are those that produce either no precipitate along grain boundaries or uniformly distributed precipitate within grains. In the latter case, corrosion along grain boundaries is minimised because the presence of precipitate or depleted regions throughout the microstructure increases the ratio of the total area of anodic regions to that of cathodic ones, thereby reducing the corrosion current of each anodic region. For alloys requiring microstructural control to avoid susceptibility, resistance is obtained by using heat treatments that produce precipitation throughout the microstructure (such as 262 hours at 150°C for AA5083 – 4.4wt.% Mg[21]).

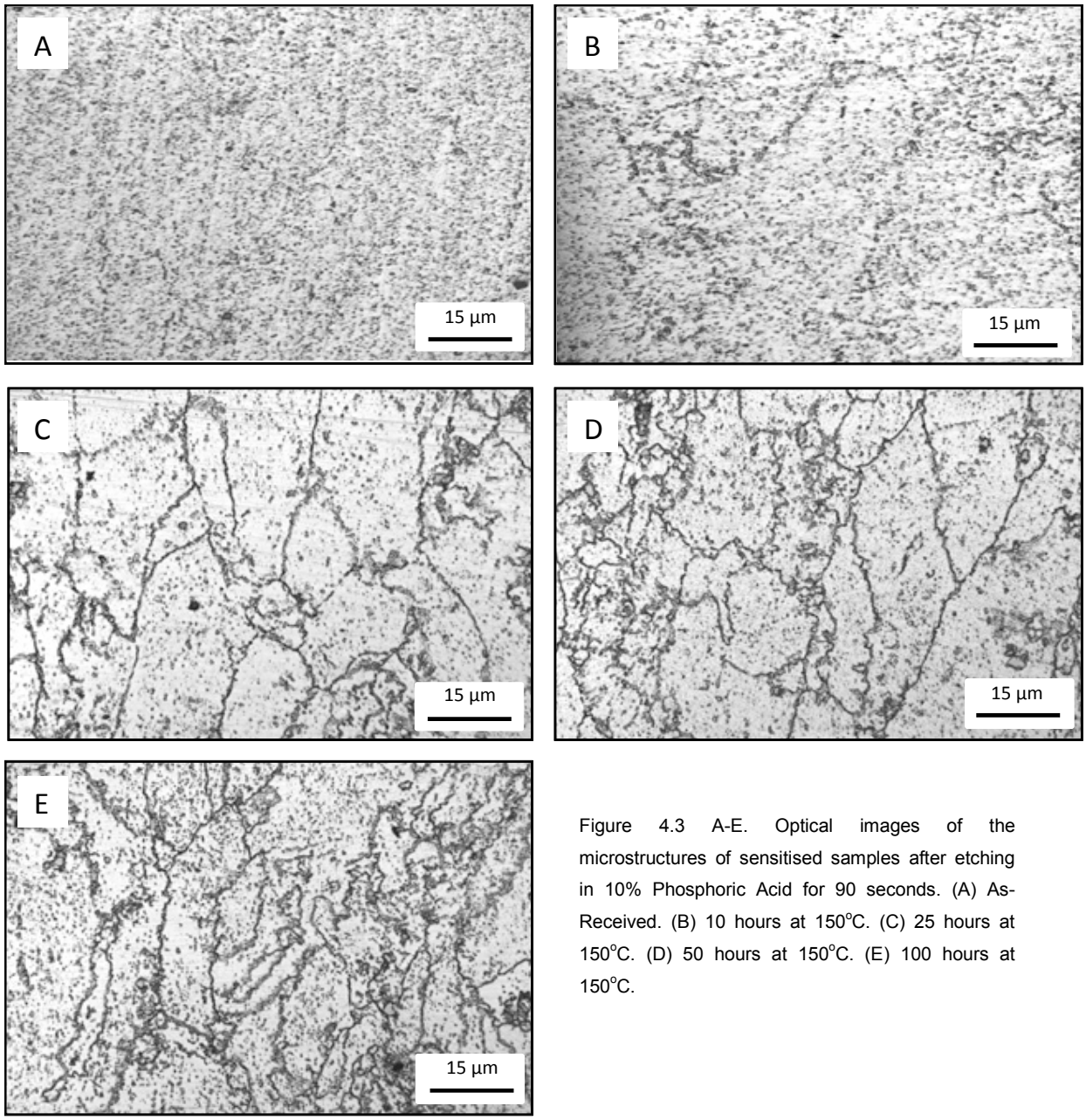

Figure 4.3 A-E. Optical images of the microstructures of sensitised samples after etching in 10% Phosphoric Acid for 90 seconds. (A) As-Received. (B) 10 hours at 150°C. (C) 25 hours at 150°C. (D) 50 hours at 150°C. (E) 100 hours at 150°C.

4.2.1.2 Nitric Acid Mass Loss Testing (NAMLT)

Nitric acid mass loss testing (NAMLT) is a standard method (ASTM G67-04 [69]) for quantitative testing of intergranular corrosion (IGC) susceptibility of 5xxx series (Al-Mg) alloys. Nitirc acid preferentially dissolves β-phase , in preference to the solid solution of magnesium in the aluminum matrix. When this compound is precipitated in a relatively continuous network along grain boundaries, the effect of the preferential attack is to corrode around the grains, causing them to fall away from the specimens. Such

dropping out of the grains causes relatively large mass losses of the order of 25 to 75 mg/cm^2, whereas, samples of intergranular-resistant materials lose only about 1 to 15 mg/cm^2. Therefore, according to ASTM G67-04, if the mass loss is greater than 25 mg cm^{-2}, the sample is considered susceptible to intergranular corrosion, whereas if the mass loss is below 15 mg cm^{-2}, the sample will be resistant to intergranular corrosion. The NAMLT values for AA5456-H116 as a function of aging time at 150^{o}C are presented in table 4.1.

Table 4.1 NAMLT results for all heat treatments of AA5456-H116 (Standard Deviation is taken from 2 measurements)

Material Identification	**Heat Treatment**	**NAMLT Value (mg/cm^2)**	**Standard Deviation (mg/cm^2)**
AA5456 H116	As-Received	**3.1**	**0.1**
	10 hrs – 100^{o}C	**4.7**	**0.1**
	10 hrs - 150^{o}C	**10.78**	**0.3**
	25 hrs - 150^{o}C	**28.76**	**2.1**
	50 hrs - 150^{o}C	**49.57**	**1.1**
	100 hrs - 150^{o}C	**58.36**	**1.4**

AA5456-H116 is resistant to Inter-granular Corrosion (IGC) both as-received and after 10 hours of heat treatment at 100^{o}C as indicated by very low weight loss values of less than 3 and 5mg.cm^{-2}, respectively. It is clear that the longer aging times, at 150˚C, lead to sensitisation. Samples heated for 10 hours sensitisation at this temperature yielded a NAMLT of 10mg.cm^{-2} suggesting IGC resistance; however when held for prolonged periods at the same temperature sensitisation of the microstructure occurred as indicated by the high weight loss values of 50 and 58mg.cm^{-2} at 50 and 100 hours respectively. Aging the material at 150^{o}C for 25 hours gives a NAMLT value of 28.76mg.cm^{-2}. According to ASTM G67-04 [70] this suggests the sample may exhibit IGC resistance or susceptibility and that further investigation is needed.

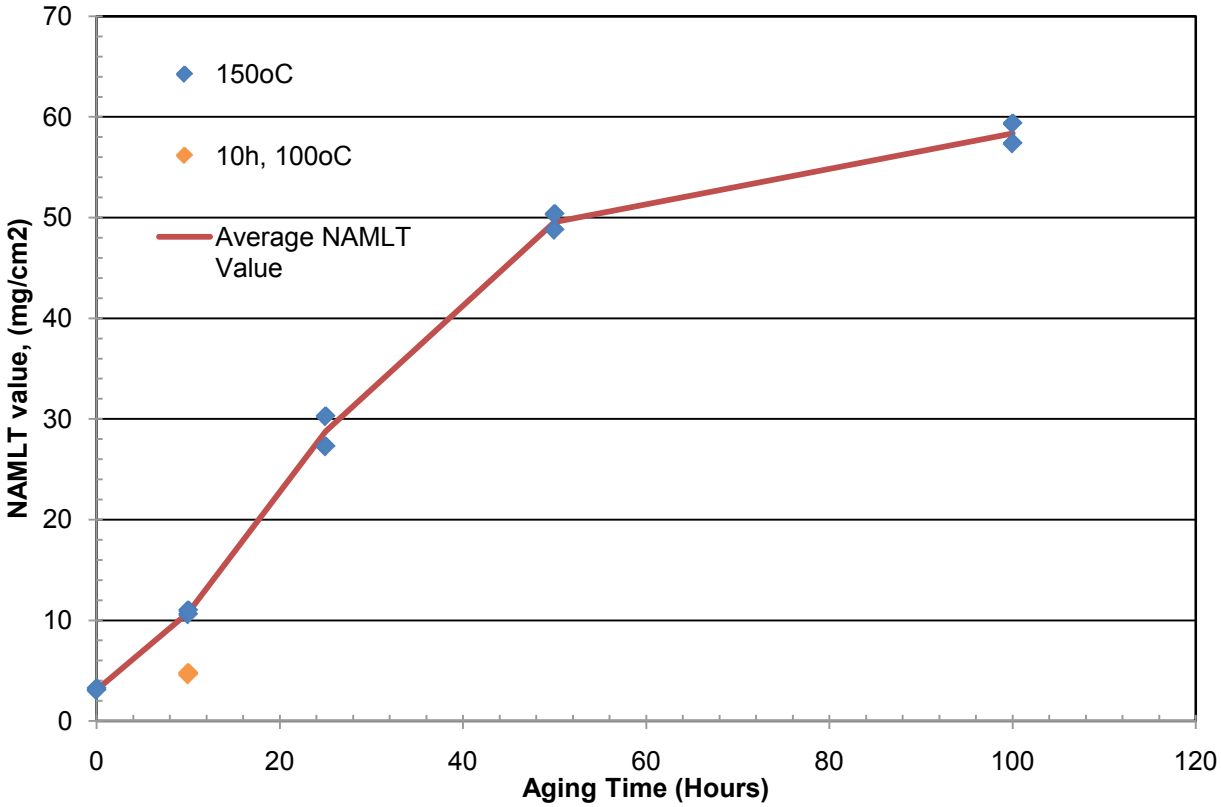

Fig. 4.4 Graph showing NAMLT values as a function of sensitisation time at 150°C.

It is clear that the degree of susceptibility of AA5456 H116 at 100°C is less that that at 150°C. As shown by the increase from 4.7 to 10.78 mg.cm^{-2} at 10hrs. Previous literature has documented a similar increase. Yuan[41] documented the NAMLT values of heat treatments on a similar Al-Mg alloy AA5182. Samples that were aged for 10hrs at between 70°C and 100°C showed low mass losses (less than 6.6mg.cm^{-2} [see appendix A.2]). NAMLT values for AA5182 samples heat treated for 10hrs at 150°C yielded an increased mass loss of 39.8 mg.cm^{-2}. Yuan[41] concluded that the reason for the increase at temperatures around 150°C can be attributed to faster diffusion of Mg and rapid kinetics of the β-phases precipitation at the higher temperature.

Selected samples of AA5456-H116 (10, 25 and 100 hrs at 150°C) were cross sectioned along the transverse direction then etched in Keller's solution to examine metallographically the morphology of corrosion. Prior to cross sectioning, macro images of the samples were taken to show the presence of a midline that was produced after NAMLT. This can be attributed to the differing magnesium contents throughout the sample (see Appendix A.3) [68]. Optical micrographs of the cross-sectional areas revealed substantial IGC that appears to increases with increasing sensitisation time. The sample aged for 10 hours at 150°C showed a small amount of IGC that has not penetrated the surface more than

approximately 50μm (figure 4.5B). In contrast an aging time of 100hrs at the same temperature revealed a large amount of IGC that extends along grain boundaries to approximately 150μm. At 25 hrs at 150^{o}C (Fig. 4.5 C) the IGC is not as severe as that of Fig 4.5 D. However, when compared to that Fig. 4.5B it is clear the IGC is greater and also that the attack is deeper (approximately 125μm).

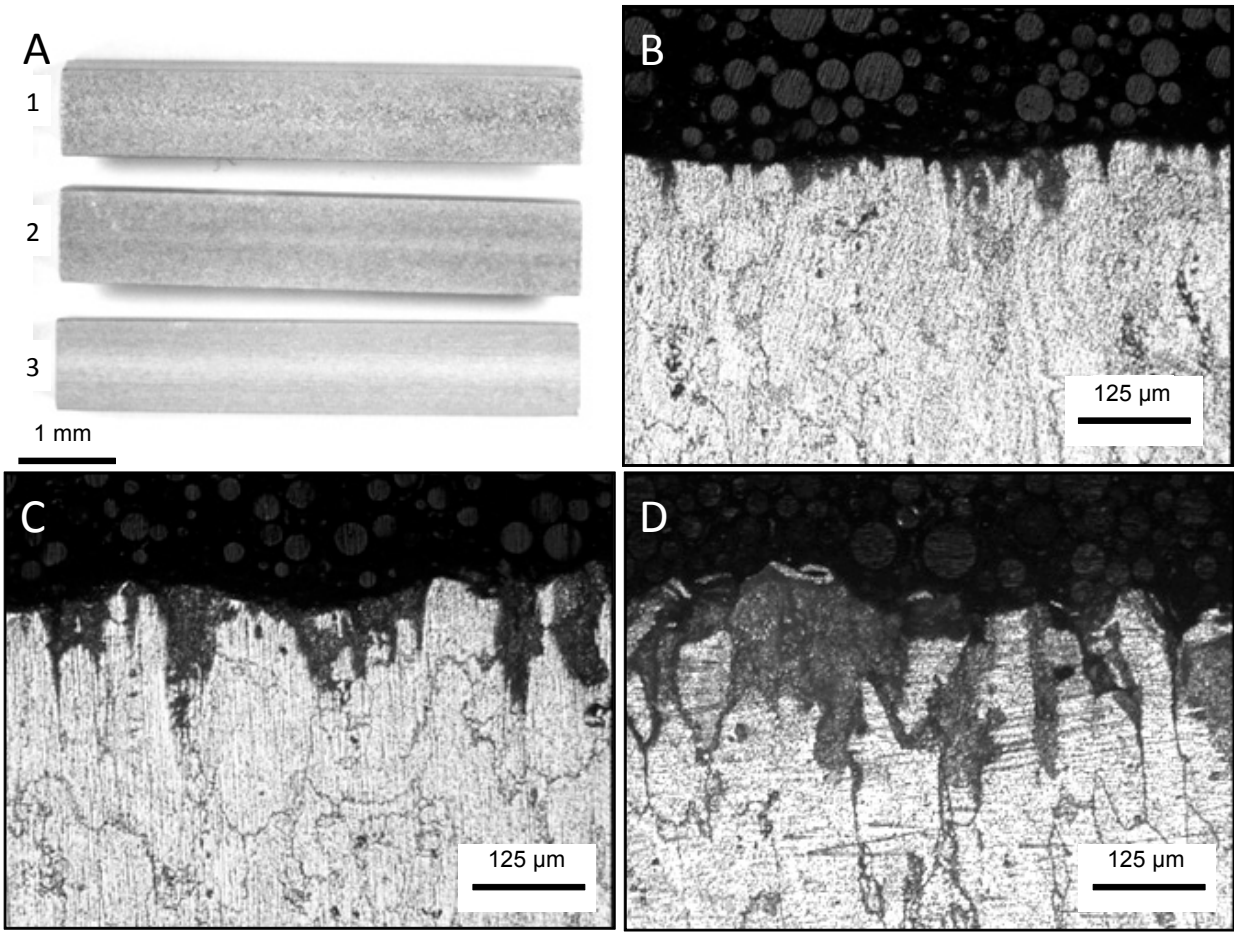

Fig 4.5 Various heat treated AA5456 H116 NAMLT samples (A) macrographic image showing the extent of the corrosion and clear midline on 100-150 (A1), 25-150 (A2), and 10-150(A3) (B) Cross section of 10-150 sample showing the extent of Inter granular corrosion (C) Cross section of 25-150 sample showing the extent of Inter-granular corrosion (D) Cross section of 100-150 sample showing the extent of Inter granular corrosion.

4.2.4 Electrochemical Behaviour

The pitting and intergranular corrosion susceptibility of the different heat treated conditions of AA5456-H116 was evaluated electrochemically using anodic potentiodynamic polarisation in acidified chloride solutions, through the use of micro-electrochemical cells.

4.2.4.1 Potentiodynamic Measurements

The breakdown potential is defined as the potential at which the alloy becomes anodically active, corresponding to the propagation of localised corrosion. Samples aged at 150°C show a decrease in breakdown potential with increasing ageing time, from as-received to 100 hours (see fig 4.6). The breakdown potential clearly shifts to more negative values (from -0.66 to -0.74 V), thus the anodic activity increases with increasing aging time at 150°C (sensitisation time). This can, in part, be used to explain the marked increase in susceptibility to corrosion as documented by the NAMLT results

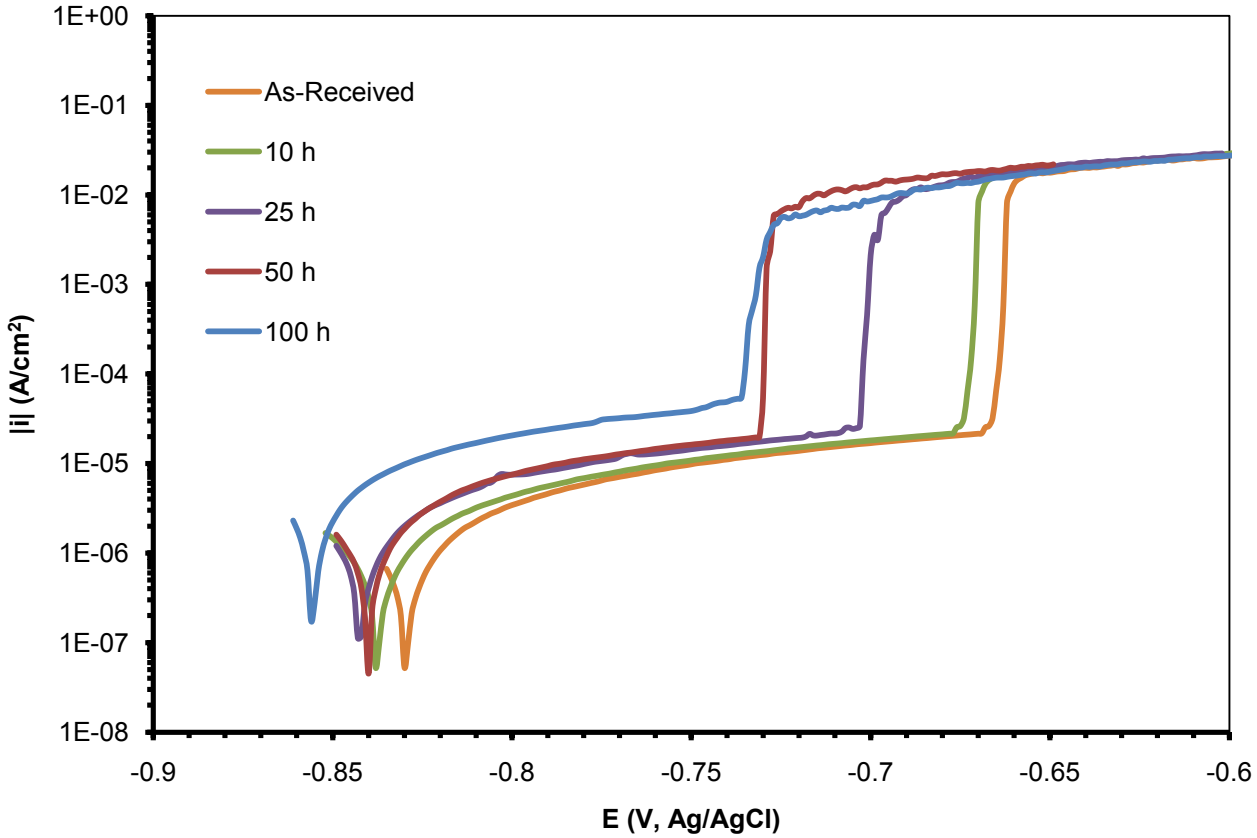

Figure 4.6 Anodic potentiodynamic curves, gained using a 'droplet' electrochemical cell, documenting the effect of ageing time at 150°C on polarisation of AA5456-H116 in 3.5% NaCl solution acidified to pH3 with HCl. Sweep rate 1 mV/sec.

4.2.5 Immersion testing in Acidified 3.5% NaCl Solution

It is evident that the development of inter-granular corrosion can be a slow process. In order to examine this, as-received and heat treated (see table 3.2) samples of 5456-H116 were immersed in a 3.5% NaCl, acidified to pH3 with HCl, for a period of 336 hours. Samples of the same heat treatment were also subjected to an alternate immersion for the same 336 hour period in order to compare the effects of the two different types of immersion.

4.2.5.1 Pitting Documentation of Full Immersion Specimens

The pit depth and density chart (figure 4.7) and table document the average distribution and depth of pits observed via optical microscopy after full immersion in pH3 3.5% NaCl (see section 3.6). The pits under 5μm in depth appeared abundant in all heat treated conditions. The density and depth of pits increase with increasing aging time at 150^{o}C. It can also be seen that there are greater number of deep pits in the 50hr and 100hr aging times. It is apparent from the chart that there is trend in that the as-received and 10hrs at 150^{o}C conditions have very similar densities and pit depth. The 25 hour sample appears to have a slight increase on the previous two conditions, both in depth and density. Finally, from the chart it is clear that the 50 and 100 hour show the greatest density and depth of pits. The densities exceed 25 pits/mm^2 and 30 pits/mm^2 respectively, both with maximum pit depths in excess of 25μm (see table 4.2).

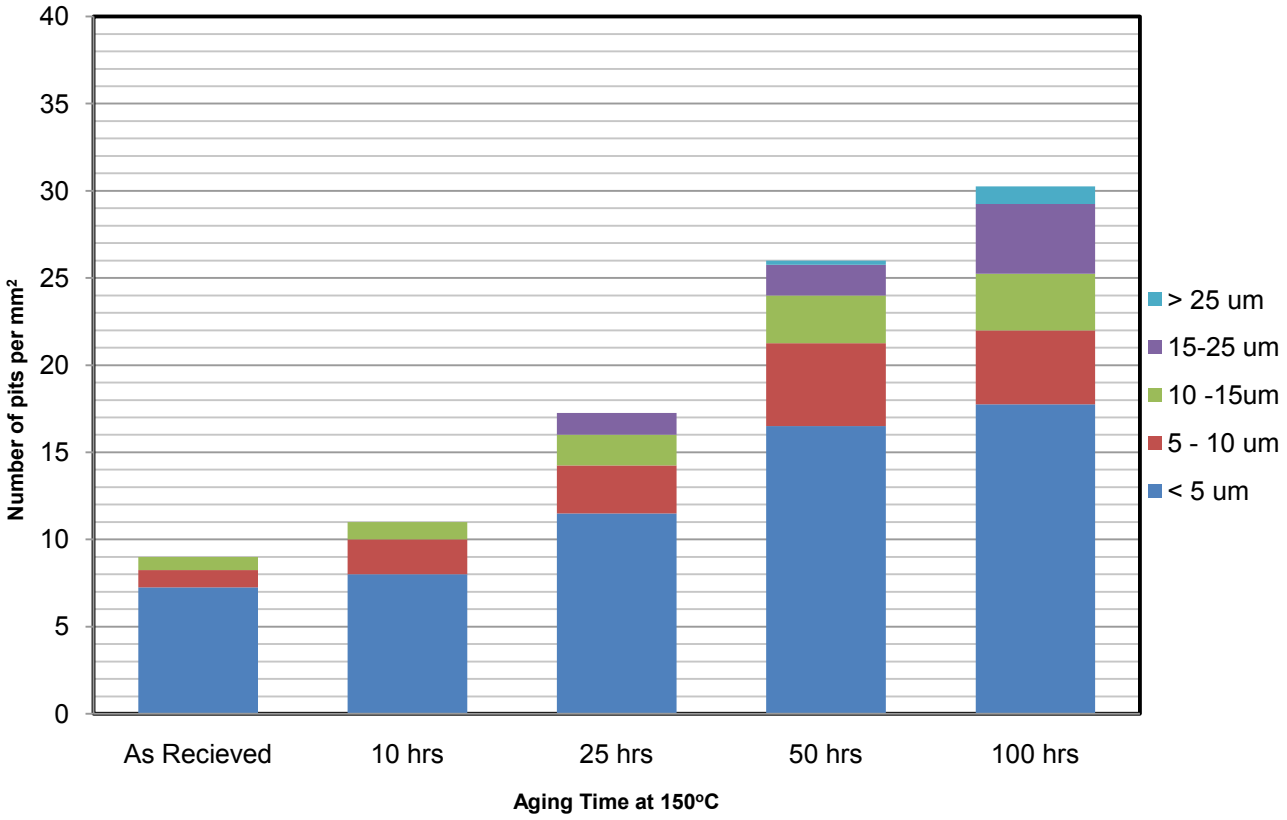

Figure 4.7 A graph representing the pit depth and densities of 336 hours full immersion specimens as a function of sensitisation time.

Table 4.2 shows the pit demographic present on the surface of various heat-treated and as-received specimens. A total area of 4mm^2 was measured and documented via optical microscopy in order to gain a fair and representative result. It can be seen quite clearly that there is a relationship between sensitisation time and pit depth and density. As previously concluded it appears that the longer sensitisation times result in greater, more aggressive localised corrosion attack. This is clear from the marked increase in pit density and maximum pit depth observed. As-received samples have a relatively low pit density and max pit depth, in comparison the larger sensitisation times of 50 hours and 100hours at 150^{o}C result in far greater pit depths and densities. The sample sensitised for 25 hours seems to be directly in the middle, whereby there is a large increase when compared to the as-received and 10 hours specimens, yet when comparing the results to the greater sensitisation times of 50 and 100 hours the max pit depth and density are not as great. This is backed up by the NAMLT results that 25 hours at 150^{o}C needs more investigation to determine whether the material is susceptible. However it can be noted that there is a greater extent of pitting and greater pit depth than the as-received and 10

hours specimens (9μm and 9pits/mm^2, 12μm and 11pits/mm^2 respectively), both of which would contribute high stress localisation for premature failure.

Table 4.2 Table presenting results obtained via optical microscopy over a 4mm^2 area on full immersion specimens of varying sensitisation times.

Full Immersion in 3.5% NaCl pH3 Solution					
Heat Treatment	**Thickness, mm**	**Exposure Period**	**Maximum Pit Depth, μm**	**Average Pit Depth , μm**	**Pit Density, pits/mm^2**
As Received	6.34	14 Days	9	3.2	9
10 hrs @ 150^{o}C	6.27	14 Days	12	3.3	11
25 hrs @ 150^{o}C	6.33	14 Days	16	6.1	17.25
50 hrs @ 150^{o}C	6.35	14 Days	25.5	7.3	26
100 hrs @ 150^{o}C	6.28	14 Days	28	7.8	30.5

4.2.5.2 Pitting Corrosion Morphology of Alternate Immersion Specimens

The pit depth and density, chart and table demonstrate the distribution and depth of pits (figure 4.8 and table 4.3) for alternately immersed specimens in various heat treatment conditions (see section 3.6). Again similarly to that of the full immersion sample the pits under 5μm in depth appeared abundant in all heat treated conditions. Correspondingly, the density and depth of pits increase with increasing aging time at 150^{o}C. It can also be seen that there are greater number of deep pits in the 50hr and 100hr aging times. It is clear from figure 4.8 that there is a relationship between the pit depth and density and sensitisation time. This is shown by the as-received and 10hrs at 150^{o}C conditions having very similar densities and pit depth. The 25 hour sample appears to have a slight increase on the previous two conditions, both in depth and density. Finally the 50 and 100 hour conditions show the greatest density and depth of pits. The greater the sensitisation time the greater the number of pits and

depth of pits. The longest sensitisation times of 50 and 100 hours produce densities that are 31 pits/mm^2 and 34.5µm respectively, both have maximum pit depths in excess of 25µm (see table 4.3).

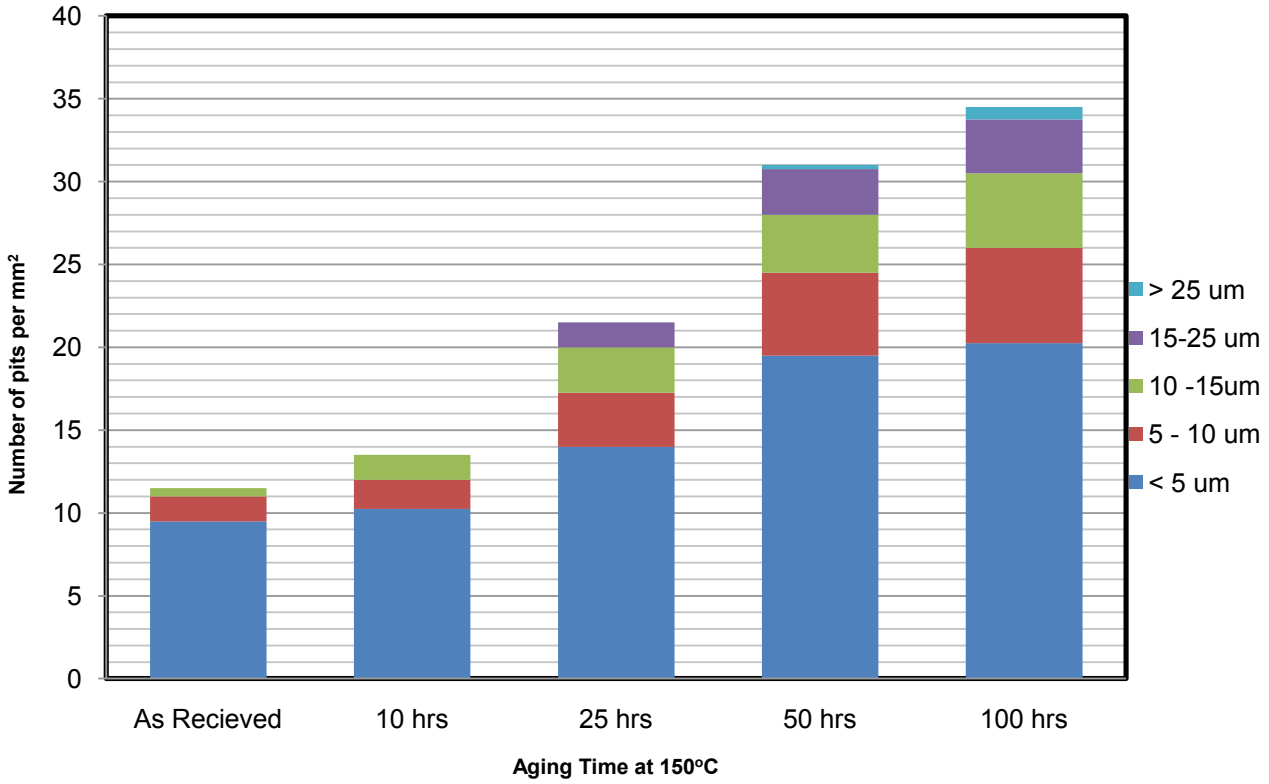

Figure 4.8 A graph representing the pit depth and densities of 336 hours full immersion specimens as a function of sensitisation time.

Table 4.3 shows the results from the figure 4.8. Again a total area of 4mm^2 was measured and documented via optical microscopy in order to gain a fair and representative result. It is quite clear that the results follow a similar pattern to those of the full immersion specimens whereby there is an increase in the severity of pitting (max pit depth, pit density) with increasing sensitisation time. However, there is also an increase in the severity of attack when compared to the results gathered from the full immersion specimens. As shown in figures 4.7 and 4.8 all heat treatments and as-received samples show a greater maximum pit depth, average pit depth and pit density after alternate immersion in the same heat treatment conditions compared to those subjected to full immersion.

Table 4.3 Table presenting results obtained via optical microscopy over a 4mm^2 area on alternate immersion specimens of varying sensitisation times.

Alternate Immersion in 3.5% NaCl pH3 Solution					
Heat Treatment	**Thickness, µm**	**Exposure Period**	**Maximum Pit Depth, µm**	**Average Pit Depth , µm**	**Pit Density, pits/mm^2**
As Received	6.29	14 Days	12	3.9	11.5
10 hrs @ 150^{o}C	6.32	14 Days	14.5	4.4	13
25 hrs @ 150^{o}C	6.34	14 Days	19	7	21.5
50 hrs @ 150^{o}C	6.29	14 Days	27.5	8.1	31
100 hrs @ 150^{o}C	6.3	14 Days	32.5	8.3	34.5

4.2.5.3 Comparison between Full Immersion and Alternate immersion

When comparing alternate immersion specimens to full immersion specimens of the same aging condition the pit depth and density increase. This is as expected because of the differing corrosion environment which samples undergoing alternate immersion experience. During the alternate immersion cycle the sample is allowed to dry after one immersion before being immersed again. During this drying period small droplets of the acidified chloride solution that are left on the surface dry producing a highly concentrated acidic salt deposit which, attacks the specimen more aggressively than the original test solution. In addition, during alternate immersion testing a thin film of the solution, frequently renewed and almost saturated with oxygen, is maintained throughout most of the exposure period. This produces a more aggressive solution for localised corrosion, resulting in increased pit attack and possibly enhanced inter-granular corrosion. Contrastingly the full immersion sample is completely submerged in solution reduced access to oxygen.

4.2.6 Discussion

4.2.6.1 Observations of Precipitation at Grain Boundaries

It is evident from the results that the precipitation of β phase at grain boundaries is strongly dependant on ageing (i.e. sensitisation) temperature and time. However, the dependence of segregation of Magnesium on the ageing temperature and time is more complex, which is related to segregation mode and the precipitation at grain boundaries.

It can be seen from the Al-Mg equilibrium phase diagram that the solubility of magnesium in aluminium decreases rapidly until less that 1 wt.% is soluble at room temperature. Alloys containing more magnesium in solid solution than equilibrium permits tend to precipitate the excess Mg in the form of β phase (Al_3Mg_2). As would be expected, precipitates nucleate preferentially at grain boundaries since these sites correspond to higher energy sites with larger free volume than the surrounding matrix and can therefore serve as more efficient nucleation sites. However at room temperature the precipitation process is very slow.

Precipitation is a time- and temperature-dependant process which, tends to occur more rapidly at higher temperature and longer ageing times. Searles et al. [21] used transmission electron microscopy to evaluate β precipitation of AA5083 after various aging times at 150°C. TEM evaluation after a 9-hour treatment produced small, isolated β precipitates. They concluded that the microstructure was resistant to IGC. At longer sensitisation times, β precipitation increased, leading to IGC susceptibility. The samples sensitized for 82.5 hours showed slight grain-boundary precipitation in the form of discreet particles. After 189 hours at 150°C, a continuous film of β precipitates was formed at grain boundaries. Aging times in excess of 189 hours showed discontinuous β precipitation suggesting that the continuous film breaks up at sufficiently long sensitisation times. This distribution of β-phase precipitates after 189hrs at 150°C demonstrates the phenomenon of stabilisation, whereby, β-phase doesn't preferentially decorate the grain boundaries and begins to precipitate throughout the grains as coarse precipitates; therefore resistance to IGC is created. Various other studies have documented the effect of sensitisation time and temperature on β precipitation using TEM and have shown similar results[6, 16].

In this investigation, based on the results of NAMLT and Phosphoric acid (H_3PO_4) etching, it can be concluded that precipitation of β-phase at grain boundaries was enhanced with elevated temperature

and increasing ageing time. The most extensive β-phase precipitation, at the majority of grain boundaries, occurred after ageing at 150°C for 100 hours. Incidentally this was the most sensitised condition investigated in this work.

4.2.6.2 Inter-granular Corrosion Behaviour

It is widely accepted that the intergranular corrosion (IGC) behaviour of Al-Mg alloys is associated with the presence of β phase precipitates at grain boundaries [5-7, 22, 31, 52]. Such a phase is more reactive than the aluminium matrix, and therefore corrodes preferentially. ASTM G67-04 [69] method has been used in the industry to accurately assess the susceptibility of Al-Mg alloys to IGC. If the mass loss is greater than 25 mg cm^{-2}, the sample will become susceptible to IGC, whereas if the mass loss is below 15 mg cm^{-2}, the sample will be resistant to IGC. In the present work there is no clear grain boundary attack in 10% phosphoric acid (H_3PO_4) for samples with mass loss below 25 mg/cm2 (Fig 4.5A and B) while samples with the NAMLT value over 25mg/cm^2, the amount of grain boundary attack rises rapidly with increasing NAMLT values, after reaching values in excess of 40mg/cm^2, grain boundary corrosion is severe and appears to aggressively attack all grain boundaries. The NAMLT results correlate well with the microstructural observation in 10% H_3PO_4. However, it is evident that there is considerable β precipitation for the sample sensitised for 25hrs at 150°C (28mg/cm^2) it could also be mentioned that it is not as extensive as that of the higher NAMLT values. A comparable increasing grain boundary attack trend with increasing NAMLT values was reported by Oguocha et al.[22] and Popovic and Romhanji[31] for similar alloys (AA5083 and Al-6.8wt.%Mg). Oguocha et al. conducted extensive studies on the sensitisation of AA5083 H116 at 80°C, 100°C, 150°C, 175°C and 200°C for exposure times from as-received up to 4 weeks (672 hours), found that although samples aged for 24 h were susceptible, those sensitised for in excess of 24 hours showed an increase in β precipitation and susceptibility. These results correlate well with the AA5456 H116 NAMLT results in this study.

Combining the NAMLT results and the phosphoric acid etching images, it can be seen that when NAMLT value is over 25 mg/cm^2, the sample is susceptible to IGC whereas with a NAMLT value below 15mg/cm^2 samples are resistant to IGC. The results obtained from this present work are in agreement with the criteria set out in ASTM67-04 [69]. Thus it can be concluded that NAMLT is an accurate method of predicting the IGC susceptibility of AA5456-H116.

Samples that gave NAMLT values in the range of 1-10 mg/cm^2 (as-received and 10 hours at 150°C) showed very similar anodic behaviour in naturally aerated 0.1M NaCl, giving breakdown potentials

between -0.66 and -0.68 V(Ag/AgCl). However, the breakdown potential shifts to a more negative value with increasing NAMLT (50-60mg/cm^2) value to around -0.74 to -0.73 V(Ag/AgCl). The sample with the NAMLT value close to the 25mg/cm^2 susceptibility value (as indicated by ASTM 67-04 [69]) gave a breakdown potential of -0.7, in between the samples that are considered highly susceptible and highly resistant. Intergranular corrosion associated with this increased anodic activity was quite clearly present on the samples with the more active breakdown potential. The corrosion behaviour is consistent with electrochemical behaviour in chloride-containing solutions, where a more negative breakdown potential for β-phase has been reported [5,21,67].

4.2.6.3 Pitting Documentation of Immersion Specimens

It can be seen quite obviously that there is a relationship between sensitisation time, pitting depth and density and immersion type. The increase in sensitisation time at 150°C results in an increase in the severity of pitting. The aggressive nature of the alternate immersion environment also causes greater pit depth and density. At the higher sensitisation times of 50 to 100 hours not only is the pitting denser, but both the average pit depth and maximum pit depth observed also increase. Below 25 hours it can be concluded that pitting is not as severe, with lower depths and densities. However, there is a large increase from 25hrs to 50hrs indicating a critical aging time. All of the above results indicate towards the presence of the critical aging time at 150°C, whereby β precipitates begin to preferentially nucleate at grain boundaries. This critical or minimal aging time has been well documented by Oguocha et al.[22] [2008], and Searles & Buchheit[21] for the same alloy (AA5083) albeit via different experimental techniques. Searles & Bucheit documented using TEM evaluation that samples sensitized for 82.5 hours showed slight grain-boundary precipitation in the form of discreet particles separated by micrometer distances. The lower wt.% of Mg (4.4wt.% Mg) in AA5083 may account for the higher critical aging time of 82.5 hours. Oguocha et al. found via NAMLT that the minimum aging time (for susceptibility) for the AA5083 (4.9wt.% Mg) was around 25 hours concurring with the results found for AA5456 used in this study. The similar Magnesium contents of both the alloys used in the respective studies may account for the similar result.

4.3 Corrosion Fatigue Properties of AA5456

The fatigue and corrosion fatigue behaviour of AA5456-H116 and the subsequent heat treatments (see Table 3.2) were studied in order to determine the possible effect of sensitisation of AA5456-H116 to fatigue and in particular corrosion fatigue.

4.3.1 S-N Curve (Wöhler Diagrams)

Figure 4.9 compares the fatigue lifetime (S-N) results of sensitised AA5456-H116 specimens fully immersed in acidified (pH3) 3.5% NaCl for 336 hours. The results show that the longer the sensitisation the lower the fatigue life. At the lower stress of 230MPa the greatest data spread is seen, which indicates a relationship between sensitisation and fatigue lifetime. As-received samples and samples aged for 10 hours at 150^{o}C exhibit no failure (ran out at 10^7 cycles) with the exception of a single as-received result which failed at approximately 6,000,000 cycles. This was due to crack initiation at the edge of the specimen. As the sensitisation time increase the specimens begin to fail after fewer cycles. Two samples sensitised for 25 hours at 150^{o}C failed at 3,000,000 and 5,000,000 cycles. However, a single specimen of the same heat treatment ran out at the same stress. Samples sensitised for 100 hours and 50 hours at 150^{o}C failed at significantly lower number of cycles (two failed within the 10^5 cycle range).

Figure 4.10 compares S-N data from the same AA5456-H116 alloy alternately immersed in the same acidified (ph3) 3.5% NaCl for 336 hours (see section 3.2.3). A very similar relationship to that of the fully immersed specimens is documented; with the only major difference being that the more aggressive nature of the alternate immersion has shortened the fatigues lifetime of sample subjected to the same stress. For example, at an applied stress of 230MPa, a sample aged for 100 hours at 150^{0}C failed after approximately 250,000 cycles. This is comparatively less than the samples of the same heat treatment subjected to full immersion. However, the same trends are still apparent, whereby the longer the sensitisation time at 150^{o}C the shorter number of cycles to failure. A single sample aged for 10 hours at 150^{o}C that was alternately immersed failed at approximately 7,500,000 cycles, while all of the samples that were tested in the as-received ran out (i.e unbroken at 10^7 cycles). At the higher stress of 260MPa there is a reduced spread, nevertheless there is still a clear relationship between sensitisation time and number of cycles till failure.

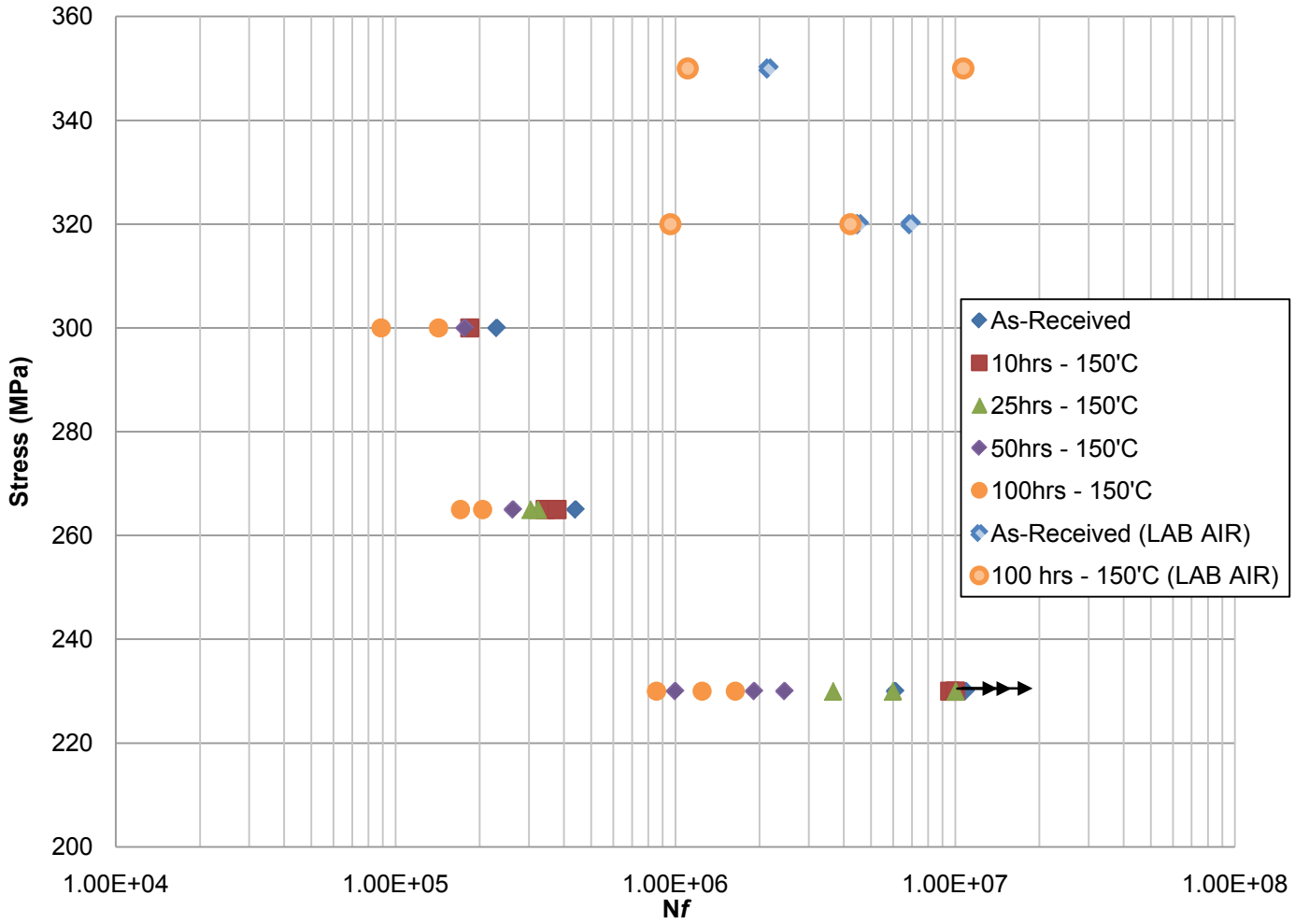

Fig. 4.9 Fatigue lifetime curves (S-N curves) in acidified (pH3) 3.5% NaCl (full immersion) comparing the effects of sensitisation time at 150^0C (R = 0.1, ω = 15Hz) for AA5456-H116.

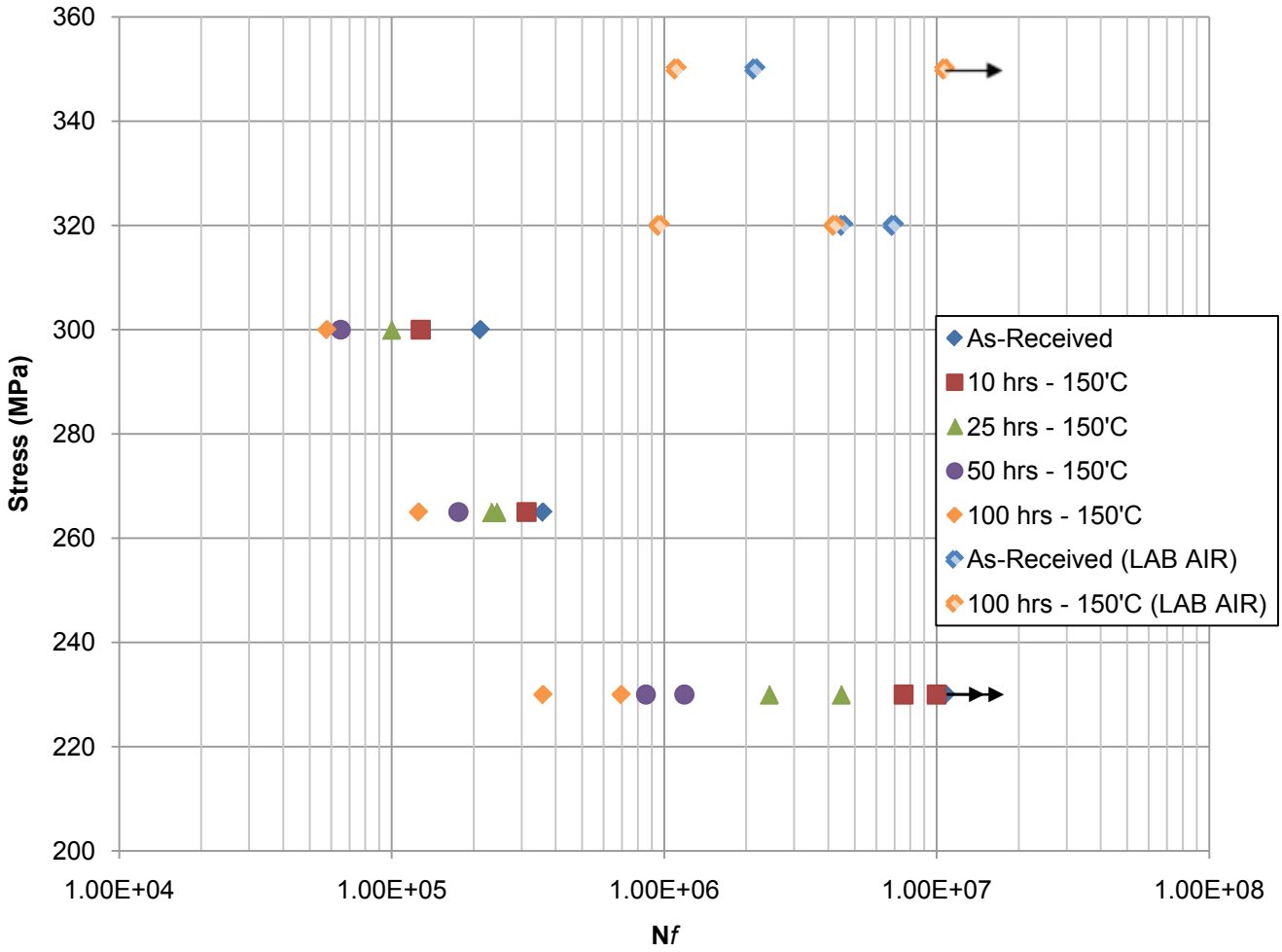

Fig. 4.10 Fatigue lifetime curves (S-N curves) in acidified (pH3) 3.5% NaCl (alternate immersion) comparing the effects of sensitisation time at 150^0C (R = 0.1, ω = 15Hz) for AA5456-H116.

Figures 4.11, 4.12 and 4.13 present data gathered from the pit morphology analysis compared with the fatigue results presented above. Firstly it is clear that the density, depth and fatigue lifetime are affected by the type of immersion. The alternate immersion specimens showing a greater average pit depth, average pit area ratio and shorter fatigue lifetime. In contrast the full immersion specimens show a comparative reduction in average pit depth, pit area ratio and relatively longer fatigue lifetimes. These results also document the relationship between the sensitisation time and the susceptibility of the alloy to both corrosion and fatigue, whereby the longer the sensitisation time the greater the average pit depth, area ratio and the shorter the fatigue lifetimes. For example, as-received samples and those aged for 10 hours at 150^{o}C have similar pit density of less than 15 pits/mm^2 the total specimen area, while their fatigue lifetimes are approximately 10^7 cycles. On the other hand Samples sensitised for 100 hours at 150^{0}C show a substantial increase in pit density for both alternate immersion and full immersion tests of between 30 and 35 pits/mm^2. While the fatigue lifetimes are less than 1,000,000 cycles. The same conclusions can be drawn from the comparison between pit depth and fatigue lifetime. Similarly when comparing NAMLT to fatigue lifetime there is an obvious relationship whereby the increased NAMLT number results in lower fatigue lifetimes. This is as expected because higher NAMLT numbers equates to a greater susceptibility to inter-granular corrosion, and therefore samples of higher sensitisation time are more susceptible to localised corrosion, resulting in a greater number of crack initiation sites, and therefore lowers corrosion fatigue lifetimes.

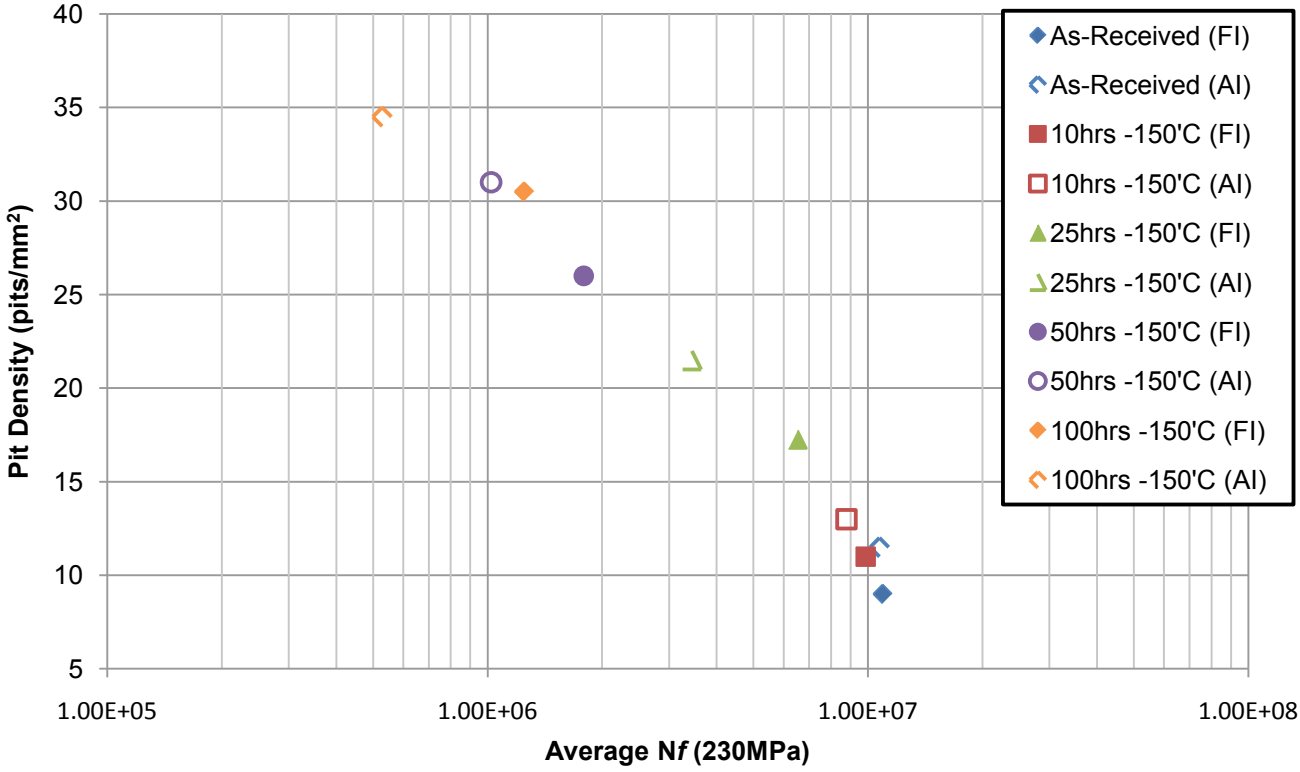

Fig. 4.11 Average fatigue lifetime at 230MPa (N*f*) vs pit density (ptis/mm^2) (S-N curves) in acidified (pH3) 3.5% NaCl (alternate immersion, AI, and full immersion, FI) comparing the effects of sensitisation time at 150^{o}C (R = 0.1, ω = 15Hz) for AA5456-H116.,

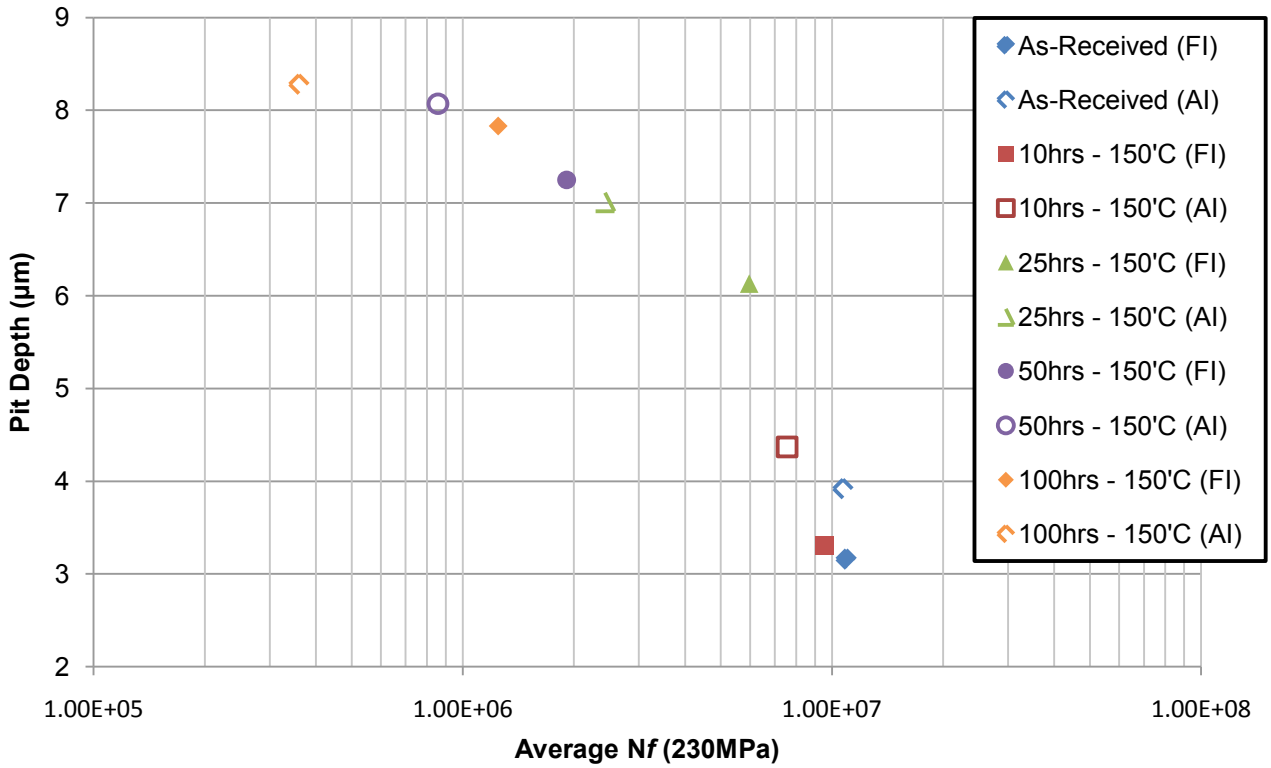

Fig. 4.12A Average fatigue lifetime at 230MPa (N*f*) vs average pit depth (µm) in acidified (pH3) 3.5% NaCl (full and alternate immersion) comparing the effects of sensitisation time at 150°C (R = 0.1, ω = 15Hz) for AA5456-H116.

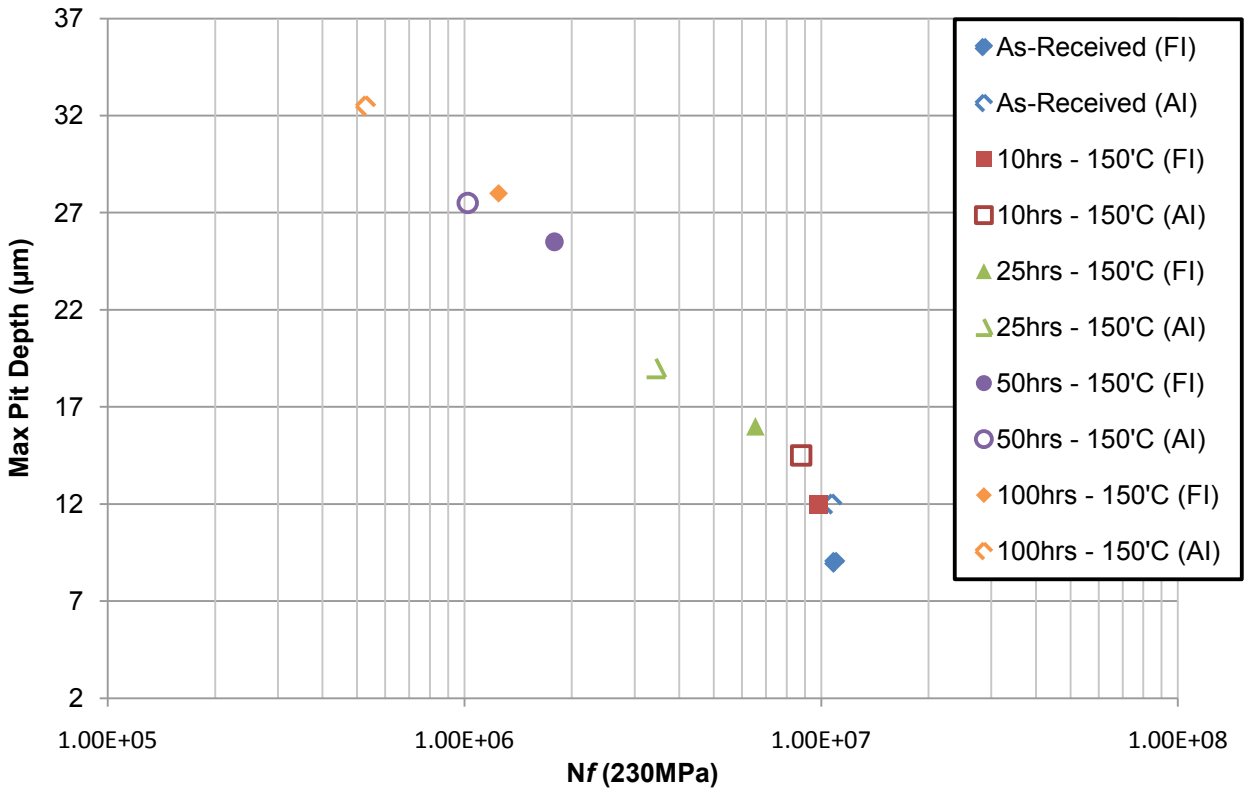

Fig. 4.12B Average fatigue lifetime at 230MPa (N*f*) vs maximum pit depth (µm) in acidified (pH3) 3.5% NaCl (full and alternate immersion) comparng the effects of sensitisation time at 150°C (R = 0.1, ω = 15Hz) for AA5456-H116.

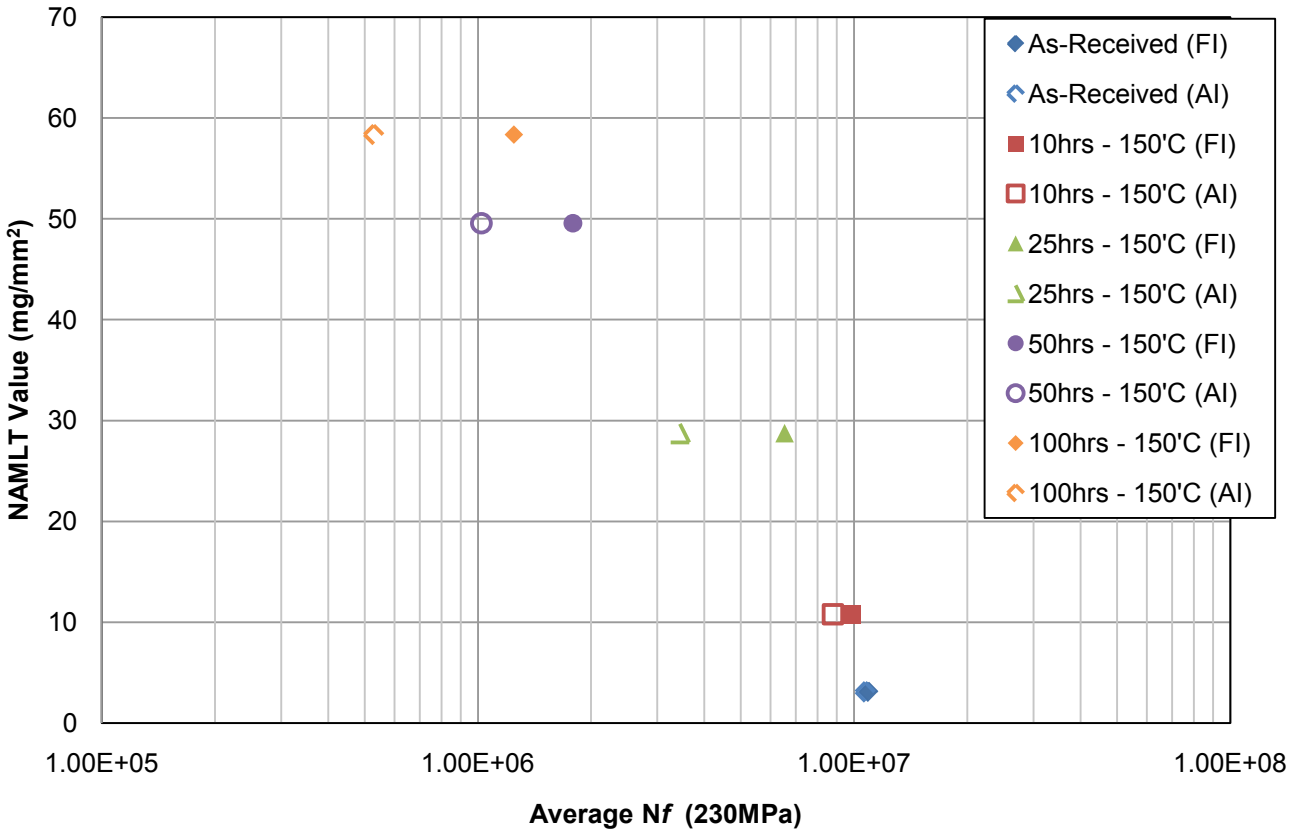

Fig. 4.13 Average fatigue lifetime (N*f*) at 230MPa vs NAMLT (mg/mm^2) (S-N curves) in acidified (pH3) 3.5% NaCl (alternate immersion, AI, and full immersion, FI) comparing the effects of sensitisation time at 150^{o}C (R = 0.1, ω = 15Hz) for AA5456-H116.,

4.3.2 Fractography

This section presents a comprehensive fractographic examination of the various sensitised specimens of AA5456-H116 that were fully and alternately immersed for 336 hours in acidified 3.5% NaCl and then subjected to cyclical fatigue until failure. It was decided to focus particularly on the stress range that resulted in the greater spread of data 230MPa as this is where sensitisation time appears to have the most effect on the corrosion fatigue properties of AA5456-H116

All figures presented below show typical fracture surfaces for their respective fatigue matrix. The top images of each figure show macroscopic images of the fracture surface observed from the side and top. Circles are used to indicate the position on the fracture surface that the SEM images were taken from and corresponding arrows between SEM images show magnified regions.

4.3.2.2 Full Immersion

Figure 4.14 shows a representative fracture surface from an as-received full immersion AA5456-H116 sample. This sample was the only sample in the as-received condition from both immersion conditions that failed. It is possible that crack initiation takes place at a mechanical defect (below the surface) near the side of a sample at the surface. An area of fracture fatigue, the darker mode I tensile region shown inside the red perforated line on the macroscopic image showing the top of the fracture surface, extends into the material. The rest of the fracture surface shows the typical characteristic microscopic appearance of an overload ductile failure (i.e., large areas of ductile dimple rupture). Microvoids are initiated at interfaces between the matrix and particles (in this case precipitates). They grow under the triaxial stress conditions ahead of the crack tip and expand until they coalesce to leave behind fracture surface with the familiar hemispheroidal surface cavities (i.e. dimples). Near the dimples are some wavy, fine slip lines indicating growth of the dimples by slip.

Figure 4.15 fractograhically documents a full immersion sample, heat treated for 25 hours at 150^0C, subjected to a cyclical stress at 230MPa that resulted in failure after approximately 5,000,000 cycles. It is evident from figure 4.15B where the initiation of crack growth occurred. A close up of this area (figures 4.15C and 4.15D) reveal a large amount of corrosion product indicating localised corrosion present on the surface around the initiation area. It could therefore be assumed that a small surface pit acted as the stress concentration that leads to initiation. There are clear brittle striations present that are parallel to the initiation site, (see figure 4.15C) which is common in samples that have been subjected to corrosion prior to fatigue. Figure 4.15E is a close up of the area highlighted. Figure 4.15C

serves to document more clearly the presence of the brittle striations and also shows the presence of secondary cracking along and slip lines. The secondary cracking is roughly parallel to the initiation site and each other. It is possible that the cracks present run along grain boundaries, which is characteristic of corrosion fatigue. An area of fatigue is outlined on the macroscopic image of the fracture surface via the first red dotted line. It is difficult to substantiate based on the given fractorgrpahs, however it is likely that this is preceded by an area of intergranular crack growth (stage I fatigue) which transitions in to stage II of fatigue signified by the presence of dimples, indicating the beginning of ductile dimple rupture and leading toward final overload or fracture (indicated by the region below the second red dotted line).

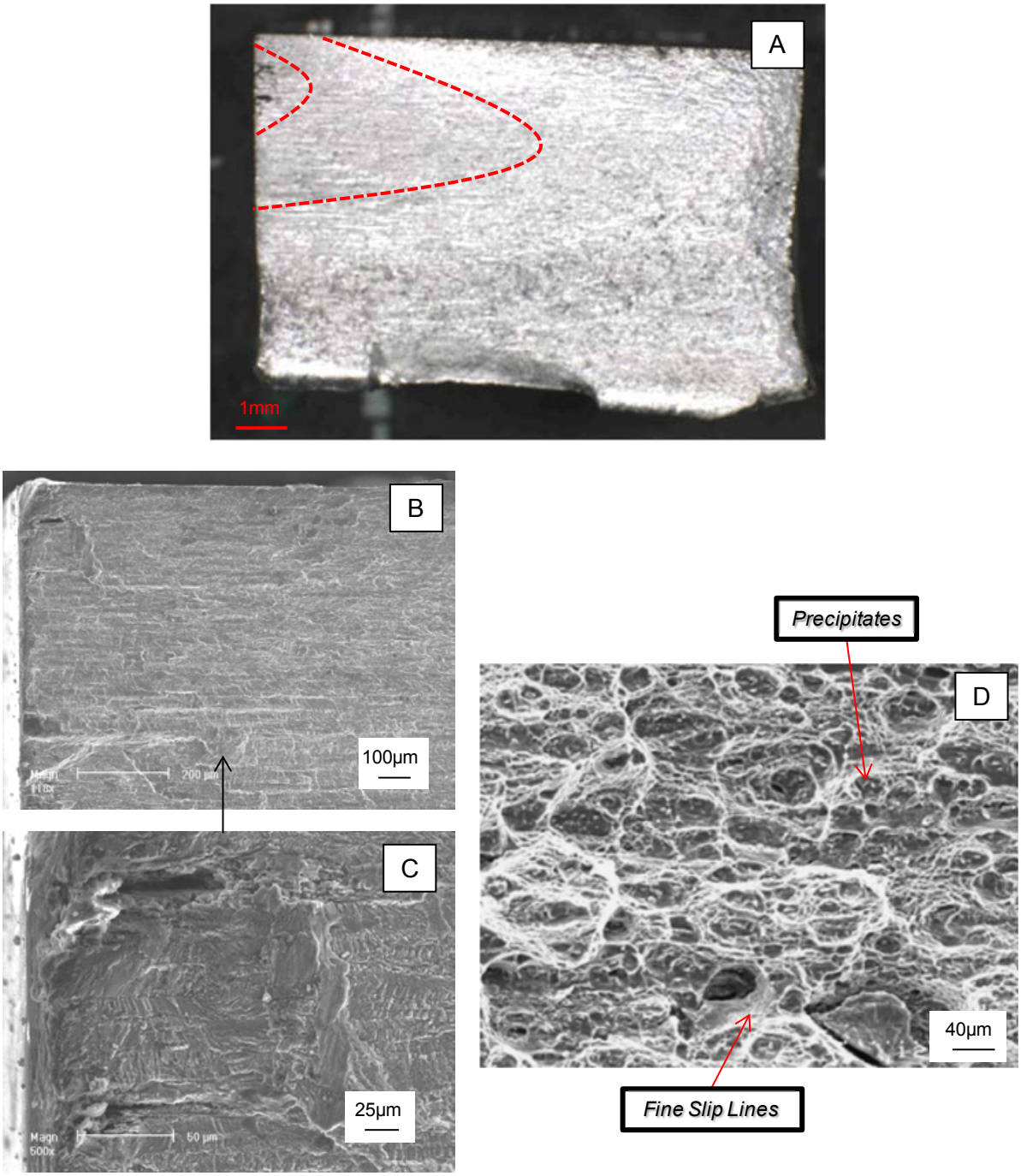

Figure 4.14. SEM images of a typical fracture surface for the AA5456-H116 as-received fatigue samples fully immersed in pH3 3.5% NaCl for 336 hours. This as-received specimen failed after 6,109,430 cycles when subjected to an applied stress of 230 MPa.

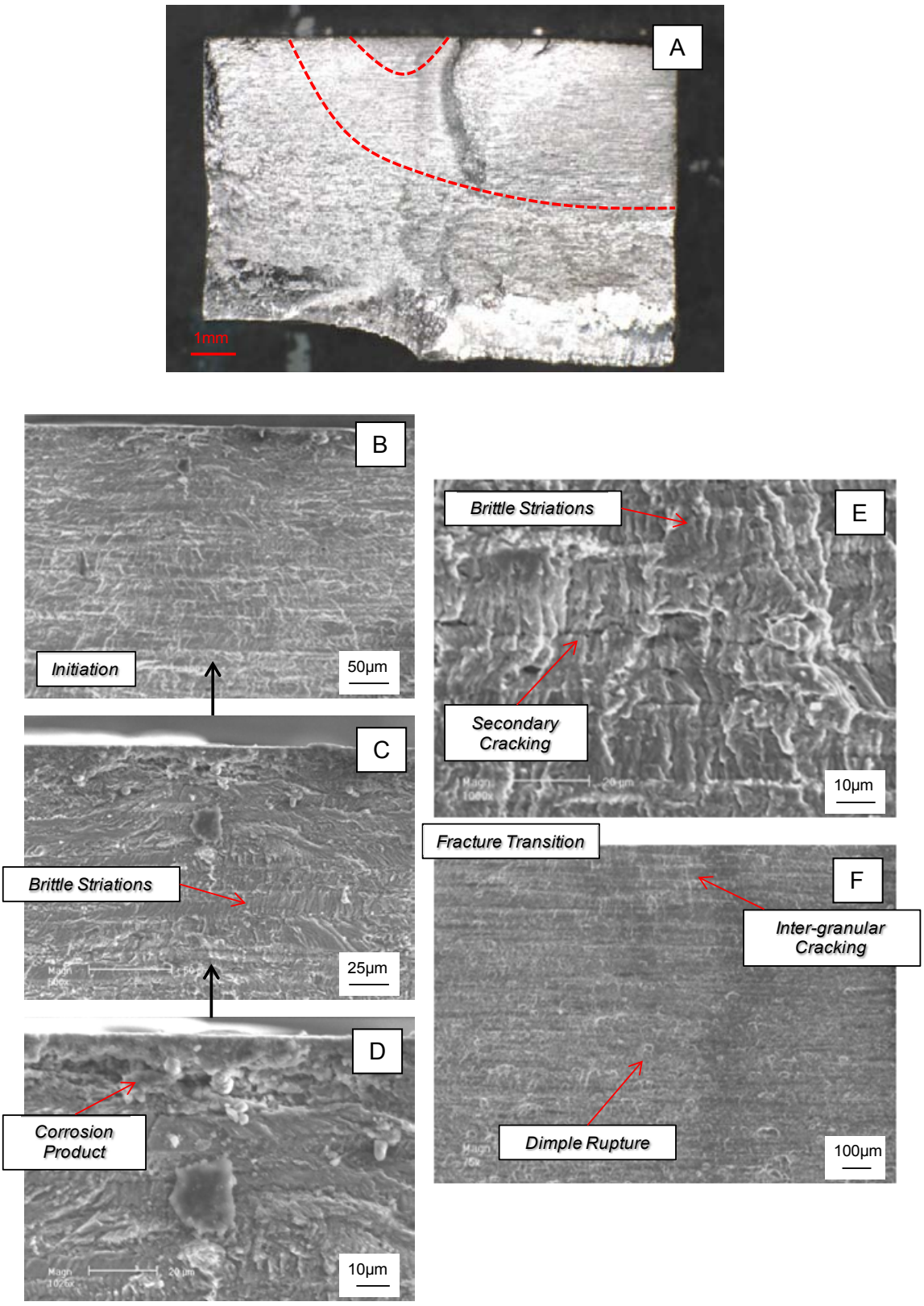

Figure 4.15. SEM images of a typical fracture surface for the AA5456-H116 heated for 25 hours at 150°C,fully immersed in pH3 3.5% NaCl for 336 hours. This specimen failed after 5,968,730 cycles when subjected to an applied force of 230 MPa.

Figure 4.16 shows the fracture surface of a sample aged for 50 hours at 150^0C full immersed in acidified NaCl for 336 hours. The sample failed at approximately 2,000,000 cycles at the same applied stress of 230MPa. The corrosion pit which acted as the initiation site for crack growth is well defined. It is approximately 30μm wide and 20μm deep. Surrounding the pit are the similar brittle striations and faceting common place in brittle fracture. Figure 4.16B shows evidence of secondary cracking close the pit (approximately 100-200μm away from initiation point). It can be assumed that, although the number of cycles to failure was low, the crack was initiated early on (due to the size of the pit) and resulted in the area of fatigue (indicated in figure 4.16A as the area inside the first dotted line). The area surrounding the pit is smaller than previously documented, and it could be possible that a secondary mechanism resulted in the end of fatigue crack growth and the beginning of final overload fracture. Figure 4.16D shows the transition from inter-granular crack growth to trans-granular (the region is identified by the dotted red line on fig. 4.16A). Figure 4.16E illustrates the edge of the fatigue section, where final overload fast fracture took place. It is apparent that the fracture surface is made up of facets representative of fast fracture. There is also a small amount of local - ductile fracture which could have resulted from the presence of large inclusions.

Figures 4.17 document the fracture surface of a full immersion sample sensitised for 100 hours at 150^0C that failed after less than 1,200,000 cycles. The corrosion pit that acted as a stress concentration which resulted in crack initiation is clearly shown in figure 4.17C. It is roughly 30-40μm across and 20μm deep. There are clear uniformly spaced brittle striations running parallel to the corrosion pit indicating corrosion-fatigue. Figure 4.17D shows roughly parallel secondary cracking, possibly at grain boundaries, in an area below the pit. The first dotted line in figure 4.17A shows the area surrounding the pit where fatigue took place. The second dotted line indicates where the fatigue ends and fast fracture begins, most likely in the form of trans-granular crack growth. The shiny ruffled surface toward the bottom of the specimen can be assumed as the site were overload occurs (ductile dimple rupture takes over as the sample completely fractured). This area of ductile dimples and tearing is also clearly shown in figure 4.17F.

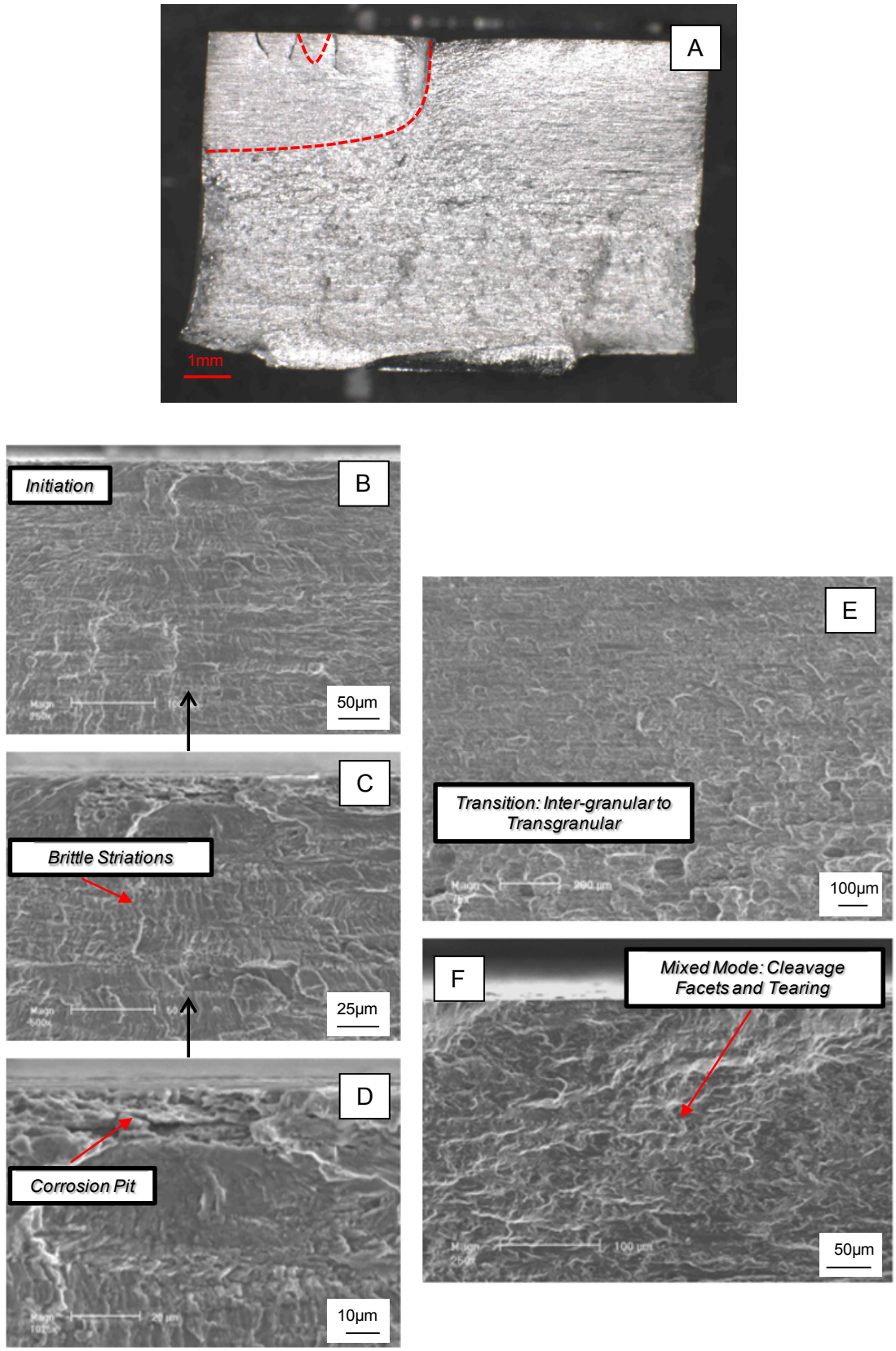

Figure 4.16. SEM images of a typical fracture surface for the AA5456-H116 (50hours at 150°C) fatigue samples fully immersed in pH3 3.5% NaCl for 336 hours. This specimen failed after 2,455,600 cycles when subjected to an applied force of 230 MPa.

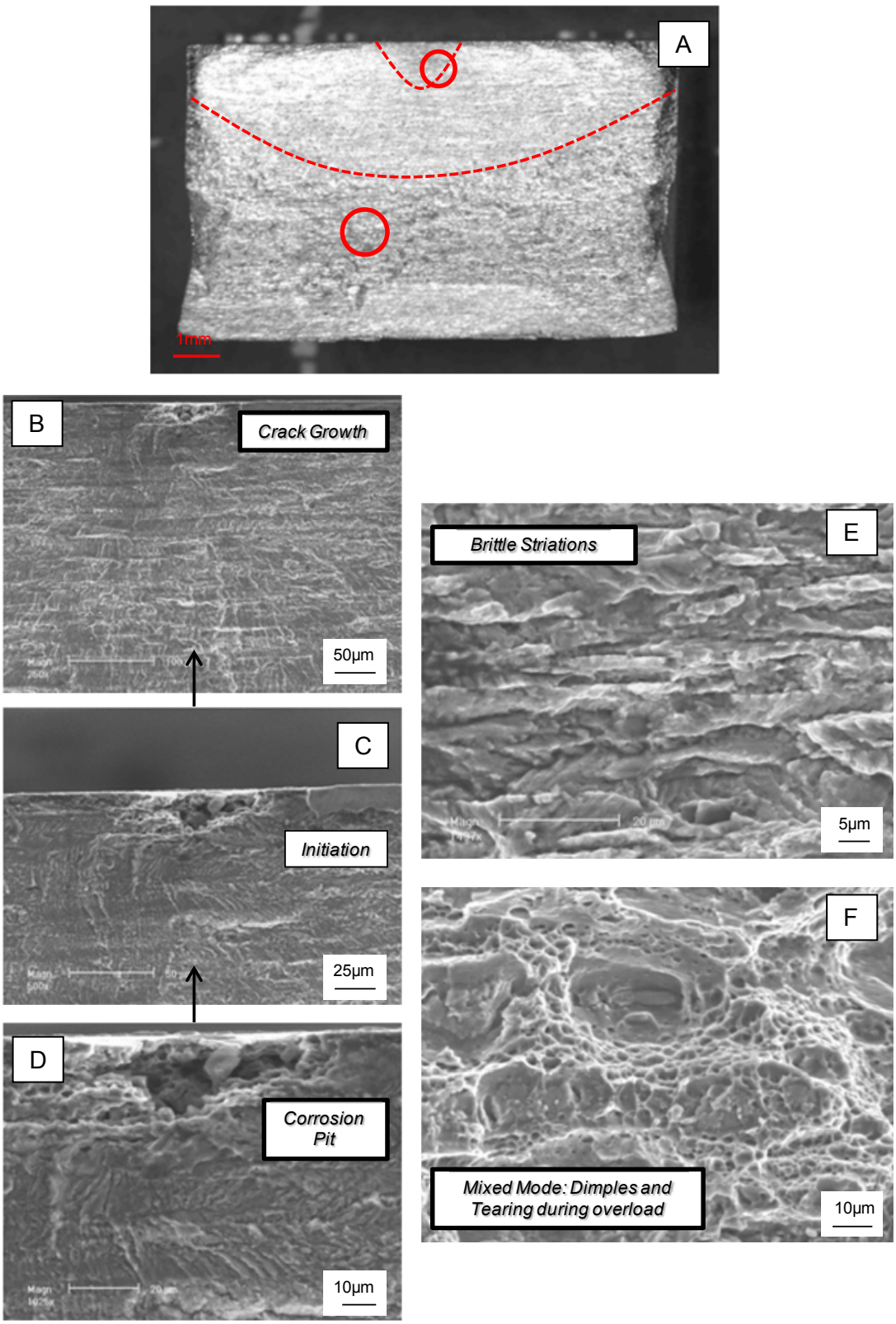

Figure 4.17. SEM images of a typical fracture surface for the AA5456-H116 heated at 150°C for 100 hours, fully immersed in pH3 3.5% NaCl for 336 hours. This as-received specimen failed after 1,246,500 cycles when subjected to an applied force of 230 MPa.

4.3.2.3 Alternate Immersion

Figure 4.18 documents the fracture surface of an as-received sample subjected to alternate immersion. There is a large amount of corrosion product surrounding a small pit of approximately 15μm in width and 10μm in depth. This can be assumed as the area of initiation (indicated by the dull region inside the red perforated line in figure 4.18A). Figure 4.18B documents the presence of brittle 'step-like' striations parallel to the pit indicating corrosion fatigue. The initiation point is surrounded by a shiny mode I tensile region which extends into the material. A close up of the section below the initiation point reveals a fatigue mode transition from intergranular to trans-granular fatigue growth. Below this there is a shiny ruffled section which can be assumed as an area of ductile dimple rupture formed as overload occurred and the sample rapidly fractured. The sample failed after 7,500,000 cycles at 230MPa, which may explain the region of intergranular fatigue which occur after long periods of time subjected to fatigue and corrosion.

Figure 4.19 shows the fracture surface of a sample sensitised for 10 hours at 150^0C and then subjected to alternate immersion for 336 hours. An applied stress of 230 MPa resulted in failure after approximately 2,500,000. The fracture surface shows initiation on the top surface with an area of fracture fatigue extending into the sample (indicated by the first dotted line – figure 4.19A). A close up of this fracture surface reveals that the initiation site contains a large amount of localised surface corrosion (indicated by the corrosion product present in fig 4.19B). This serves to illustrate that the initiation was likely to have occurred from a small surface corrosion pit that was formed during the alternate immersion in acidified 3.5% NaCl. There is clear corrosion fatigue growth into the specimen with brittle striations (figure 4.19D) present near the initiation surface. However the jagged appearance (indicating trans-granular growth) of the site and the shortness of the striations indicate that although corrosion fatigue has occurred the fatigue also took place relatively quickly (see figure 4.19C). Of note are the large number of secondary cracks, possibly at grain boundaries, all of which are more or less parallel. The second dotted line in figure 4.19A indicates where the fatigue ends and fast fracture begins (transfer between Stage I and Stage II fatigue), as shown by the mixed mode of fatigue present in figure 4.19E, whereby on one side there are brittle striations with a clear band of tearing through the middle of the figure. The shiny ruffled surface toward the bottom of the specimen can be assumed as the site were ductile dimple rupture takes over as the sample completely fractured.

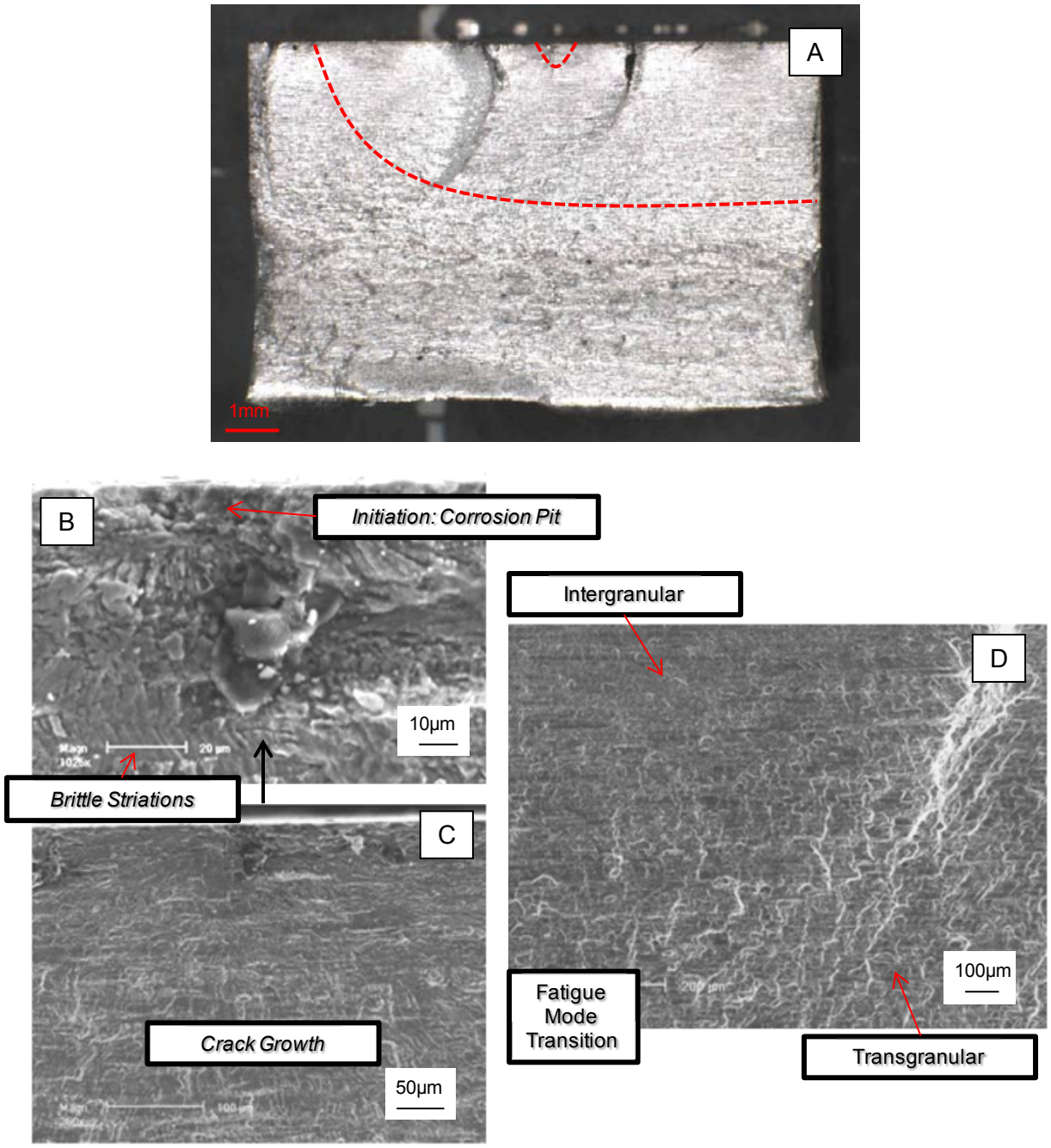

Figure 4.18. SEM images of a typical fracture surface for the AA5456-H116 sensitised for 10 hours at 150°C fatigue samples alternately immersed in pH3 3.5% NaCl for 336 hours. This specimen failed after 7,562,310 cycles when subjected to an applied force of 230 MPa.

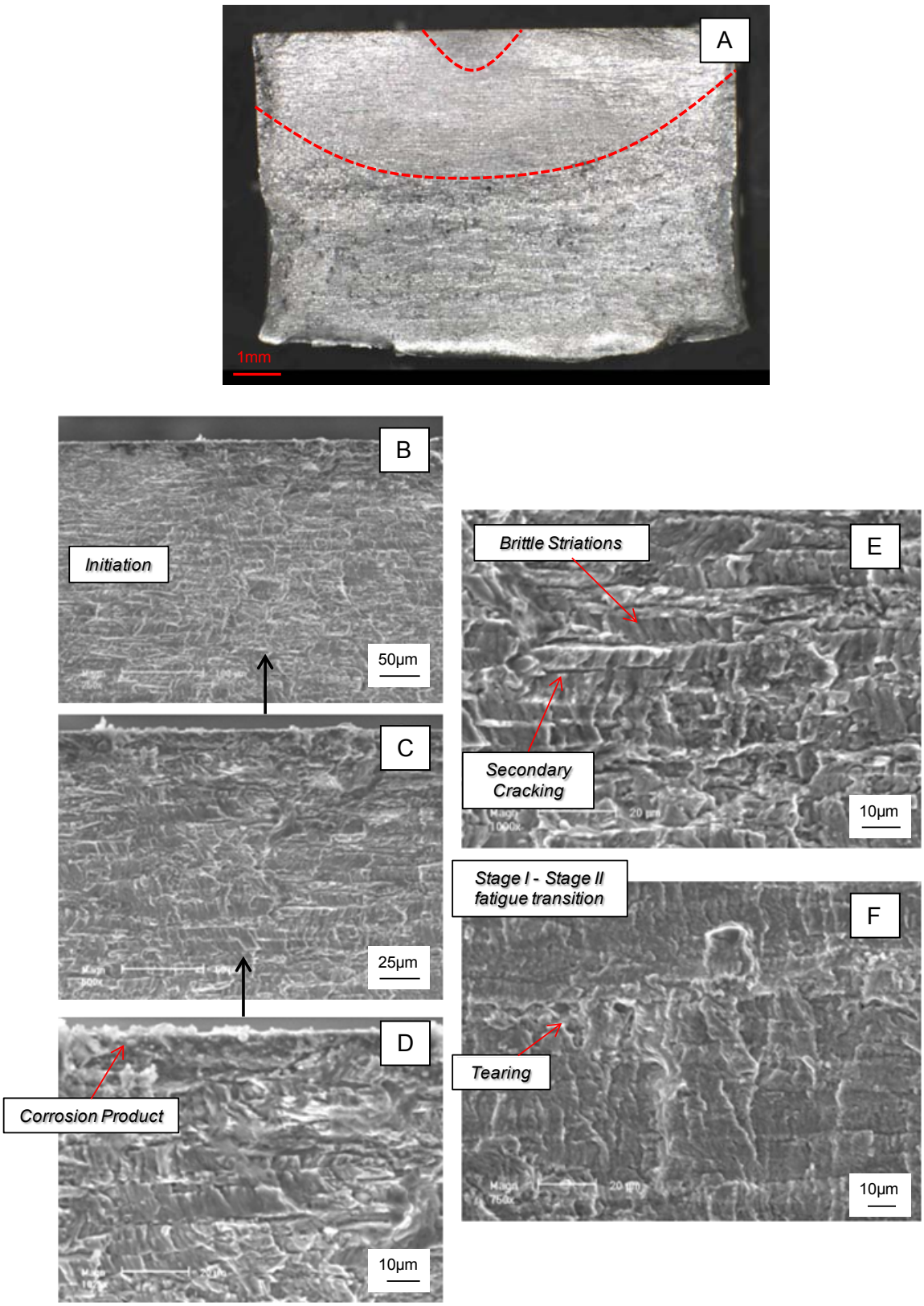

Figure 4.19. SEM images of a typical fracture surface for the AA5456-H116 heated for 25 hours at 150°C fatigue samples fully immersed in pH3 3.5% NaCl for 336 hours. This as-received specimen failed after 2,428,700 cycles when subjected to an applied force of 230 MPa.

Figure 4.20 shows a sample that was sensitised for 50 hours at 150^0C and then subjected to a cyclical stress of 230MPa after alternate immersion. It is clear from the large pit (approx 30-40μm wide and 20μm deep) presented in figure 4.20D where initiation occurred. Figure 4.20A shows the different stages of fatigue and the crack growth into the specimen. The duller areas are where the majority of corrosion-fatigue has taken place (indicated by the area inside the first red perforated line) with the shinny area surrounding the suggesting trans-granular growth (area inside the second red perforated line). Figures 4.20B and C show the area surrounding the initiation site and the fatigue growth into the specimen. It is obvious from close ups (figures 4.20 E and F) that brittle striations are present. This is characteristic of corrosion fatigue and similar to most of the fatigue specimens already presented. Figure 4.20E illustrates that the brittle striations are parallel to grain boundary and the initiation site. As already shown there is a tendency for secondary cracks to form along grain boundaries, resulting in the intergranular brittle striation growth. The shiny ruffled surface toward the bottom of the specimen can be assumed as the site were ductile dimple rupture takes over as the sample completely fractured.

Figure 4.21 represents the fracture surface of a sample sensitised for 100 hours at 150^0C and subjected to the same stress as all the other samples documented. There is a substantial pit located in the middle of the sample, which is approximately 90μm wide and 30μm deep. Figure 4.21B provides a detailed picture of the pit and very close surrounding area; it is obvious that the similar mechanisms of fatigue exist, as brittle striations are present. The area inside the first red dotted line in Figure 4.21A represents the largest area of corrosion fatigue surrounding the initiating pit observed in all the macro images presented previously. Corrosion product is present on the surface of the sample as shown in figure 4.21C, suggesting large amounts of localised corrosion. Figure 4.21E presents evidence of intergranular growth, whilst figure 4.21F documents the transition from stage II fatigue (trans-granular growth) to final overload fracture in the form of ductile dimple rupture.

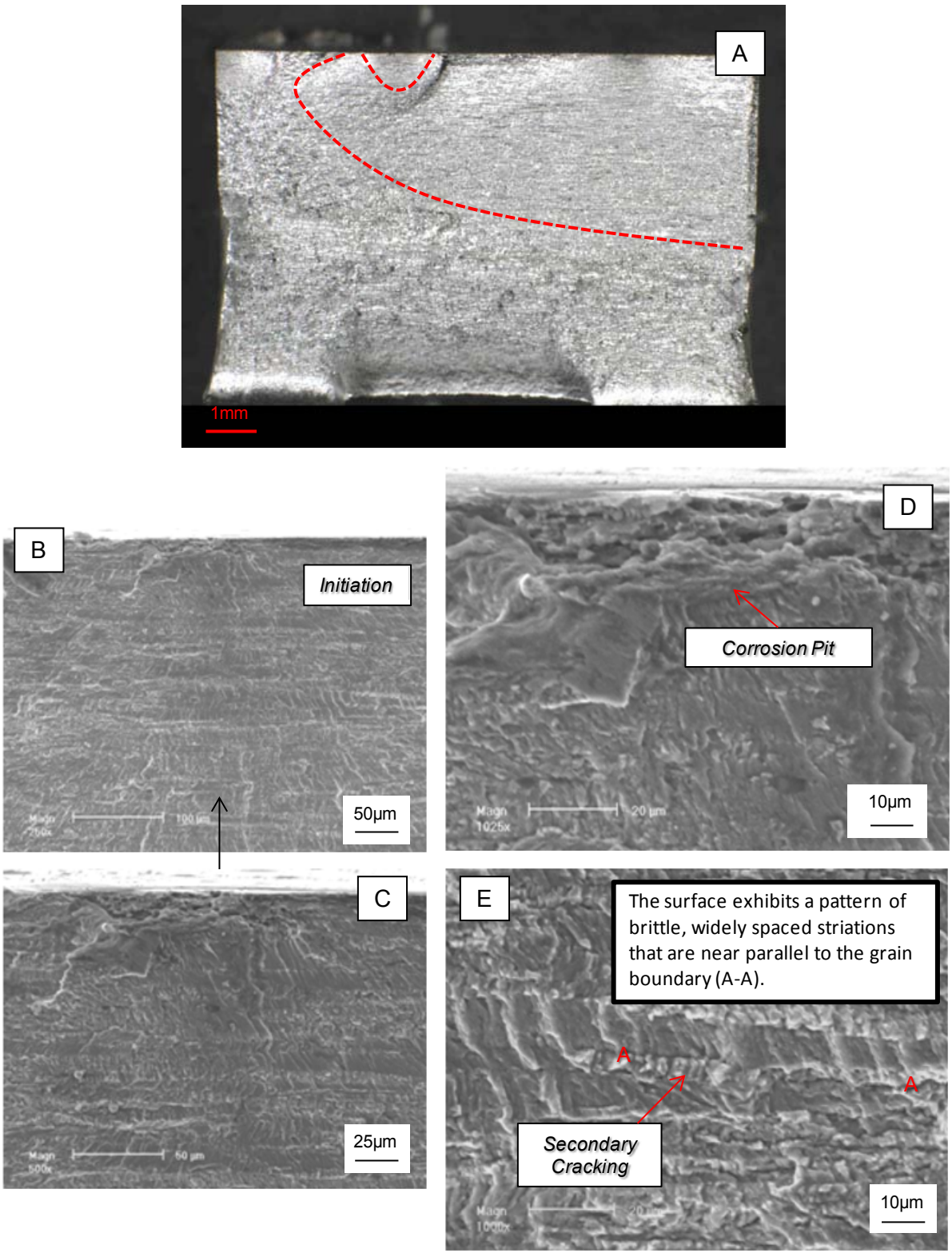

Figure 4.20. SEM images of a typical fracture surface for the AA5456-H116 sensitised for 50 hours at 150°C fatigue samples alternately immersed in pH3 3.5% NaCl for 336 hours. Tthis specimen failed after1,186,200 cycles when subjected to an applied force of 230 MPa.

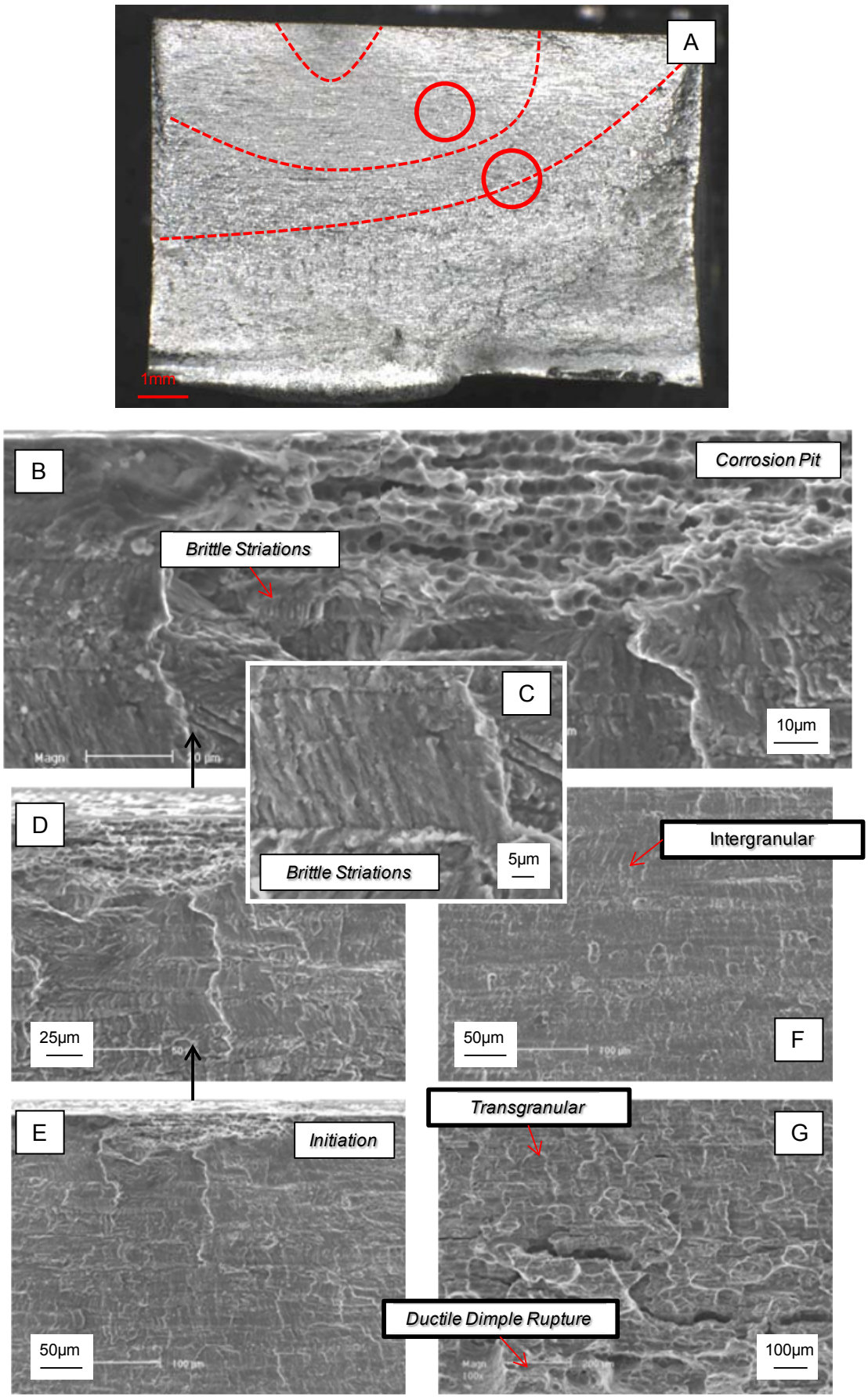
A
1mm
B
Corrosion Pit
Brittle Striations
C
10µm
Brittle Striations
5µm
D
Intergranular
25µm
50µm
F
E
Initiation
Transgranular
G
Ductile Dimple Rupture
50µm
100µm

Figure 4.21. SEM images of a typical fracture surface for the AA5456-H116 sensitised for 100 hours at 150°C fatigue samples fully immersed in pH3 3.5% NaCl for 336 hours. This specimen failed after 296,870 cycles when subjected to an applied force of 230 MPa. (Needs to be on previous page)

4.3.3 Discussion

It can be seen in all the results presented in section 4.3 that there is a clear relationship that has developed between sensitisation time and its effect on the corrosion fatigue properties of AA5456-H116. The longer the sensitisation time at 150^{0}C the greater the extent of corrosion (i.e. greater pit size and depth) which cause a reduction in the fatigue lifetime. This can be attributed to the mechanisms of sensitisation that results in the formation of anodically reactive β precipitation at grain boundaries, as shown by various studies[5, 7, 11, 21]. Jones et al. concluded that increased β-phase precipitation at the grain boundaries of AA5083 as a result of thermal aging for 100 hours at 175^{0}C results in more than 5 times an increase in the crack-growth rate[5]. The resulting effects of precipitation in AA5456-H116 causes a reduction in the corrosion resistance (see NAMLT results in section 4.2), this in turn decreases the fatigue lifetime due to the increase in the number of stress risers (i.e. pits) present that can more readily lead to the initiating of a crack and eventually failure. The β precipitation of AA5456-H116 is increased by an increase in the sensitisation time up to a maximum that differs for various alloys, as shown by numerous studies [21, 22, 51]. In this study the longer sensitisation times of 50 hours and 100 hours produced a marked increase in the number of pits (i.e. pit density) and more aggressive pitting (i.e. greater pit depth), as documented in section 4.2.

This decrease in the corrosion fatigue properties as sensitisation time at 150^{0}C increases is well reflected in the fractographic examination presented in the section above, whereby the increased sensitisation times exhibit greater areas of corrosion fatigue (brittle striations and intergranular crack growth) and larger initiating pits. The fatigue lifetimes also diminish accordingly.

It is possible that the pits that have initiated the crack that lead to failure are comparable with the maximum pit depths observed in section (4.2), indicating that the larger pits on the surface of the specimens act as the initiation sites for crack growth. For example, looking at figure 4.21 the pit depth appears to be approximately 35μm to 40μm deep. From table 4.2 we can see that the maximum pit depth recorded via optical documentation for 100hours at 150^{0}C prior to alternate immersion is 34.5μm. Another example that compares with the pit documentation data is the 50 hours at 150^{0}C full immersion specimen shown in figure 4.16. The pit depth is approximately 20μm deep which although it is not the maximum pit depth observed for this particular specimen condition is still greater than the average pit

depth recorded for that specimen condition (see table 4.2). At lower sensitisation times this correlation becomes difficult due to the higher number of cycles to failure and the smaller initiating pits. It can be seen for the as received sample alternately immersed that the approximate pit depth is 10μm although it is difficult to examine due the surrounding corrosion product. However, the maximum pit depth observed for that condition was 12μm. It must also be noted that the pit volumes and surface area also increase with increasing sensitisation time along with type of immersion. Alternate immersion as already discussed in section 4.2 produces larger pit sizes and densities due to the more aggressive environment created during immersion. Nevertheless, to fully understand the causes of failure and the effects of sensitisation and subsequent corrosion it is important that typically large pits present on the surface of the sensitised specimens are fully documented. This will be completed using confocal laser scanning microscopy, which will provide pit volumes, surface areas and 3D mapping.

4.4 Pit Morphology

After comparing the fatigue micrographs and the relevant corrosion data it is evident that the largest pits present on the surface of the material act as the initiation sites for crack growth and ultimately failure (see section 4.3). It was decided that a more detailed documentation of the morphology of such pits should be undertaken. All heat treatment conditions were examined and pit surface area, volume and area ratio (density) were measured (see section 3.7).

4.4.1 Confocal Laser Scanning Microscopy of Immersion Specimens

As-received and heat treated specimens were full immersed in a 3.5% NaCl acidified to pH3 with HCl for a period of 336 hours. Samples were also subjected to an alternate immersion for the same 336 hour period in the same in order to compare the effects of the two different types of immersion (see section 3.2 for sample preparation). Three randomly selected areas across the plate surface (T-L Plane – see figure 4.1A) were selected for confocal laser scanning microscopy (CLSM) pit documentation, which examined the total number of pits in a given area, the total area of pits, the average pit volume and the area ratio (calculated using equation 3.2). However, to document fully the type of pitting that results in crack initiation, larger pits that were selected and examined in greater detail. Below is a table that shows the results obtained from the selected pits. Despite this approach it must be made clear that the surface of the specimen did not wholly comprise large pits. Table 4.4 documents the following confocal micrographs for the selected pits (complete CLSM results including all selected areas are shown in table in A1.3).

Table 4.4 Table showing the CLSM summary of total number of pits measured, total area of pits and area ratio (see section 3.3.1).

Sample Identification	Total number of Pits	Total Area of Pits [μm^2]	Average Pit Area [μm^2]	Average Pit Volume [μm^3]	Average Pit Volume/No. Pits [μm^3]	Area ratio[%]
As-Received Full Immersion	5	34.9	7.0	2.8	0.6	0.286
As-Received Alternate Immersion	6	67.8	11.3	2.1	0.3	0.555

10hrs – 150^{0}C Full Immersion	8	68.6	8.6	3.7	0.5	0.561
10hrs – 150^{0}C Alternate Immersion	8	101.8	12.7	6.2	0.8	0.833
25hrs – 150^{0}C Full Immersion	15	305.2	20.3	8	0.5	2.497
25hrs – 150^{0}C Alternate Immersion	10	604.1	60.4	36.6	3.7	4.942
50hrs – 150^{0}C Full Immersion	19	923.2	48.6	41.8	2.2	7.553
50hrs – 150^{0}C Alternate Immersion	11	1022.5	93	96.8	8.8	8.365
100hrs – 150^{0}C Full Immersion	5	1154.4	230	115.5	23.1	9.445
100hrs – 150^{0}C Alternate Immersion	12	1388.4	115.7	237.3	19.8	11.359

4.4.1.2 Pitting Morphology of Full Immersion Specimens

Optical micrographs taken using a confocal laser scanning microscope (CLSM) (see section 3.6.2) reveal that there is a difference in the corrosion morphology when comparing the different heat treatments. Below are selected confocal micrographs that show the most extensive pitting present on the plate surface (T-L plane – see figure 4.1A) of each heat treated sample (see appendix A.1.3 for representative confocal work). Figures 4.22 represents the as-received full immersion specimens after the corrosion product was removed via ultrasonic cleaning in de-ionised water. There is a small group of pits, the largest being approximately 15μm^2 in area and the smallest being less than 1μm^2 in area. The combined area of all the pits, calculated using CLSM, is 34.9μm^2. The total area rate as a percentage was calculated (see section 3.3) as 0.286%.

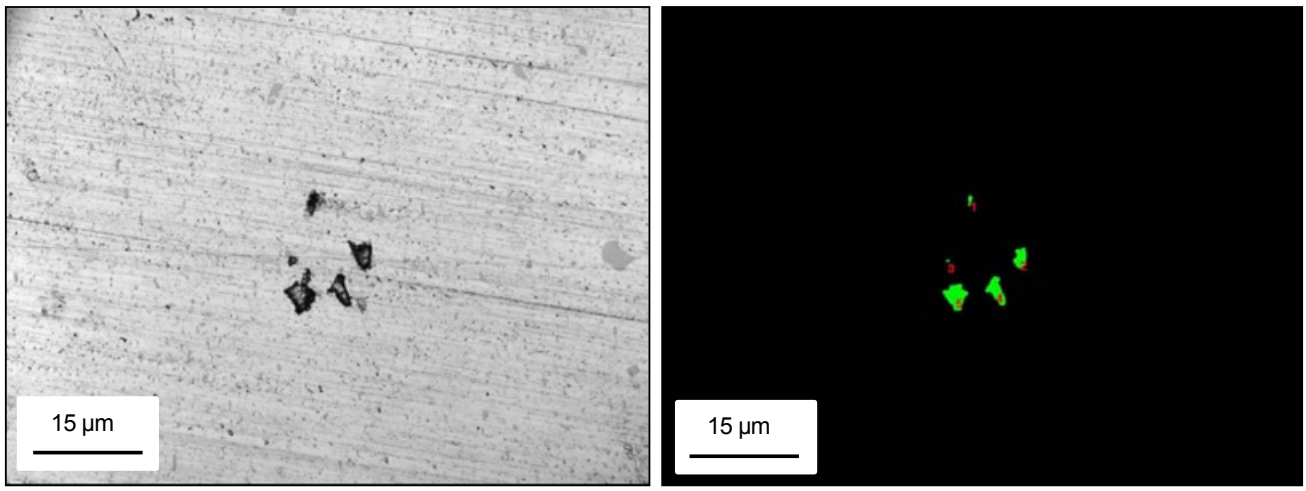

Figure 4.22 A and B. A) Showing a group of pits on the surface of an as-received specimen fully immersed in pH3 NaCl for 336 hours. B) A binary representation of the pits that were measured by CLSM.

Figures 4.23 documents the pit morphology of a specimen heat treated at 150^0C for 10 hrs after 336 hrs full immersion in pH3 3.5% NaCl after the corrosion product was removed via ultrasonic cleaning in de-ionised water. There is a small, yet recognisable difference between the heat treated and as-received samples. The pit size is very similar with the largest being approximately 14µm^2 in area and the smallest being 1.2µm^2 in area. When comparing the total area of pits divided by the number of pits it appears that the extent of pitting is relatively similar.

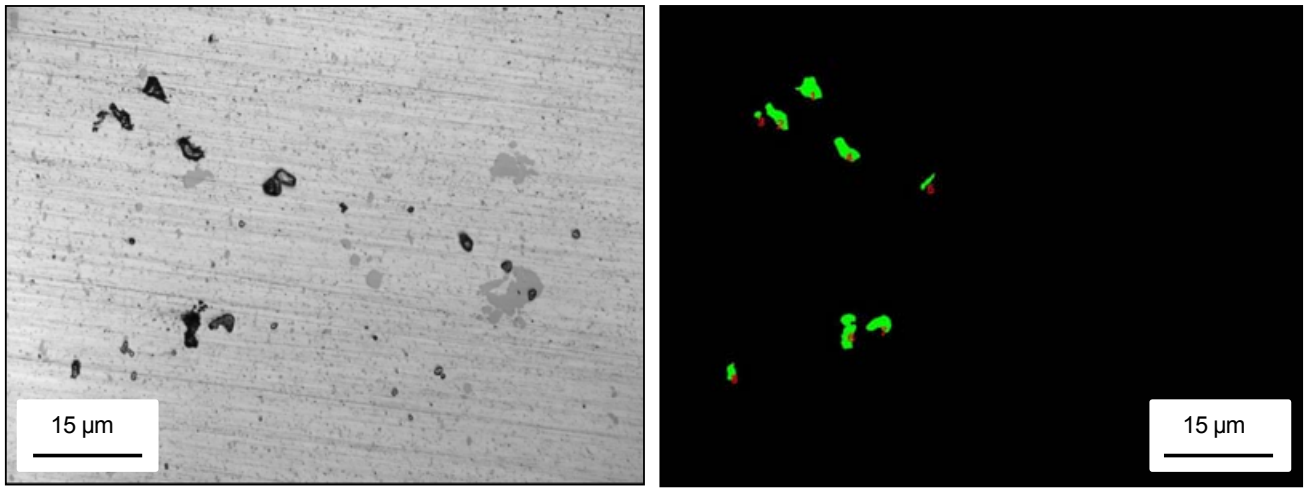

Figure 4.23 A and B. A) Showing a group of pits on the surface of a sample heated for 10 hours at 150°C specimen fully immersed in pH3 NaCl for 336 hours. B) A binary representation of the pits that were measured by CLSM.

Figures 4.24 documents the pit morphology of a specimen heat treated at 150^0C for 25 hrs after 336 hrs full immersion in pH3 3.5% NaCl. There is a large difference between the pit morphology of this heat treatment when compared to the as-received and 10 hour heat treatment at 150^0C. The pit size is much greater, the largest being 102μm^2 in area with the average size approximately 20μm^2. The average pit density and pit depth also increase by a significant amount (see table 4.2). It is clear that pitting is more severe for the longer heat treatment when compared with the as-received and 10 hour heat treatment.

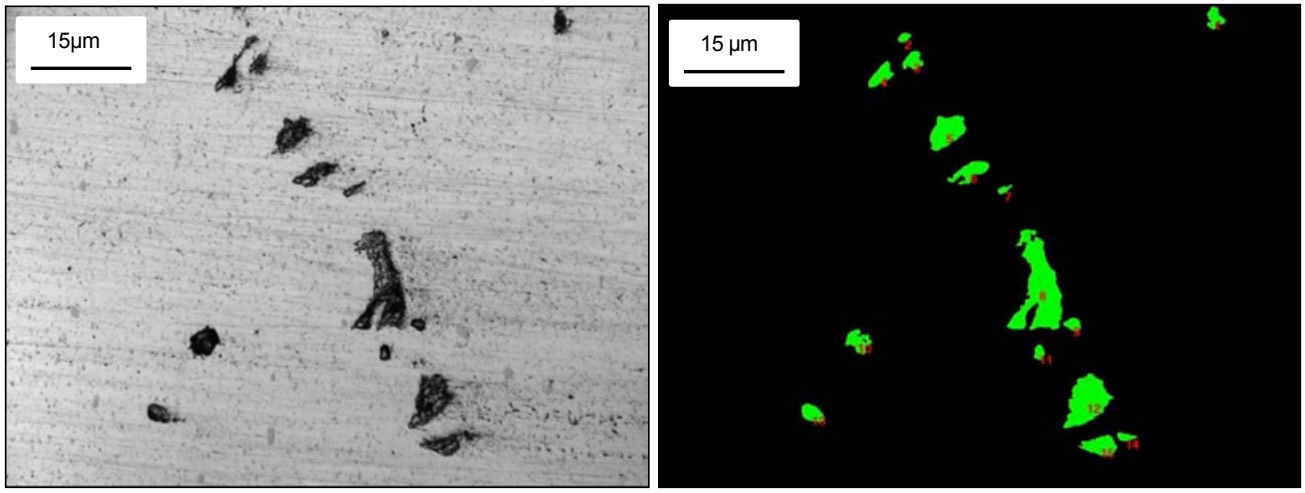

Figure 4.24 A and B. A) Showing a group of pits on the surface of a sample heated for 25 hours at 150°C specimen fully immersed in pH3 NaCl for 336 hours. B) A binary representation of the pits that were measured by CLSM.

Figure 4.25 shows the same area as that presented in figure 4.24; however it has been etched for 30 seconds in Keller's reagent to reveal the microstructure. It can be seen that some of the pit boundaries follow the grain boundaries, possibly suggesting inter-granular corrosion (IGC) combined with pitting. However, the distribution of pits is still mostly random (similar to the two previous aging conditions).

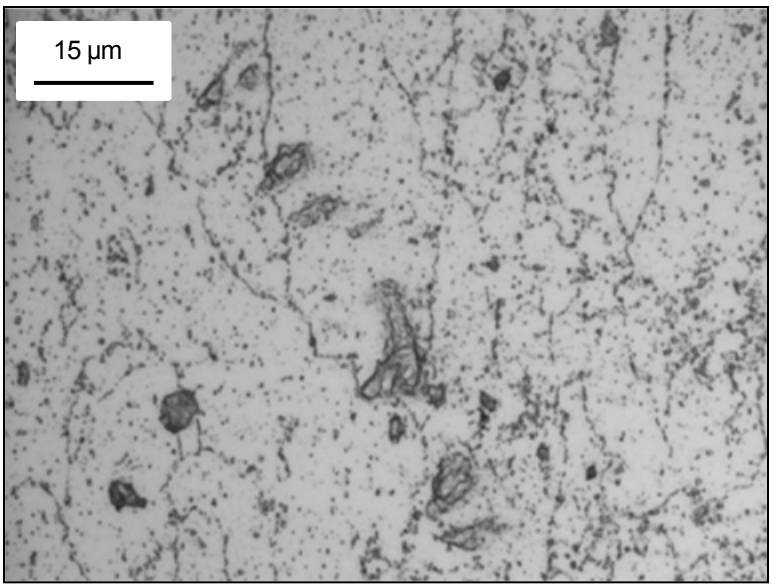

Figure 4.25 Represents that same surface area as presented in figure 4.24 after Keller's etching to reveal the microstructure.

Figure 4.26 is a 3D wire representation of the same area. The colour scale indicates that the depth of the pit is approximately around 4-5µm, which is similar to the average pit size of the 25hrs at 150^{0}C heat treatment (see table A1.1).

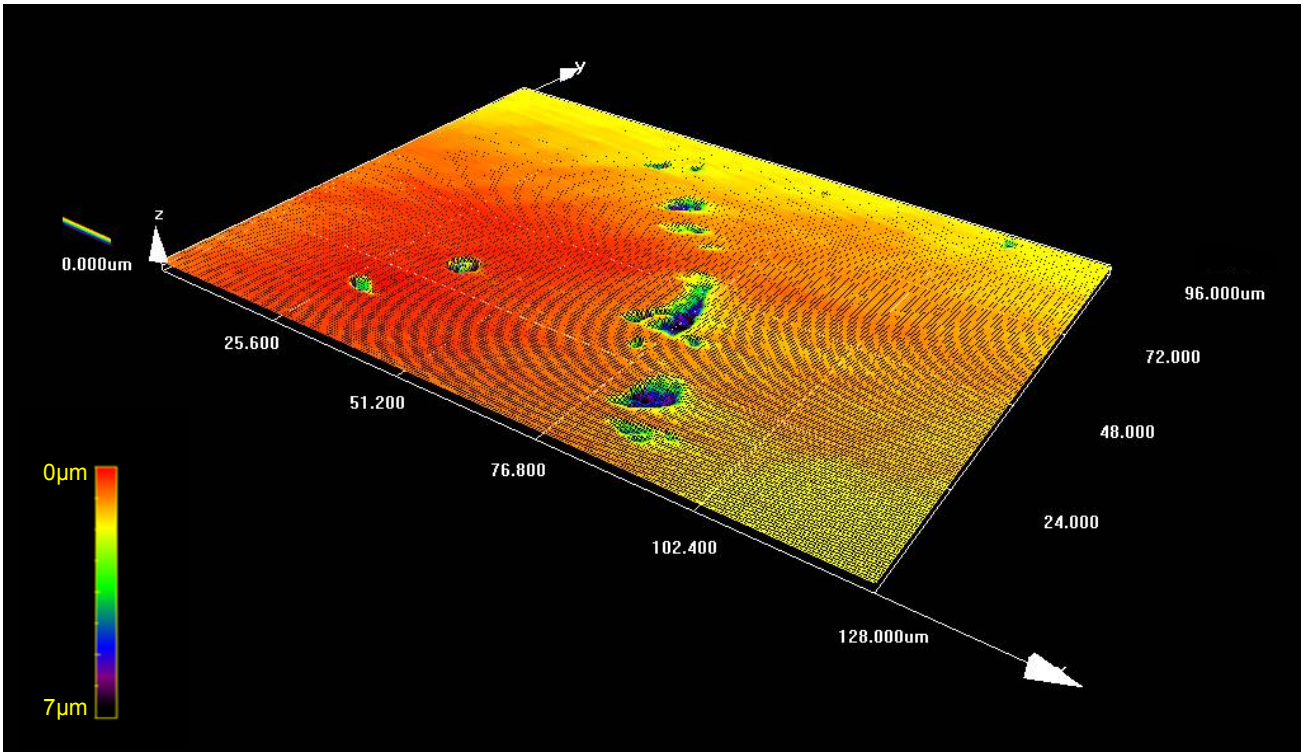

Figure 4.26. A 3D wire representation of the same are documented in figure 4.24 taken using CLSM.

Figures 4.27 document the pit morphology of a specimen heat treated at 150^{0}C for 50 hours after 336 hrs full immersion in pH3 3.5% NaCl. There is a large difference between the pit morphology of this heat treatment when compared to the previous aging times at 150^{0}C. The pit size is much greater, the largest being 880μm^2 in area with the average size approximately 50μm^2. As expected the average pit density and depth increase, however this increase is more considerable than the previous three heat treatments (see table 4.2).

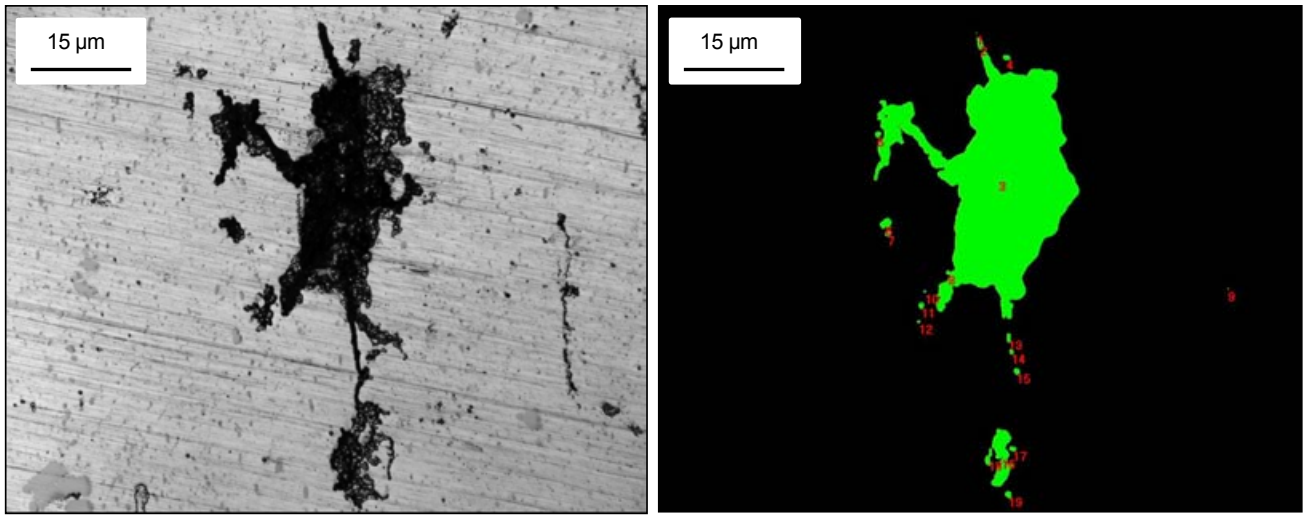

Figure 4.27 A and B. A) Showing a group of pits on the surface of a sample heated for 50 hours at 150^{o}C specimen fully immersed in pH3 NaCl for 336 hours. B) A binary representation of the pits that were measured by CLSM.

Figure 4.28 shows the same area as that presented in figure 4.27, however it has been etched for 30 seconds in keller's reagent to reveal the microstructure. It can be seen that most of the pit boundaries follow the grain boundaries, suggesting inter-granular corrosion (IGC) combined with pitting. It can be assumed that pits have initiated and then grown along grain boundaries, joining other pits in close proximity.

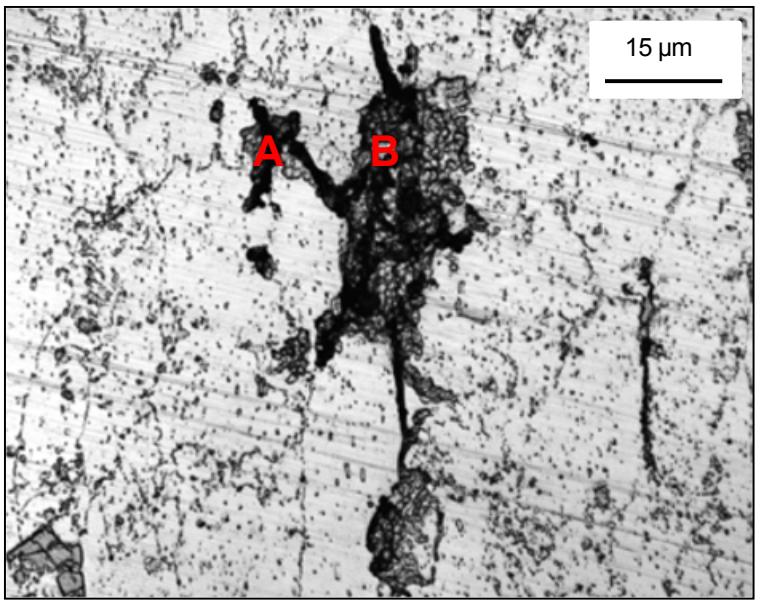

Figure 4.28. Represents that same surface area as presented in figure 4.27 after Keller's etching to reveal the microstructure.

A profile of an adjacent cross section of the specimen is shown in Figure 4.29. To produce this cross section, a vertical section was made through the pit above and optical micrographic pictures were taken. It can be seen that pit growth is relatively wide and shallow. It can also be seen in pit B that there is a small amount of horizontal growth occurring, possibly along a grain boundary. Because of the nature of the sensitisation and immersion time and period it can be assumed that extensive pitting has occurred; however the growth of the pit beneath the surface is not extensive.

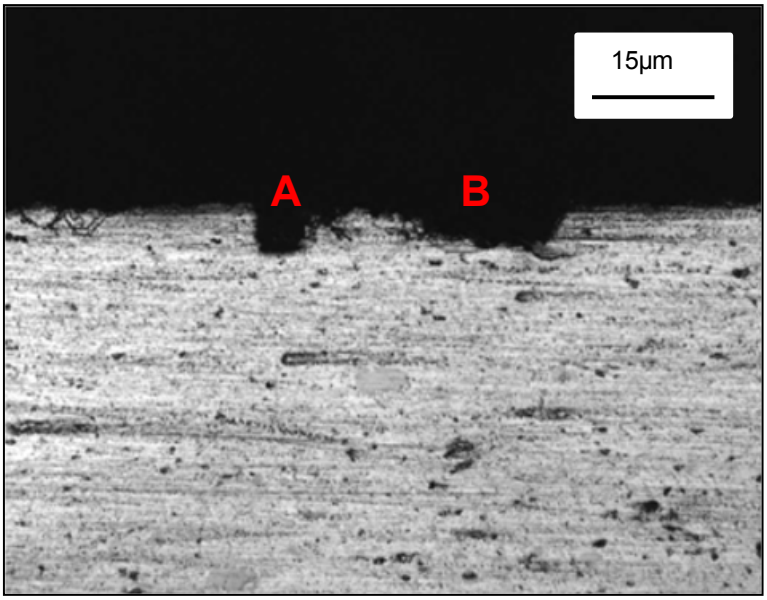

Figure 4.29 Represents that same surface area as presented in figure 4.27 after Keller's etching to reveal the microstructure.

Figure 4.30 is a 3D wire representation of the same area. The colour scale indicates that the depth of the pit is roughly around 15µm, which is greater than the average pit size of the 50hrs at 150°C heat treatment (see table 4.2).

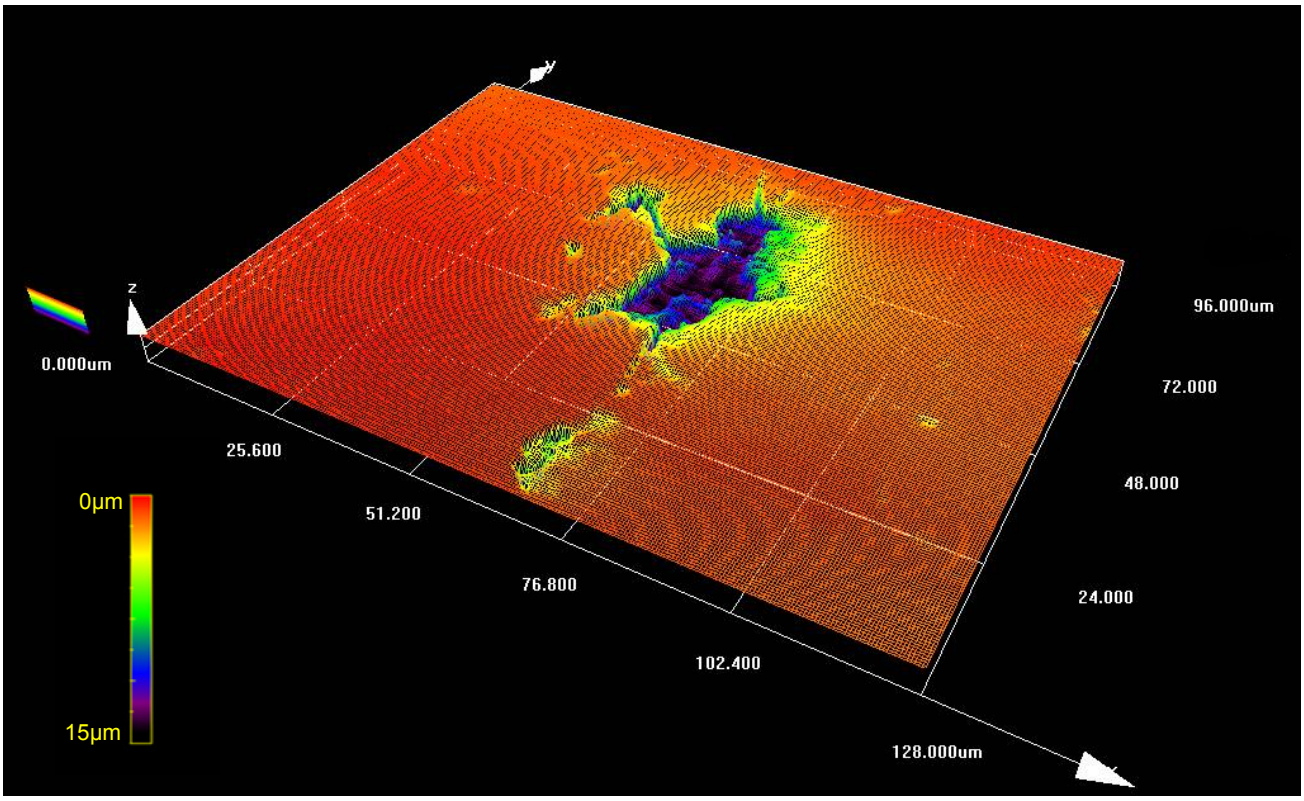

Figure 4.30. A 3D wire representation of the same are documented in figure 4.27 taken using CLSM.

Figures 4.31 documents the pit morphology of a specimen heat treated at 150^{0}C for 100 hrs after 336 hrs full immersion in pH3 3.5% NaCl. Again similarly to the full immersion, there is a degree of similarity when compared to the 50hrs at 150^{0}C. The pit size is much greater than that of the as-received, 10hrs and 25hrs at 150^{0}C conditions, it appears that various smaller pits have grown and joined together to form a pit that covers the majority of the surface area. The area rate was calculated to be 9.445%, the maximum of all the other heat treatments that underwent full immersion in pH3 3.5% NaCl. The average pit density and pit depth are also the largest (see table 4.2). This clearly demonstrates that pitting is the most severe for the longest heat treatment. Samples held at 150^{0}C for 50hrs are seriously compromised when immersed in acidic chloride environments.

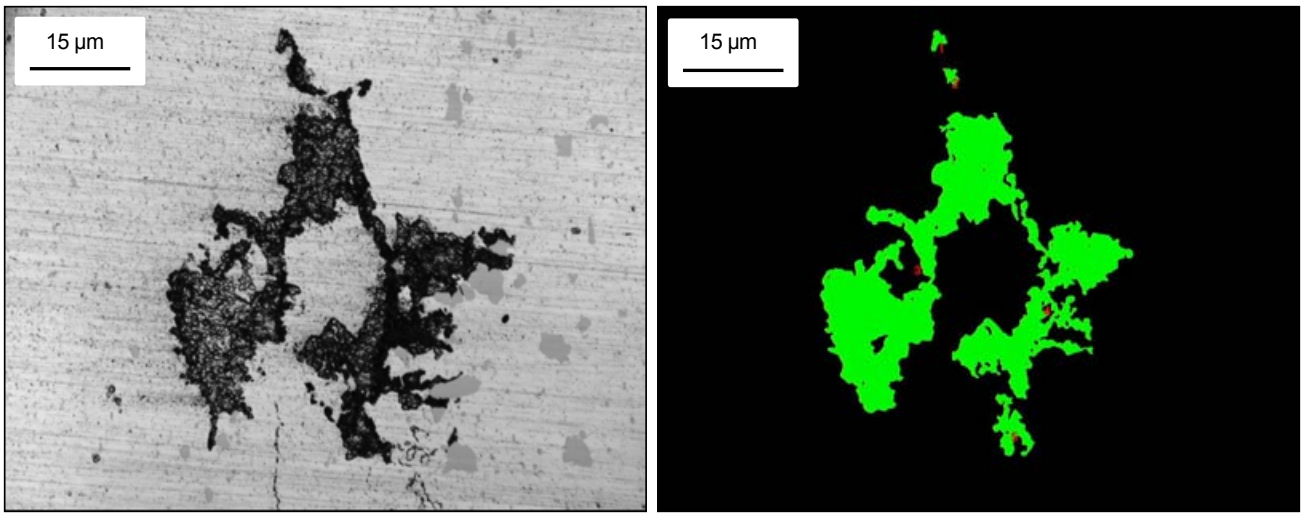

Figure 4.31 A and B. A) Showing a group of pits on the surface of a specimen sensitised for 100 hours at 150°C, fully immersed in pH3 NaCl for 336 hours. B) A binary representation of the pits that were measured by CLSM.

Figure 4.32 represents an etched microstructure of the same area represented in figure 4.16. It is clear that the pits have grown along grain boundaries to join up with other adjacent pits, suggesting pitting and IGC. It could also suggest that whole grains have been corroded away, due to the severe nature of pitting that occurs on samples of this heat treatment.

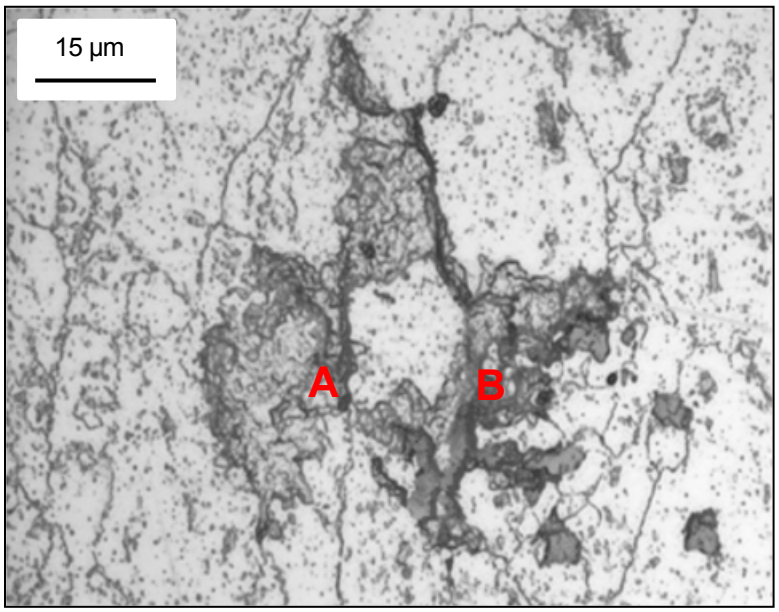

Figure 4.32. Represents that same surface area as presented in figure 4.31 after Keller's etching to reveal the microstructure

A profile of an adjacent cross section of the specimen is shown in Figure 4.33. To produce this cross section, a vertical section was made through the pit above and optical micrographic pictures were

taken. It is evident that the pits have coalesced. According to ASTM standard G 46-94 [70] (Standard Practice for Examination and Evaluation of Pitting Corrosion) the two separate pits (indicated as A and B in both figures 4.32 and 4.33) have joined beneath the surface of the material through horizontal pit growth. Pit growth has quite clearly undercut the surface joining the two pits A and B.

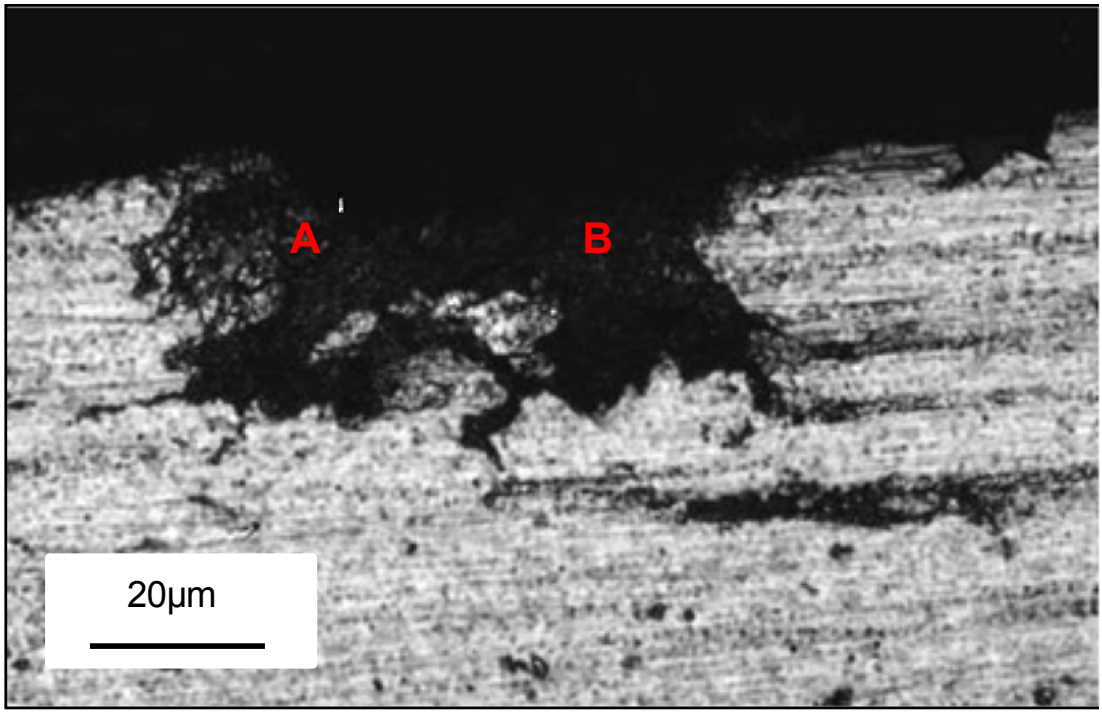

Figure 4.33 Represents that same surface area as presented in figure 4.31 after Keller's etching to reveal the microstructure

Figure 4.34 is a 3D wire representation of the same area. The colour scale indicates that the depth of the pit is roughly around 15µm, which is greater on the average pit depth of the 100hrs at 150^{0}C heat treatment (see table 4.2). The areas of deep attack represent where discrete pits have nucleated first, yet, with increasing exposure time pit coalescence took place to cause more extensive, larger areas of localised attack.

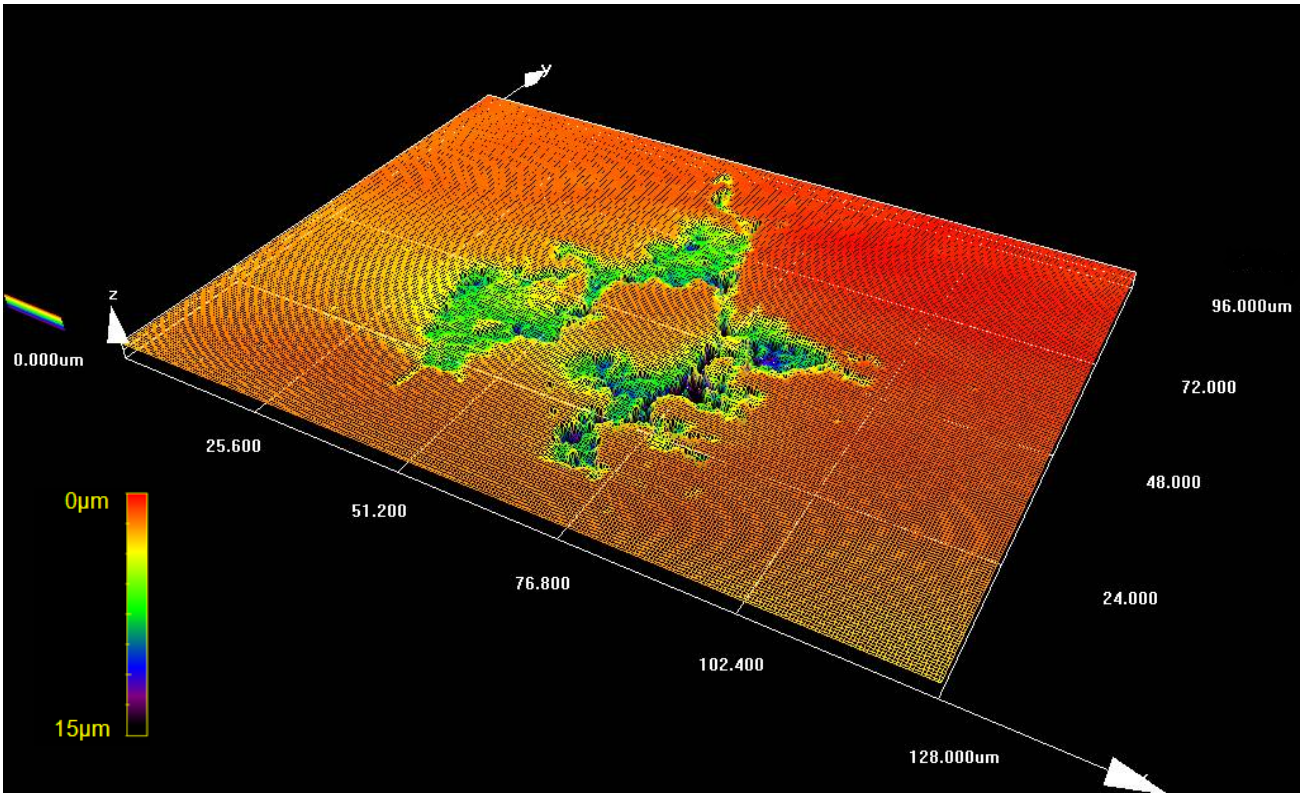

Figure 4.34. A 3D wire representation of the same are documented in figure 4.31. taken using CLSM.

4.4.1.2 Pitting Morphology of Alternate Immersion Specimens

Figures 4.35 represents the as-received alternate immersion specimens after the corrosion product was removed via ultrasonic cleaning in de-ionised water. There is a small group of pits, the largest being approximately 21µm in area and the smallest being less than 2.5µm^2 in area. The combined area of all the pits, calculated using CLSM, is 67.8µm^2. The total area rate as a percentage was calculated (see section 3.3) as 0.555%.

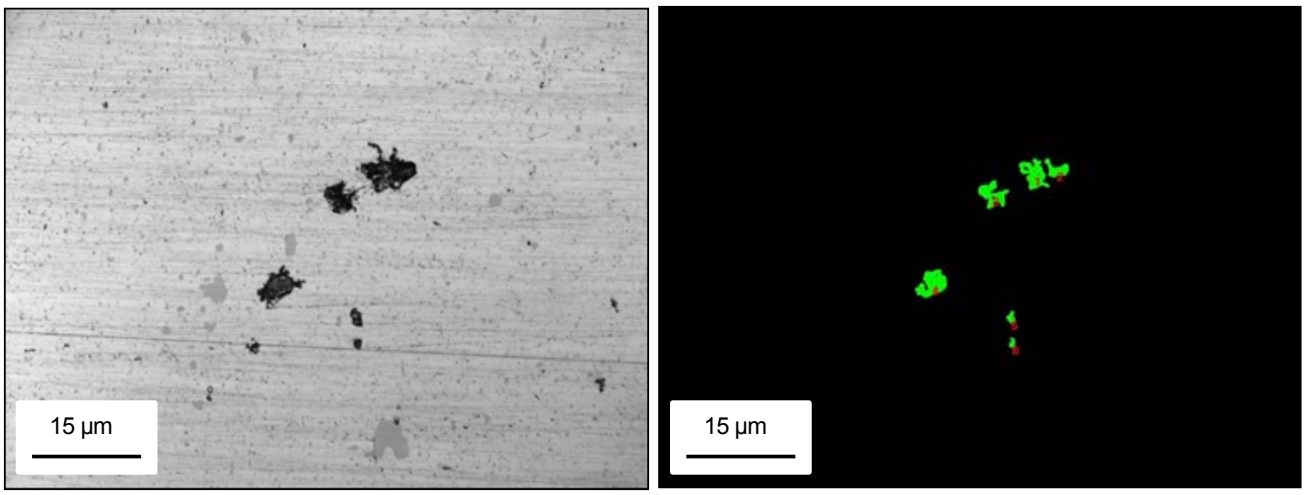

Figure 4.35 A and B. A) Showing a group of pits on the surface of an as-received specimen alternately immersed in pH3 NaCl for 336 hours. B) A binary representation of the pits that were measured by CLSM.

Figures 4.36 documents the pit morphology of a specimen heat treated at 150^0C for 10 hrs after 336 hrs alternate immersion in pH3 3.5% NaCl. Much like the full immersion specimens there is an increase in corrosion between the heat treated and as-received samples. The pit size is very similar to that of the as-received with the largest being approximately 21µm^2 in area and the smallest being 1.5µm^2 in area. However, the combined area of the total pitting shows a large increase when compared to that of the as-received sample (101.8µm^2), the total area rate also shows an increase to 0.833%. When comparing the calculated pit densities over a 12mm^2 there is an increase of 2pits/mm^2 (see table 4.3). Using the average pit depth it is clear that the extent of pitting is very similar for these conditions.

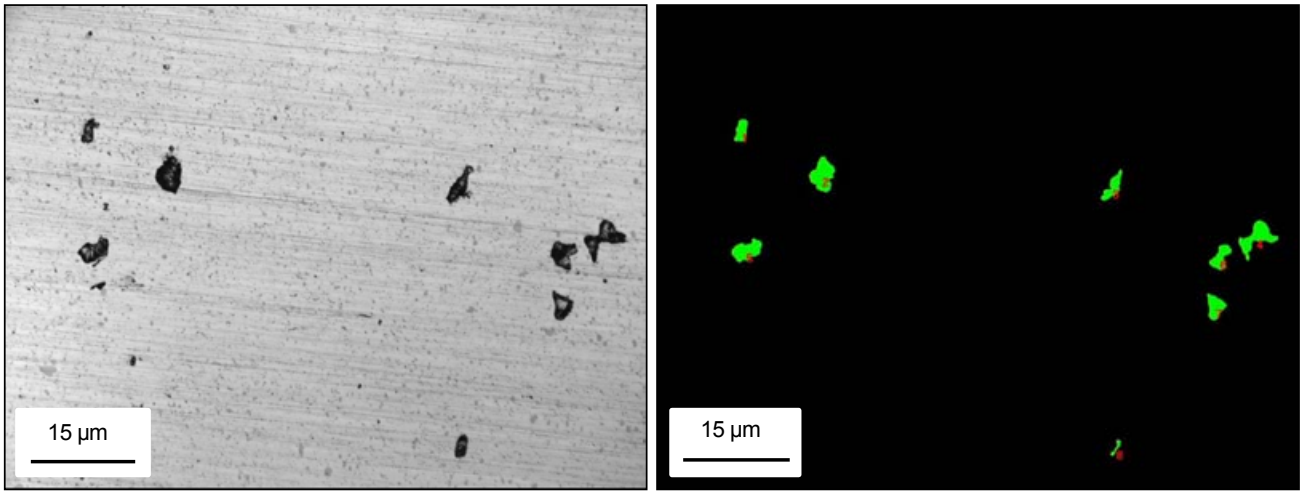

Figure 4.36 A and B. A) Showing a group of pits on the surface of a specimen, sensitised for 10 hours at 150^oC, alternately immersed in pH3 NaCl for 336 hours. B) A binary representation of the pits that were measured by CLSM.

Figures 4.37 documents the pit morphology of a specimen heat treated at 150^0C for 25 hrs after 336 hrs alternate immersion in pH3 3.5% NaCl. There is a large difference between the pit morphology of this heat treatment when compared to the as-received and 10 hour heat treatment at 150^0C. The pit size is much greater, the largest being 102μm^2 in area with the average size approximately 20μm^2. The average pit density and pit depth also increase by a significant amount (see table 4.3). This suggests that pitting is more severe for the longer heat treatment in contrast to the as-received and shorter heat treatment.

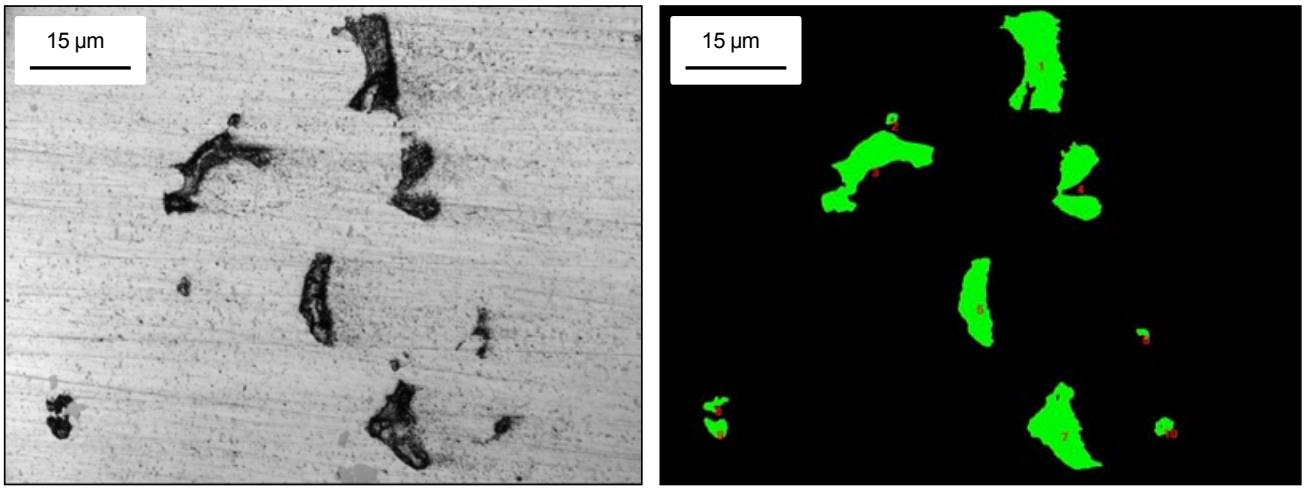

Figure 4.37 A and B. A) Showing a group of pits on the surface of a sensitised specimen (25 hours at 150^oC) alternately immersed in pH3 NaCl for 336 hours. B) A binary representation of the pits that were measured by CLSM.

Figure 4.38 shows the same area as that presented in figure 4.37, however it has been etched for 30 seconds in Keller's reagent to reveal the microstructure. It can be seen that some of the pit boundaries follow the grain boundaries suggesting inter-granular corrosion (IGC) combined with pitting. However, the distribution of pits is still mostly random (like the two previous aging conditions).

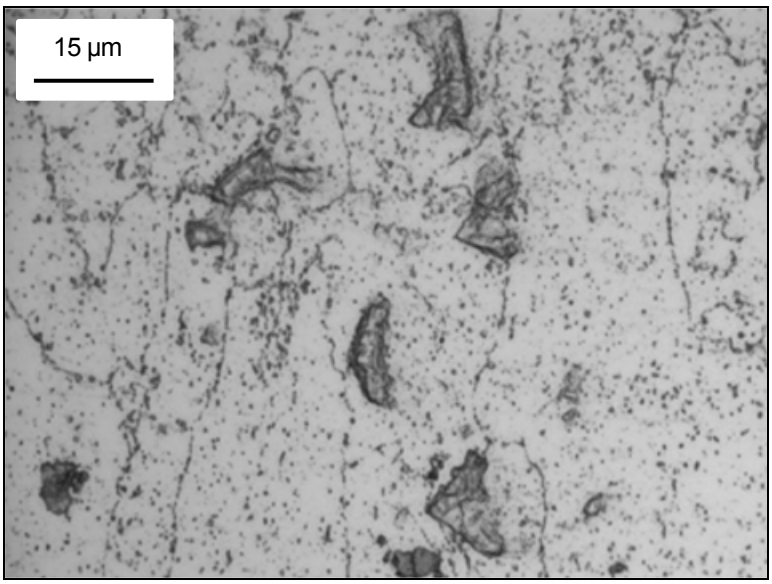

Figure 4.38. Represents that same surface area as presented in figure 4.37 after Keller's etching to reveal the microstructure

Figure 4.39 is a 3D wire representation of the same area. The colour scale indicates that the depth of the pit is roughly around 7µm, which is greater than the average pit depth of the 25hrs at 150°C heat treatment (see table 4.3).

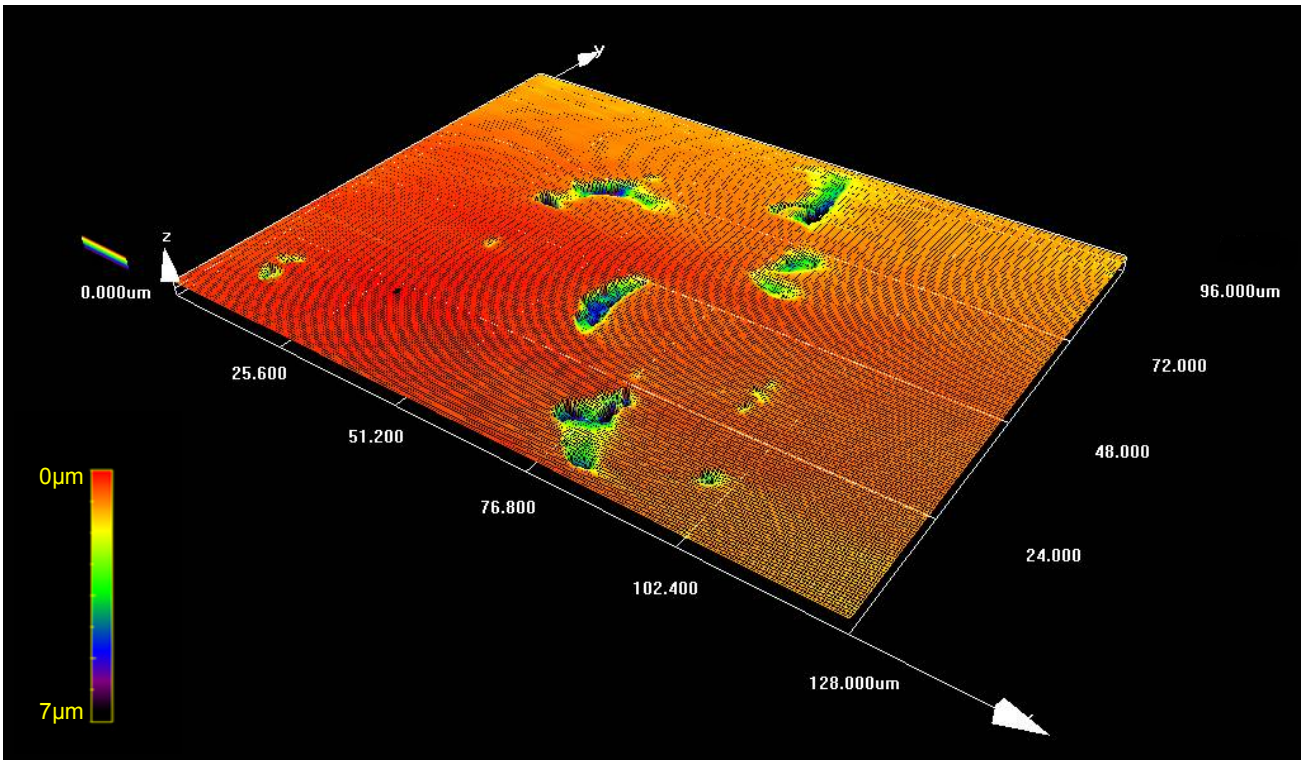

Figure 4.39. A 3D wire representation of the same area documented in figure 4.37 taken using CLSM.

Figures 4.40 documents the pit morphology of a specimen heat treated at 150^{0}C for 50 hrs after 336 hrs alternate immersion in pH3 3.5% NaCl. There is a degree of similarity when compared to the 100hrs at 150^{o}C. The pit size is much greater than that of the as-received, 10hrs and 25hrs at 150^{0}C conditions; it appears that various smaller pits have grown and joined together to form a pit that covers the majority of the surface area. The area rate was calculated to be 8.35%, the maximum of all the other heat treatments that underwent full immersion in pH3 3.5% NaCl. The average pit density and pit depth are also the largest (see table 4.3). This clearly demonstrates that pitting is the most severe for the longest heat treatment. Samples held at 150^{0}C for 50hrs are seriously compromised when immersed in acidic chloride environments.

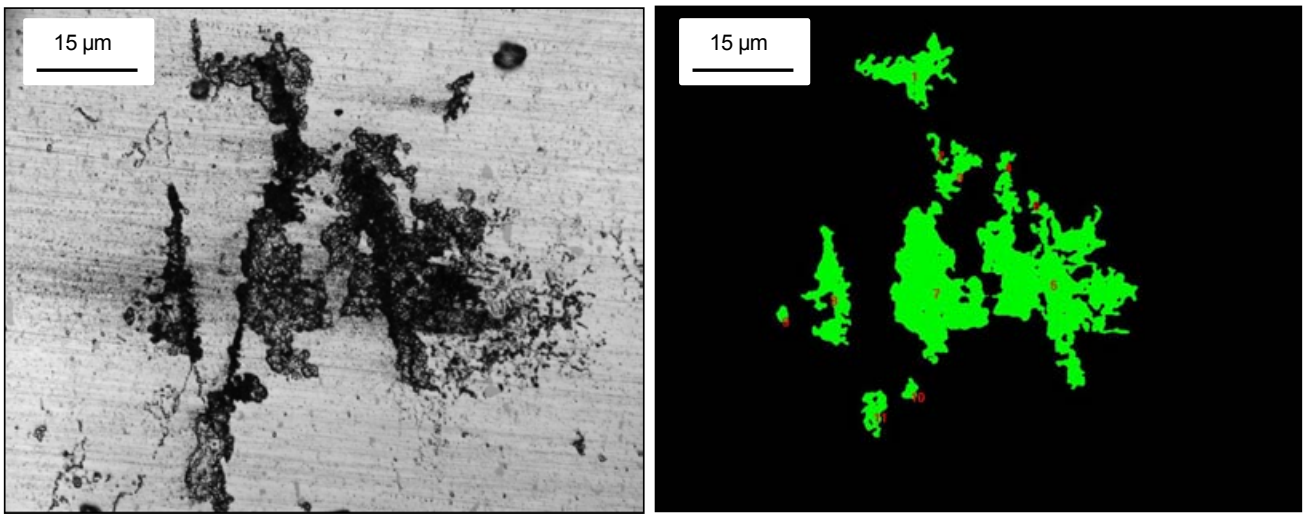

Figure 4.40 A and B. A) Showing a group of pits on the surface of a sample heated for 50 hours at 150^{o}C specimen alternately immersed in pH3 NaCl for 336 hours. B) A binary representation of the pits that were measured by CLSM.

Figure 4.41 represents an etched microstructure of the same area represented in figure 4.40. It is clear that the pits have grown along grain boundaries to join up with other adjacent pits, suggesting pitting and IGC. The red lines indicate grain boundaries along which IGC and pitting has occurred. It could also be suggested that whole grains have been corroded away, due to the severe nature of pitting that occurs on samples of this heat treatment.

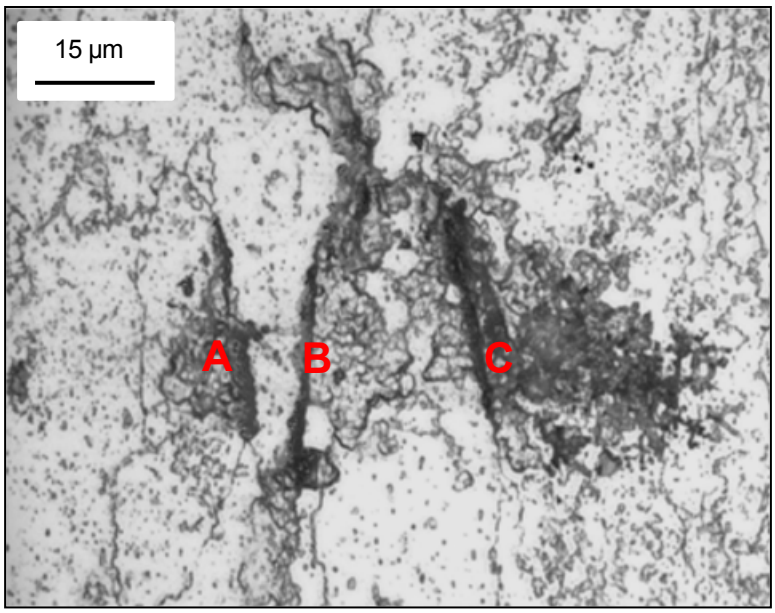

Figure 4.41 represents that same surface area as presented in figure 4.40 after Keller's etching to reveal the microstructure.

A profile of an adjacent cross section of the specimen is shown in Figure 4.42. To produce this cross section, a vertical section was made through the pit above and optical micrographic pictures were taken. It is evident that the pits shown in figure 4.43 have coalesced. According to ASTM standard G 46-94 [70] (Standard Practice for Examination and Evaluation of Pitting Corrosion) the three separate pits (indicated as A, B and C in figures 4.42 and 4.43) have joined beneath the surface of the material via horizontal pit growth. Pit A, B and C also shows signs of undercutting the surface. It may be that the surface material apparent between pits A and B in figure 4.42 has been ground away when removing material to reveal the pit. It is possible that there was growth beneath this layer of material, thus connecting A and B much in the same way that B and C are connected. It is interesting to note that all three pits are roughly the same depth and all exhibit similar growth conditions.

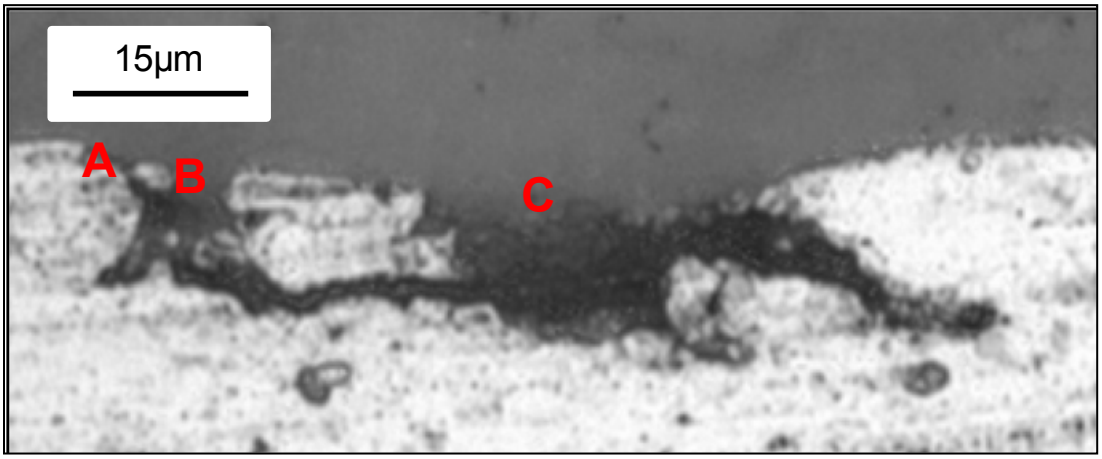

Figure 4.43 Cross section of the same area represented in figure 4.41.

Figure 4.44 is a 3D wire representation of the same area. The colour scale indicates that the depth of the pit is roughly around 15µm. Which is greater than the average pit depth (8.1µm) for samples sensitised for 50hrs at 150^{0}Cµm (see table 4.3). The areas of deep attack represent where discrete pits have nucleated first, yet, with increasing exposure time pit, coalescence took place to cause more extensive, larger areas of local attack.

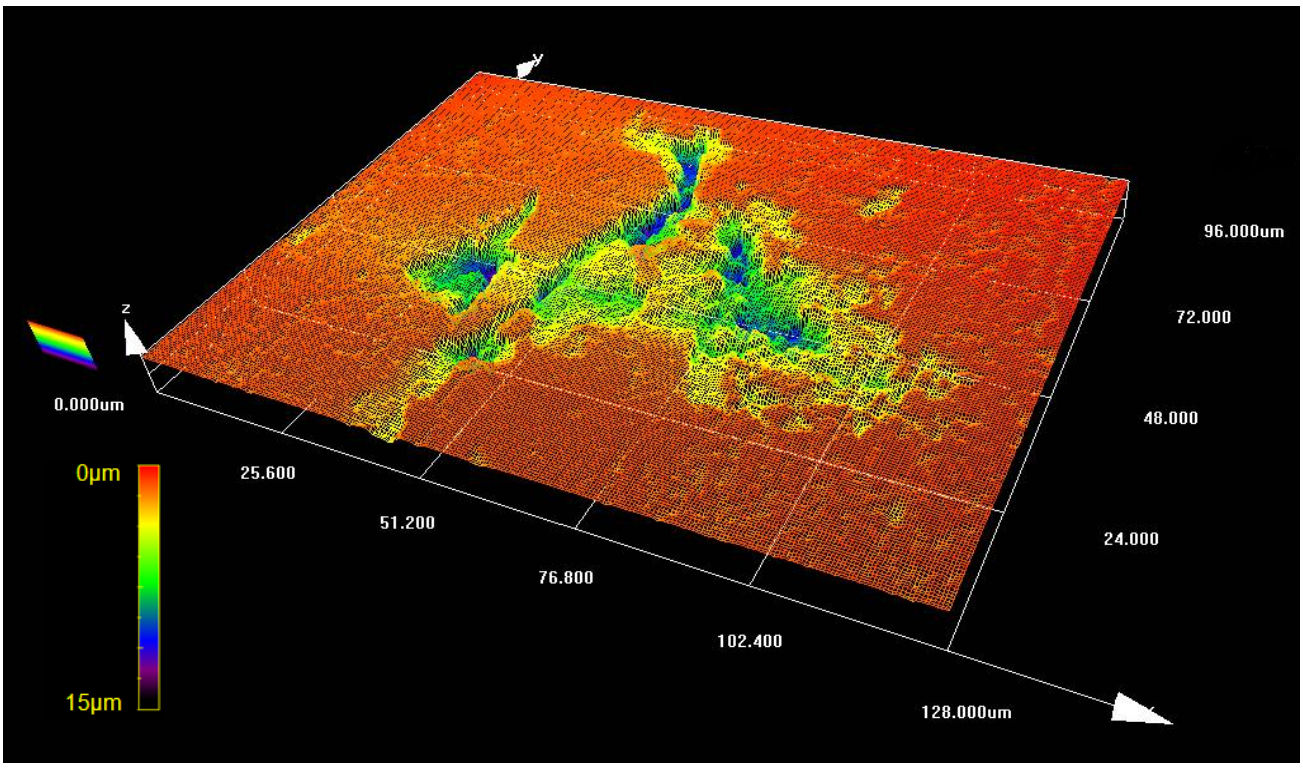

Figure 4.44. A 3D wire representation of the same are documented in figure 4.41 taken using CLSM.

Figure 4.45 documents the pit morphology of a specimen heat treated at 150^{0}C for 100 hours after 336 hrs alternate immersion in pH3 3.5% NaCl. It is obvious from the figure that the corrosion susceptibility of the sample is significantly less than the all of the previous samples. This is clear from size of the pits present at the surface. They are considerably greater than that of the as-received, 10hrs and 25hrs at 150^{0}C conditions (see table 4.4). Similarly to the sample heated at 150^{o}C for 50 hours, various smaller pits have grown and joined together to form a pit that covers the majority of the surface area. The area rate was calculated to be 11.3%, the maximum of all the other heat treatments that underwent full immersion in pH3 3.5% NaCl. The average pit density and pit depth are also the largest (see table 4.3). This clearly demonstrates that pitting is the most severe for longer sensitisation times (in excess of 50 hours).

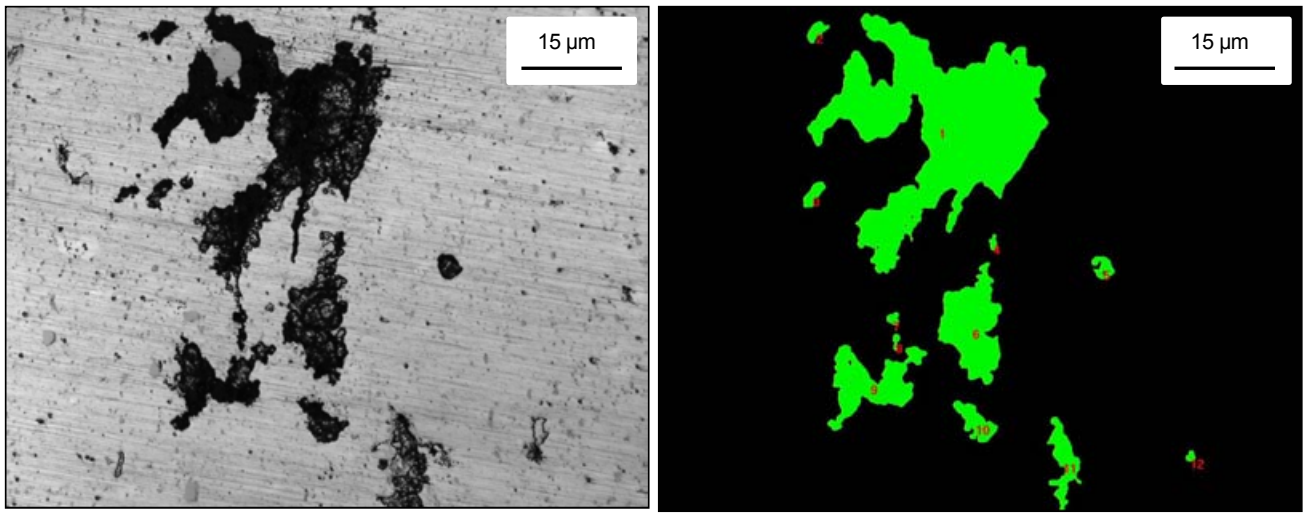

Figure 4.45 A and B. A) Showing a group of pits on the surface of a sample heated for 100 hours at 150°C specimen alternately immersed in pH3 NaCl for 336 hours. B) A binary representation of the pits that were measured by CLSM.

Figure 4.46 represents an etched microstructure of the same area represented in figure 4.45. Similar to the microstructure of the 100hrs at 150^{0}C specimen it is apparent that the pits have propagated along grain boundaries to join up with other adjacent pits, suggesting mechanisms of both pitting and IGC. It is clear from average pit depth and density that the pitting is more severe than any previous sample. The pitting and IGC are also enhanced due to the aggressive nature of alternate immersion. Again it appears that whole grains have been corroded away, due to the severe nature of pitting that occurs on samples of this heat treatment.

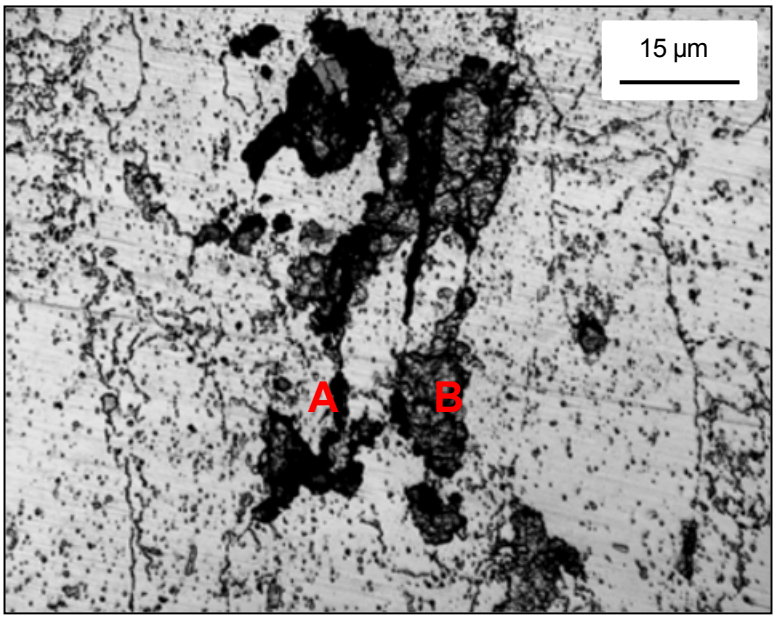

Figure 4.46 Represents that same surface area as presented in figure 4.45 after Keller's etching to reveal the microstructure.

A profile of an adjacent cross section of the specimen is shown in Figure 4.47. To produce this cross section, a vertical section was made through the pit above and optical micrographic pictures were taken. It is evident that the pits shown in this figure have coalesced. According to ASTM standard G 46-94 [70] (Standard Practice for Examination and Evaluation of Pitting Corrosion) the two separate pits (indicated as A and B in both figures 4.46 and 4.47) have joined beneath the surface of the material through horizontal pit growth. Pit growth has quite clearly undercut the surface, and extends horizontally outward by almost 80μm this is possibly due to the aggressive nature of alternate immersion and the autocatalytic nature of pits.

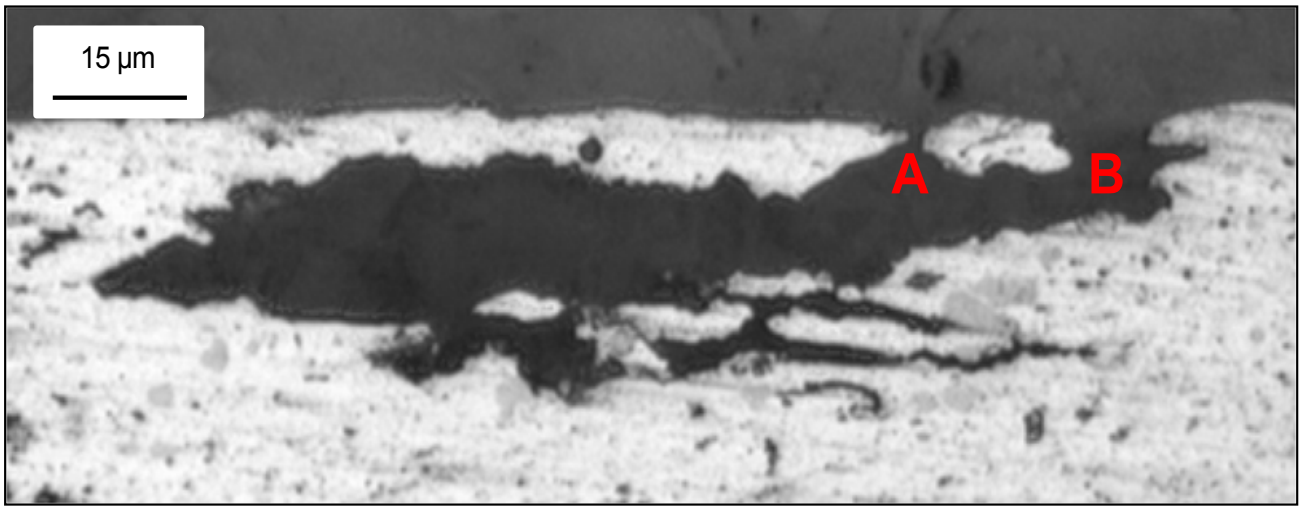

Figure 4.47 A cross section of the same area represented in figure 4.29

Figure 4.48 is a 3D wire representation of the same area. The colour scale indicates that the depth of the pit is roughly around 15μm. Which is greater than the average pit depth (8.2μm) of the samples sensitised for 100hrs at 150^{0}C (see table 4.3). There are large areas of deep attack whereby discrete pits have nucleated first. There is also an extended area of localised attack. In comparison to the samples sensitised for 50 hours at the same temperature the amount of localised attack appears less, however, individual pits appear deeper.

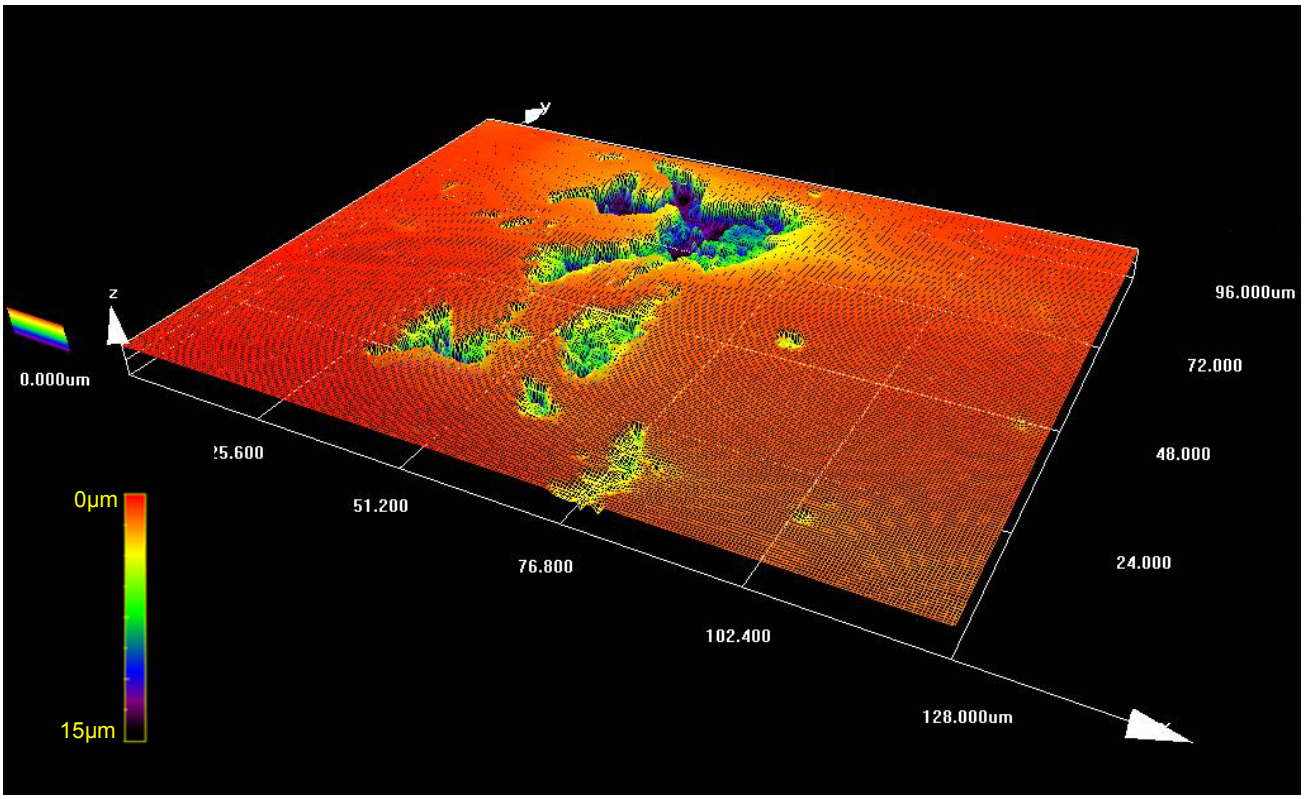

Figure 4.48. A 3D wire representation of the same are documented in figure 4.46 taken using CLSM.

4.4.1.3 Discussion

Intermetallic constituent particles can be seen in various figures (represented by grey shiny areas, see example figure 4.31). The presence of such particles has already been discussed in the literature (see section 2.5.1). The equilibrium solubility of many metals in aluminium is very low; therefore alloying additions as well as impurities often form intermetallic particles. These particles have semi conductive oxide films and are more effective sites for the cathodic reactions. Reviewing table 2.1 it is possible that such cathodic intermetallics could be Al_2Fe or Al_2Cu [37].

Secondly, there is a relationship between sensitisation time, pitting depth and density and immersion type. The increase in sensitisation time at 150^0C results in an increase in the severity of pitting. The results shown in the Table 4.4 confirm this relationship between increased sensitisation time and the increase in the total area of pitting, average pit volume and the area ratio (see equation 3.2). As documented previously in section 4.2 there is also a marked increase gained by the type of immersion. Alternate immersion results in increased IGC beneath the surface, this is because a more aggressive environment is created within the pit due to ease of which oxygen is accessed. It is clear from the

CLSM and the fatigue work conducted, that larger pits present on the typical surface of sensitised AA5456-H116 are, more than likely, the cause of crack initiation and ultimately failure. The aggressive nature of the alternate immersion environment also causes greater pit attack resulting in deeper, larger pits. At the higher sensitisation times of 50 to 100 hours the pitting appears to grow and connect through intergranular corrosion mechanism both upon and beneath the surface. Again much like that which was discussed in section 4.2.5.3, this can be attributed to an increase in anodically active β phase precipitates nucleating preferentially along grain boundaries after longer sensitisation times. It can be reasonably assumed that despite the presence of areas where pitting is not as severe, there is a greater number and greater size of precipitates nucleating after longer sensitisation times, thus leading to greater pit sizes in certain areas. Searles and Bucheit[21] confirmed for 5083 that there was a greater number of β-phase particles present at grain boundaries after longer sensitisation time through the use of TEM. They also confirmed that coarse discontinuous grain boundary precipitates were observed micrometers apart, which could account for the intermittent areas of the large pits.

However, this does not explain the existence of inter-granular corrosion (IGC) that links pits. It is already known that β-phase particles are highly reactive and would be expected to dissolve rapidly if exposed to a chloride containing solutions. Winsley [68] was the first to propose that discrete precipitates can cause continuous IGC attack; the same theory can be used to explain IGC between pits. When an exposed grain boundary precipitate dissolves, it frees Mg^{2+} ions into the localised solution cavity. This change in the localised solution makes that solution inherently more aggressive to the surrounding aluminium matrix, this could serve to preferentially attack the surrounding matrix. As the area of attack widens it may, in highly sensitised conditions, reach another coarse grain boundary β-phase particle, which again dissolves rapidly producing a more aggressive localised solution. Thus it is possible for IGC to link pits as they produce the aggressive localised solution that enables attack of the surrounding matrix.

5. Summary and Conclusions

After investigating the effect of sensitisation on the corrosion fatigue properties of AA5456-H116 a number of conclusions can be drawn.

Ultimately sensitisation is associated with precipitation of β-phase at grain boundaries. The degree of precipitation and extent of corrosion shows a consistent trend depending on the sensitisation time. From anodic potentiodynamic sweeps it is clear that the microstructure of AA5456 becomes more anodically active with increasing sensitisation time. It is also apparent that there is a 'critical' aging time whereby, AA5456 becomes highly sensitised at 150^0C in excess of 25 hours. Above the 'critical' aging time the material is highly susceptible to IGC and localised corrosion, this can maybe attributed to a greater presence of anodically reactive β-phase precipitates at grain boundaries. In order to confirm this TEM evaluation would be necessary.

The resulting microstructure of sensitised AA5456 can lead to large scale localised attack in the form of inter-granular corrosion and pitting. The severity (i.e. depth and density) of this attack is determined by the length of sensitisation, with the longer treatment times of 50 and 100 hours resulting in a greater the extent of corrosion and immersion type.

The marked effect sensitisation has on the corrosion properties of AA5456 has serious implications on the fatigue lifetime. The sensitisation times that result in large amounts of pitting on the surface of the material lead to a reduction in the fatigue lifetime. A determining factor that dictates failure is the immersion environment, whereby, the aggressive nature of the alternate environment produces lower fatigue lifetimes, fractographic examination of fracture surfaces indicates that in all cases cracks have initiated from pits present at the surface. The depth of the initiating pits increases with increasing sensitisation time. It is evident that the larger pits (i.e. greater depth, volume and surface area) present on the surface of the sensitised specimens have acted as the initiation sites for failure.

The morphology of these large pits revealed that pit growth and inter-granular corrosion extends both on and beneath the surface. The localised attack caused by immersion explains the mechanisms for failure below which can be accepted as normal fatigue lifetime of AA5456-H116. When comparing immersion conditions it is clear that alternate immersion produces greater IGC due to the more

aggressive nature of the solution. This results in a reduction in fatigue lifetime when compared to full immersion.

In summary sensitisation results in β-phase precipitation at grain boundaries that causes microstructure to become susceptible to localised corrosion, the extent of which is governed by the length of sensitisation at 150^0C. Longer sensitisation times should result in greater grain boundary β-phase precipitation resulting in a more susceptible microstructure. When immersed in chloride containing environments localised corrosion, in the form of pitting and IGC, occurs. The extent of which is determined by the sensitisation time. Ultimately increased sensitisation time at 150^oC has been shown to render the microstructure of AA5456-H116 susceptible to IGC and localised corrosion (in the form of pitting), which in turn modifies the local stress and ultimately shortens the fatigue life and lowers the threshold stress for crack initiation and propagation.

6. Appendix

Appendix A.1 Literature Review

A.1.1 Stress Corrosion Cracking of Aluminium Alloys

Stress-corrosion cracking (SCC) is a term used to describe service failures in engineering materials that occur by slow, environmentally-induced crack propagation resulting from the combined effects of an active environment and a mechanical stress, neither of which occurring individually would be expected to cause such failure. The magnitude of stresses involved for crack initiation and propagation can be far below the values expected to cause yielding. SCC can be thought of as a delayed failure process, meaning that cracks initiate and propagate at very slow rates (around 10^{-9}-10^{-6} $m.s^{-1}$) until stresses in the remaining ligaments of metal exceed the material's fracture strength[42].

Generally it is agreed that for SCC to occur, three conditions are required: first the alloy must be susceptible; second, there must be a specific damaging environment (e.g. salt water); and third, the stress intensity must be sufficient[43]. However, not all aluminium alloys are vulnerable to SCC; for example, AA6061-T6 and AA3004 are often considered as immune. Furthermore, SCC susceptibility is affected by grain orientation within a specimen. During SCC, fine cracks could cause the component to be close to failure, while outwardly it appears largely corrosion free; for this reason SCC is highly dangerous in service.

A1.2 Mechanisms of SCC

There are a number of theories as to why SCC occurs and within these many theories there are numerous sub-models. This work will now consider the two main proposed mechanisms; anodic dissolution induced cleavage and hydrogen embrittlement.

The anodic dissolution mechanism is based on the idea that crack propagation is associated with localised anodic dissolution. Initiation is believed to occur as a result of sufficient concentration of stress

at the base of a localised corrosion pit; the deeper the attack and the smaller the radius at the base of the pit the greater the stress concentration. At the resulting crack tip, the metal surface has no film or oxide protecting it, thus the bare metal is exposed to a damaging corrosive environment. Because this unprotected metal is more reactive than the surrounding matrix, an increase in current flow from the crack tip takes place, and hence there is accelerated anodic dissolution until the protective oxide is reformed. Continued corrosion results in further separation of the metal, which results in an increased rate of crack penetration, due to the mutually detrimental effects of tensile stress and corrosion. In aluminium alloys, susceptible localised paths of attack are generally associated with grain boundaries. In 2xxx series alloys, the susceptible path is a copper deleted region either side of the grain boundaries, which is created through the precipitation of copper-rich particles at the grain boundaries. In the 5xxx series alloys, it is the preferential grain boundary decoration of the anodically reactive precipitate Mg_2Al_3 that forms the susceptible path of attack. The anodic dissolution mechanism has gained much support within the literature, especially to explain SCC within the 5xxx[5, 19, 21] series of aluminium alloys.

The hydrogen embrittlement mechanism suggests that cracks propagate following atomic hydrogen absorption into the metal, this causes weakening or embrittlement of the metallic bonds at the crack tip, just beneath the surface. Although many possible mechanisms by which this can occur have been reported the process of hydrogen embrittlement basically consists of aggressive species being adsorbed at the crack tip causing a reduction in the metal-metal bond strength. Separation then occurs by the adsorption of hydrogen in locally dilated areas immediately ahead of the crack tip. Hydrogen gas then forms in locally dilated areas or along slip planes, this gas pressure assists in rupture of metal-metal bonds. The formation of metal hydrides causes a reduction in metal-metal bond strength and embrittlement of the region ahead of the crack tip. Finally adsorbed hydrogen weakens the grain boundaries causing cleavage that causes intergranular separation or a highly localised plastic fracture. Hydrogen induced cracking appears to be an important contributing mechanism causing SCC of the 5xxx series[44-46].

In summary, no individual mechanism within the literature can be used to accurately explain SCC within all aluminium alloy systems. It seems likely that the true mechanism or mechanisms operating depend greatly on the alloy system in question. However, dissolution almost always plays a major role in the process of SCC. The anodic dissolution mechanism has gained much support within the literature, especially to explain SCC within the 5xxx [5, 19, 21] series of aluminium alloys

A.1.3 Stress Corrosion Cracking Susceptibility of Al-Alloys

Stress corrosion cracking (SCC) problems have been observed in service for Al-Cu, Al-Zn-Mg-Cu, Al-Zn-Mg and Al-Mg alloy systems. Test methods utilising both constant-load and constant-strain techniques, and both pre-cracked and smooth specimens, have established standards that allow many alloys to be used safely. SCC experiments can be classified into three different categories: tests on statically loaded smooth samples; tests on statically loaded precracked samples, and tests using dynamically strained samples. Detailed information on SCC tests can be found in reference [47]. Of these tests, the slow strain rate tension (SSRT) method is described below in greater detail.

The slow strain rate tension (SSRT) method offers the potential of a rapid, reliable, reproduced assessment of stress corrosion susceptibility. The application of SSRT testing on 2xxx, 5xxx and 7xxx Al-based alloys has been reviewed by Holroyd and Scamans [48]. They claimed that the slow strain rate stress corrosion test could provide results consistent with service experience and other test methods for both laboratory alloys and commercial alloys in various product forms. A strain rate of 10^{-4} s^{-1} was generally appropriate for 5xxx series alloys and 10^{-6} s^{-1} for 2xxx and 7xxx series alloys (Figure 2.16). In each series of alloys, the “ductility ratio” shown in Figure 2.16 refers to a ductility parameter such as reduction in area, elongation, or fracture energy determined in the corrosive test solution normalised to that obtained at the same strain rate in an inert test environment.

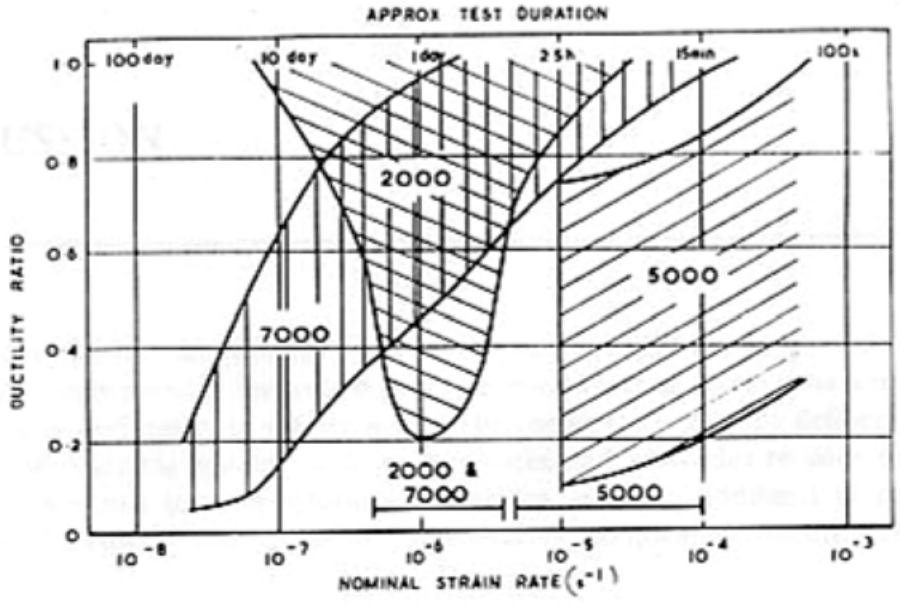

Figure: A.1.1 Strain rate regimes for studying stress corrosion cracking of 2xxx, 5xxx and 7xxx alloys[48].

The magnitude of the strain rate is the critical factor in SSRT testing. For example, if the strain rate is too high, ductile fracture will occur before the necessary corrosion reactions can take place. On the other hand, if the strain rate is too low, repassivation becomes possible and corrosion is prevented, thus the necessary reactions between exposed metal and the environment cannot be take place preventing SCC. Typical critical strain rates range from 10^{-5} s^{-1} to 10^{-7} s^{-1}, but will change depending on the alloy and environment system. Solutions containing chloride ions was found to be the most effective environment for laboratory tests, because the test results potentially relate to stress corrosion behaviour in natural environments.

Appendix A.2 Relevant 5xxx Series NAMLT Results

Material Identification	Heat Treatment	NAMLT Value (mg/cm^2)	Standard Deviation (mg/cm^2)
SHT (30mins @ 450°C, air-cooled) AA5182 Yuan, 2006 REF	10 hrs – 70°C	1.23	0.01
	10 hrs – 85°C	1.5	0.05
	10hrs – 100°C	6.6	0.5
	10 hrs - 150°C	39.8	1.5
	50 hrs – 150°C	47.4	1.3
	100 hrs – 150°C	48.7	1.4
SHT (2hrs @ 520°C, quenched) AA5083 H116 Winsley, 2006 re	10hrs – 100°C	10	0.78
	10 hrs – 150°C	30	1.3
	100 hrs – 150°C	38	0.3
AA5083 H116 Winsley, 2006 REF	As-Received	-	-
	100 hrs - 150°C	28	2.2

Appendix A.3 University of Birmingham PhD Thesis: Evaluation of the corrosion resistance of FSW AA5083-H116, Winsley, 2006.

This section is taken directly from work done by R. Winsley [68]. The following chapter presents the glow discharge optical emission spectroscopy (GDOES) results for AA5083-H116 which has a similar magnesium content as the AA5456-H116 investigated in this work.

A.3.1 'As received' AA5083-H116

Commercial AA5083-H116 was used in this work, supplied by Novelis, Kingston in a plate thickness of 5 mm. The composition of the alloy, determined by optical emission spectroscopy is given in Table A3.1.1.

Table A3.1.1: Chemical composition of AA5083-H116, (wt. %) was determined by optical emission spectroscopy (OES).

Mg	Cu	Mn	Fe	Cr	Si	Zn	Ti	Ni
4.22 ± 0.21	0.033 ± 0.002	0.57 ± 0.03	0.26 ± 0.01	0.091 ± 0.006	0.078 ± 0.004	0.009 ± 0.002	0.007 ± 0.001	0.005 ± 0.001

A.3.2 Glow Discharge Optical Emissions Spectroscopy (GDOES)

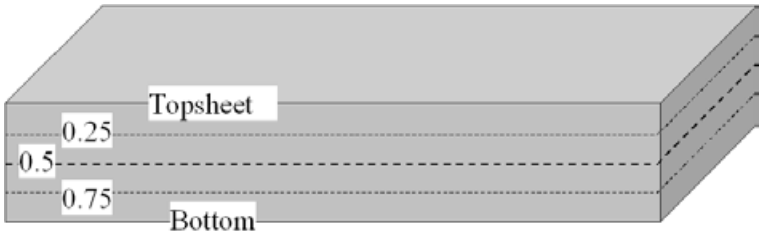

Figure A3.2.1: Schematic representing the depths through the 5mm thickness of AA5083-H116 analysed for compositional variance data.

At each of the 5 depths through the 5mm thickness of AA5083-H116 plate, GDOES elemental analysis was performed. Craters of ~60 µm were sputtered at each depth and the raw data (intensity) are shown in Figure A3.2.1 for elemental levels of Cu, Fe, Mn, Mg, Si and Zn.

A clear reduction in the signal for Mg was observed at the centre of the plate (Figure 4.7 c) compared to the full thickness samples (Figure 3.2.2 a and e) and the 25 and 75 % samples (Figure 4.7 b and d). A slight, but reproducible decrease in Mg intensity was also observed between the full thickness samples (top and bottom) and the 25 and 75% removed samples. This GDOES data is in good agreement with the electron micro-probe elemental line-scan results shown in Figure 4.5. In order to convert these observed differences in through thickness Mg intensity levels into wt. % data, an Mg GDOES calibration curve was utilised, as shown in Figure A3.2.2.

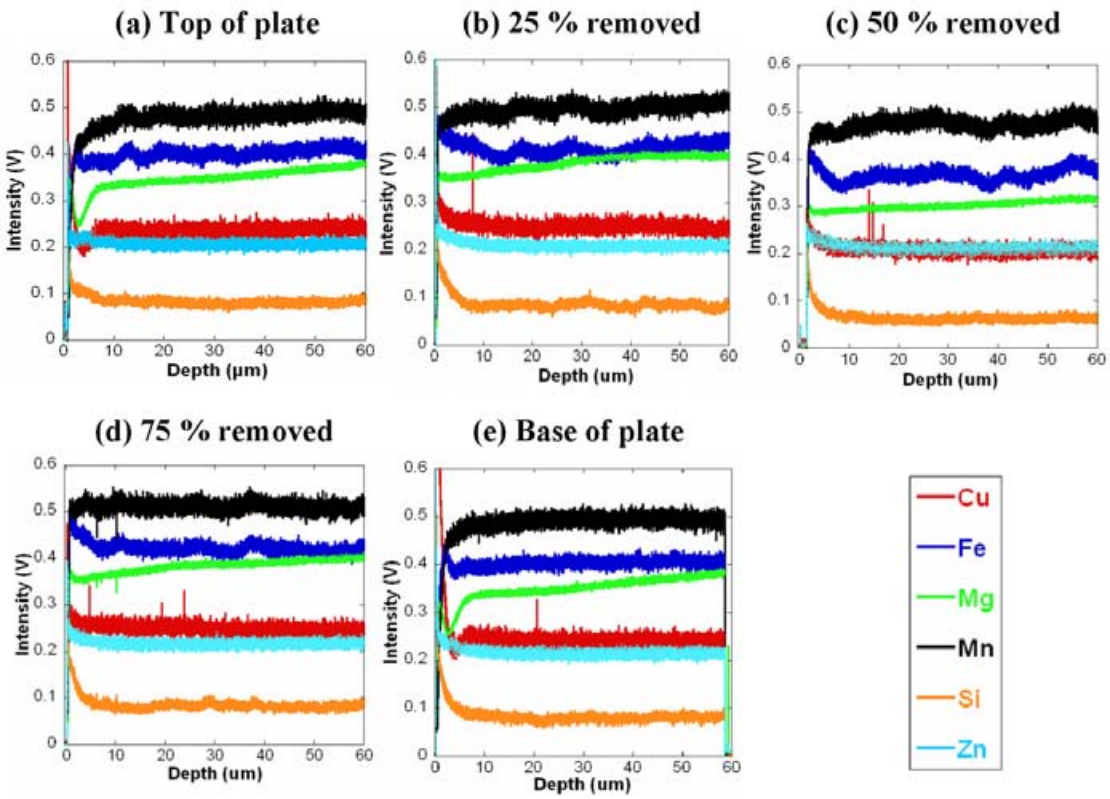

Figure A3.2.2: GDOES compositional data as intensity (V), taken at various depths through the thickness of 5mm AA5083-H116 plate; **(a)** Top sheet of plate **(b)** 25 % of plate thickness removed **(c)** 50 % of plate thickness removed **(d)** 75 % of plate thickness removed **(e)** bottom of plate (Depths illustrated schematically in Figure 4.6).

Figure A3.2.3 clearly shows that the Mg concentration at the centre of the plate is lower by some 1.2 wt. % compared with the levels at 25 and 75 % removed thickness and by over 0.6 wt.% compared with the top and bottom of the 5 mm plate. Figure A3.2.4 supports this observation; it shows the GDOES wt. % data combined with EDS full screen (large area) and matrix spot data taken from analysis of the base of each GDOES crater. The same Mg compositional trend is clearly evident from both the short count time matrix spot analysis and the longer general area EDS analysis at the various depths through AA5083-H116 plate.

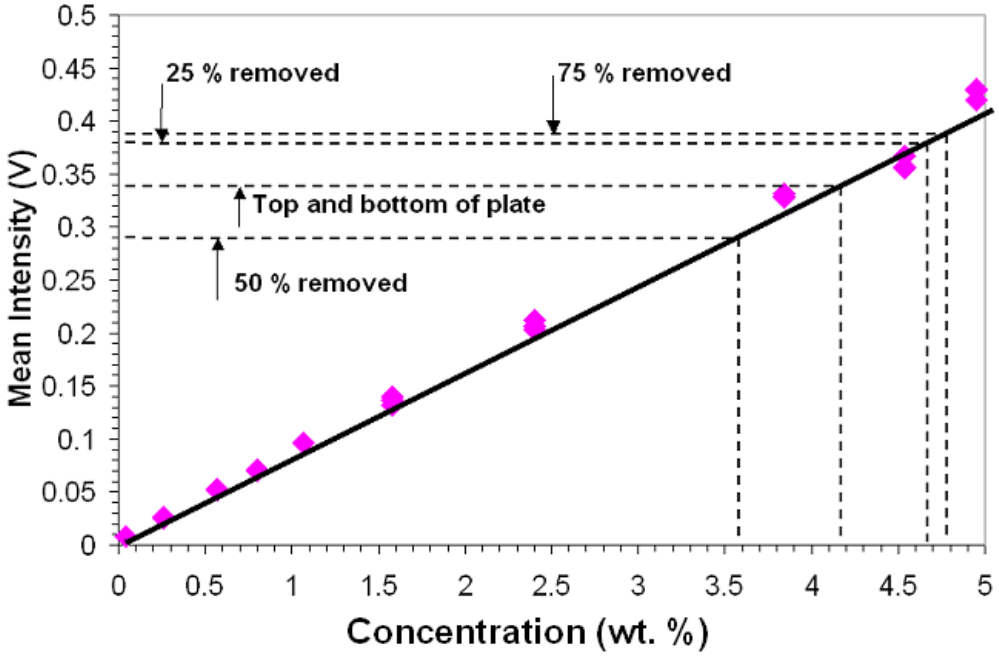

Figure A3.2.3: Elemental calibration curve for Mg, used to convert mean GDOES intensity (V) values into wt. % data.

Figure A3.2.4 (b) is taken from Figure A3.2.4 (a); it shows the through thickness variation in closer detail for the other alloying elements in AA5083-H116 plate. It can be seen that levels of Mn, and Zn appear constant through the plate thickness, whereas levels of Fe and Cu measured using GDOES appear to be reduced at the plate centre. Impurity levels of Cr, measured using full screen EDS analysis appear to increase slightly at the plate centre.

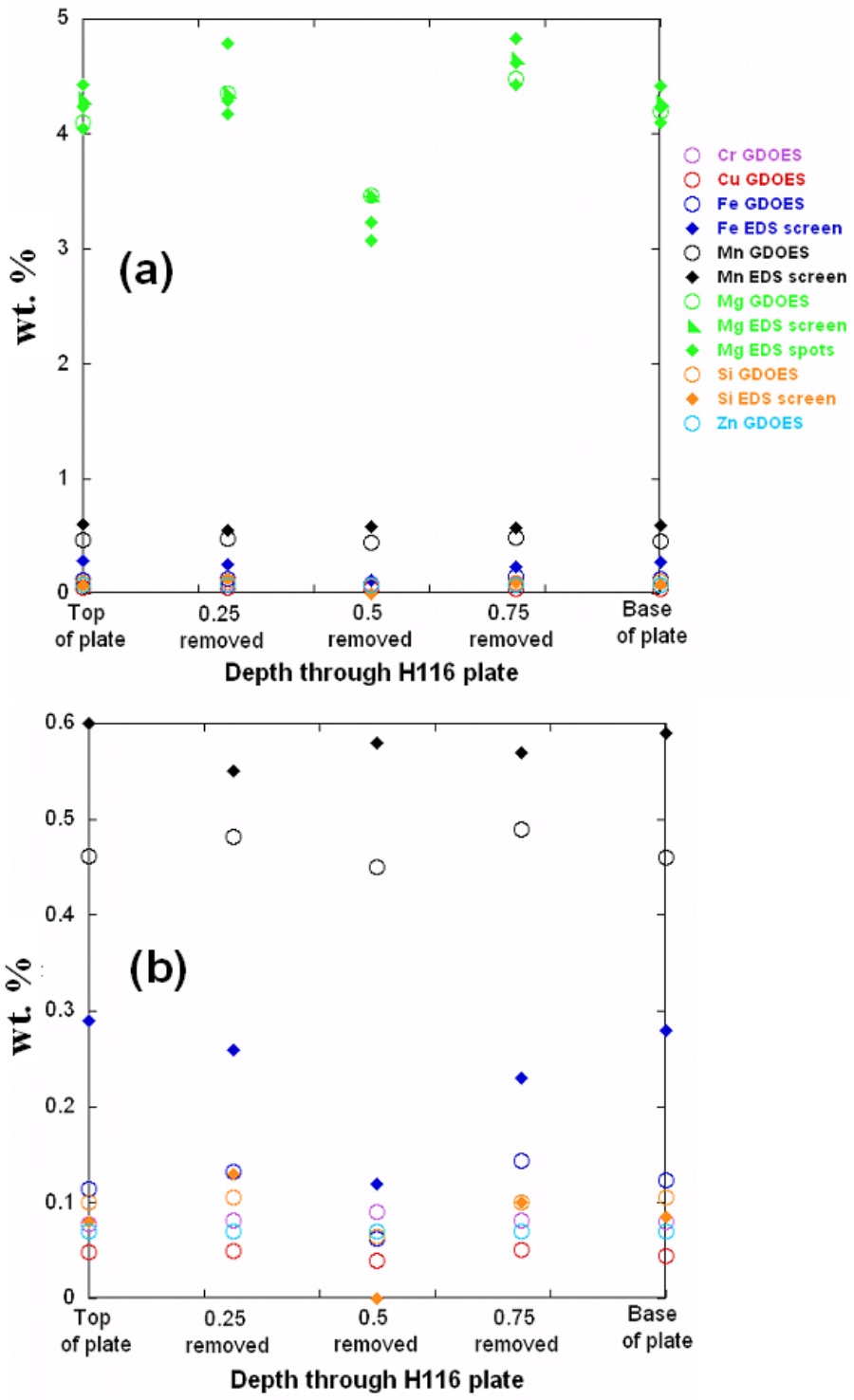

Figure A3.2.4: Compositional variation through the thickness of AA5083-H116 plate, elemental composition shown as wt. %, values are shown from GDOES data taken from calibration curves (example for Mg shown in Figure 4.8), EDS full screen analysis (long count time) and EDS spot analysis (short count time), taken from the bottom of the GDOES crater **(a)** Primarily showing Mg variation **(b)** Expanded axis showing trace elements.

Appendix A.4 Table of Confocal Laser Scanning Microscopy Results

Presented below are all the results gathered from the confocal laser scanning microscopy (CLSM) work. Three randomly selected areas SIZE on the top plate of each heat treatment condition and immersion type was examined. (For experimental details of both the immersion conditions and CLSM see section 3.6 and 3.7 respectively). As already seen throughout the thesis, there is an increase in the depth, volume and surface area of pitting as a function of sensitisation time. However, it must be pointed out that not all areas on the surface contained the large pits that where fully examined in section 4.5. The table below accurately documents the measured results and the calculated averages provide a fair representation of the typical pitting present on each sample.

The same conclusions that an increase in the extent of pitting with increasing sensitisation time can still be drawn from these averages. However, it must be stressed that all of the surface was examined firstly via optical microscopy (see section 4.2) and then using the fractography (section 4.4) the larger pits shown in section 4.5 where chosen to provide and accurate representation of the type of pits present on the surface of specimens that lead to crack initiation.

Again it can be seen from the results that there is evidence supporting a critical aging time in excess of 25 hours. The extent of pitting on specimens heated at 150^{o}C below this time show only small pits, in both area and volume, and there is little to no evidence of inter-granular corrosion (IGC). On the other hand the representative surface areas of those samples heated for up to 25 hours and longer contain larger pit networks connected by IGC, with greater volumes and surface areas. However, not all of the documented areas on the longer sensitisation times contained these large pits and it can be concluded that the total surface area is not subjected to aggressive localised corrosion. This could be due to the fact that β-phase particles only precipitate discreetly at gain-boundaries, giving explanation to the varied extent of pitting across the surface area.

Sample Identification	Total number of Pits	Total Area of Pits [µm2]	Average Pit Volume [µm3]	Area ratio[%]
1. As-Received Full Immersion	5	34.909	2.8	0.286

2. As-Received Full Immersion	4	8.175	0.434	0.067
3. As-Received Full Immersion	8	0.668	0.005	0.005
AVERAGE		14.584	1.079	0.119
1. As-Received Alternate Immersion	6	67.89	2.08	0.555
2. As-Received Alternate Immersion	1	11.533	5.948	0.094
3. As-Received Alternate Immersion	2	9.823	0.893	0.08
AVERAGE		29.745	2.974	0.243
1. 10hrs – 150^{o}C Full Immersion	8	68.574	3.698	0.561
2. 10hrs – 150^{o}C Full Immersion	7	16.957	0.789	0.139
3. 10hrs – 150^{o}C Full Immersion	4	23.451	1.089	0.268
AVERAGE		36.327	1.858	0.322

1. 10hrs – 150^{o}C Alternate Immersion	8	101.804	6.175	0.833
2. 10hrs – 150^{o}C Alternate Immersion	7	16.957	0.78	0.139
3. 10hrs – 150^{o}C Alternate Immersion	4	28.723	2.755	0.235
AVERAGE		49.161	3.236	0.402
1. 25hrs – 150^{o}C Full Immersion	15	305.24	8.006	2.497
2. 25hrs – 150^{o}C Full Immersion	2	15.273	4.793	0.133
3. 25hrs – 150^{o}C Full Immersion	7	34.209	5.175	0.28
AVERAGE		118.240	5.991	0.97
1. 25hrs – 150^{o}C Alternate Immersion	10	604.077	36.582	4.942
2. 25hrs – 150^{o}C Alternate Immersion	3	48.306	9.371	0.395

3. 25hrs – 150°C Alternate Immersion	3	37.504	5.145	0.307
AVERAGE		229.962	17.032	1.881
1. 50hrs – 150°C Full Immersion	19	923.196	41.802	7.553
2. 50hrs – 150°C Full Immersion	10	41.747	0.624	0.342
3. 50hrs – 150°C Full Immersion	8	49.923	2.459	0.359
AVERAGE		338.288	33.574	2.751
1. 50hrs – 150°C Alternate Immersion	11	1022.498	96.837	8.365
2. 50hrs – 150°C Alternate Immersion	16	80.868	1.245	0.662
3. 50hrs – 150°C Alternate Immersion	7	59.544	2.641	0.487
AVERAGE		387.636	50.167	3.171
1. 100hrs – 150°C Full Immersion	5	1154.423	115.485	9.445

2. 100hrs – 150°C Full Immersion	21	338.162	32.365	3.49
3. 100hrs – 150°C Full Immersion	14	97.327	2.652	0.796
AVERAGE		529.970667	50.16733333	4.577
1. 100hrs – 150°C Alternate Immersion	12	1388.416	237.302	11.359
2. 100hrs – 150°C Alternate Immersion	23	136.541	2.352	1.117
3. 100hrs – 150°C Alternate Immersion	8	401.059	59.874	7.658
AVERAGE		642.005	99.842	6.71

7. References

1. Sanders, R.E., S.F. Baumann, and H.C. Stumpf, *Aluminium Alloys Their Physical and Mechanical Properties*. 1986, Charlottesville, VA: University of Virginia.
2. Polmear, I.J., *Light Alloys: From Traditional Alloys to Nanocrystals*. 4 ed. 2006: Butterworth-Heinemann.
3. Sanders, R.E., S.F. Baumann, and H.C. Stumpf, *Wrought Non-Heat-Treatable Aluminium Alloys*, in *Aluminium Alloys - Contemporary Research and Applications*, A.K. Vasudevan and R.D. Doherty, Editors. 1989, Academic Press: New York.
4. Schmidt, C.G. and A.K. Miller, *THE EFFECT OF SOLUTES ON THE STRENGTH AND STRAIN-HARDENING BEHAVIOR OF ALLOYS .16.* Acta Metallurgica, 1982. 30(3): p. 615-625.
5. Jones, R.H., et al., *Role of Mg in the stress corrosion cracking of an Al-Mg alloy.* Metallurgical and Materials Transactions a-Physical Metallurgy and Materials Science, 2001. 32(7): p. 1699-1711.
6. Jones, R.H., J.S. Vetrano, and C.F. Windisch, *Stress corrosion cracking of Al-Mg and Mg-Al alloys.* Corrosion, 2004. 60(12): p. 1144-1154.
7. Vetrano, J., et al., *Influence of microstructure and thermal history on the corrosion susceptibility of AA5083*, in *Automotive Alloys 1, TMS Annual Meeting*, S. Das, Editor. 1997, TMS, Warrendale, PA: Orlando, FL. p. 77.
8. Sprowls, D.O. and R.H. Brown, *Fundamental Aspects of Stress Corrosion Cracking.* 1969, Houston: NACE. 466-512.
9. McLean, D., *Grain Boundaries in Metals*. 1957, Oxford: Claredon Press.
10. Westbrook, J.H., *Segregation at Grain Boundaries.* Metallurgy Review, 1964.
11. Scamans, G.M., N.J.H. Holroyd, and C.D.S. Tuck, *THE ROLE OF MAGNESIUM SEGREGATION IN THE INTERGRANULAR STRESS-CORROSION CRACKING OF ALUMINUM-ALLOYS.* Corrosion Science, 1987. 27(4): p. 329-347.
12. Faulkner, R.G., *Segregation to Boundaries and Interfaces in Solids.* Materials Science Forum, 1995. 189-190: p. 81-94.
13. Anthony, T.R., *Solute segregation in vacancy gradients generated by sintering and temperature changes.* Acta Metallurgica, 1969. 17(5): p. 603-609.
14. Cundy, S.L., et al., *STUDIES OF SEGREGATION AND INITIAL STAGES OF PRECIPITATION AT GRAIN BOUNDARIES IN AN ALUMINIUM 7 WT PERCENT MAGNESIUM ALLOY WITH*

AN ENERGY ANALYSING ELECTRON MICROSCOPE. Proceedings of the Royal Society of London Series a-Mathematical and Physical Sciences, 1968. 307(1490): p. 267-&.

15. Doig, P. and J.W. Edington, *INFLUENCE OF SOLUTE DEPLETED ZONES ON STRESS-CORROSION SUSCEPTIBILITY OF AGED AL-7.2 MASS PERCENT MG AND AL-4.4 MASS PERCENT CU ALLOYS.* Proceedings of the Royal Society of London Series a-Mathematical Physical and Engineering Sciences, 1974. 339(1616): p. 37-&.
16. Scamans, G., in *Enviromental Degredation of Engineering Material in Aggresive Enviroments*, M.R. Louthan, R.P. McNitt, and R.D. Sisson, Editors. 1981, Virginia Polytechnic Institute: Blacksburg, VA. p. 153.
17. Vetrano, J.S., D.R. Baer, and R.H. Jones. *Solute segregation and beta-phase precipitation at internal interfaces in AA5083*. in *Symposium on Automotive Alloys II at the 1998 TMS Annual Meeting*. 1998. San Antonio, Tx: Minerals, Metals & Materials Soc.
18. Vetrano, J.S., et al., *Influence of the particle size on recrystallization and grain growth in Al-Mg-X alloys.* Materials Science and Engineering A, 1997. 238(1): p. 101-107.
19. Hollingsworth, E.H. and H.Y. Hunsicker, *Corrosion of Aluminium and Aluminium Alloys*, in *ASM Handbook - Corrosion*, J.R. Davis, Editor. 1992, ASM International. p. 583-609.
20. Carroll, M.C., et al., *Effects of Zn additions on the grain boundary precipitation and corrosion of Al-5083.* Scripta Materialia, 2000. 42(4): p. 335-340.
21. Searles, J.L., P.I. Gouma, and R.G. Buchheit, *Stress corrosion cracking of sensitized AA5083 (Al-4.5Mg-1.0Mn).* Metallurgical and Materials Transactions a-Physical Metallurgy and Materials Science, 2001. 32(11): p. 2859-2867.
22. Oguocha, I.N.A., O.J. Adigun, and S. Yannacopoulos, *Effect of sensitization heat treatment on properties of Al-Mg alloy AA5083-H116.* Journal of Materials Science, 2008. 43(12): p. 4208-4214.
23. Nebti, S., D. Hamana, and G. Cizeron, *Calorimetric Study of Pre-Precipitation and Precipitation of Al-Mg Alloys* Acta Metallurgica Et Materialia, 1995. 43(9): p. 3583-3588.
24. Bournane, M., M. Nedjar, and A.F. Sirenko, *Precipitation in solid solutions of Al-Mg.* Scripta Materialia, 1999. 40(3): p. 375-382.
25. Hamana, D., et al., *Comparative study of formation and transformation of transition phases in Al-12 wt.% Mg alloy.* Journal of Alloys and Compounds, 2001. 320(1): p. 93-102.
26. Rajasekaran, B., et al., *Effect of microarc oxidised layer thickness on plain fatigue and fretting fatigue behaviour of Al-Mg-Si alloy.* International Journal of Fatigue, 2008. 30(7): p. 1259-1266.
27. Starink, M.J. and A.M. Zahra, *beta ' and beta precipitation in an Al-Mg alloy studied by DSC and TEM.* Acta Materialia, 1998. 46(10): p. 3381-3397.

28. Mondolfo, L.F., *Aluminum alloys : structure and properties / L. F. Mondolfo*. 1976, London ; Boston :: Butterworths.
29. Yuan, Y., A.J. Davenport, and M. Strangwood. *Interfacial control of beta-phase precipitation in Al-Mg alloys*. in *International Conference on Solid-Solid Phase Transformations in Inorganic Materials (PTM 2005)*. 2005. Phoenix, AZ: Minerals, Metals & Materials Soc.
30. Lucadamo, G., et al., *Microstructure characterization in cryomilled Al 5083.* Materials Science and Engineering a-Structural Materials Properties Microstructure and Processing, 2006. 430(1-2): p. 230-241.
31. Popovic, M. and E. Romhanji, *Characterization of microstructural changes in an Al-6.8 wt.% Mg alloy by electrical resistivity measurements.* Materials Science and Engineering a-Structural Materials Properties Microstructure and Processing, 2008. 492(1-2): p. 460-467.
32. Kaigorodova, L.I. *The effect of grain-boundary structure formation on beta-precipitation in aged Al-Mg alloys*. in *9th International Conference on Intergranular and Interphase Boundaries in Materials (iib98)*. 1998. Prague, Czech Republic: Transtec Publications Ltd.
33. Frankel, G.S., *Pitting corrosion of metals. A review of the critical factors (vol 145, pg 2186, 1998).* Journal of the Electrochemical Society, 1998. 145(8): p. 2970-2970.
34. Pourbaix, M., *Atlas of Electrochemical Equilibria in Aqueous Solutions*. 1974, NACE: Houston, TX. p. 168.
35. Suter, T., et al., *Microelectrochemical studies of pit initiation on high purity and ultra high purity aluminum.* Advanced Engineering Materials, 2005. 7(5): p. 339-348.
36. Muller, I.L. and J.R. Galvele, *Pitting Potential of High-Purity Binary Aluminum-Alloys .1. Al-Cu Alloys - Pitting and Intergranular Corrosion.* Corrosion Science, 1977. 17(3): p. 179-&.
37. Birbilis, N. and R.G. Buchheit, *Electrochemical characteristics of intermetallic phases in aluminum alloys - An experimental survey and discussion.* Journal of the Electrochemical Society, 2005. 152(4): p. B140-B151.
38. Lumsden, J.B., et al., *Corrosion behavior of friction-stir-welded AA7050-T7651.* Corrosion, 2003. 59(3): p. 212-219.
39. Davis, J., *Aluminum and Aluminum Alloys*. ASM Specialty Handbook. 1993: ASM International. 784.
40. Pao, P.S., et al., *Microstructure, fatigue crack growth, and corrosion in friction stir welded Al 5456.* Friction Stir Welding Processing III, 2005: p. 27-34.
41. Yuan, Y., *Localised Corrosion and Stress Corrosion Cracking of Aluminium-Magnesium Alloys*. Phd Thesis, 2005. University of Birmingham.

42. Jones, R.H. and R.E. Ricker, *Mechanisms of Stress-Corrosion Cracking*, in *Stress-Corrosion Cracking - Materials Performance and Evaluation*, R.H. Jones, Editor. 2003, ASM International. p. 1-40.
43. Burleigh, T.D., *The Postulated Mechanisms for Stress-Corrosion Cracking of Aluminum-Alloys - a Review of the Literature 1980-1989.* Corrosion, 1991. 47(2): p. 89-98.
44. Jones, R.H., *The influence of hydrogen on the stress-corrosion cracking of low-strength Al-Mg alloys.* Jom-Journal of the Minerals Metals & Materials Society, 2003. 55(2): p. 42-46.
45. Tanguy, D., et al., *Hydrogen effects during IGSCC of pure Al-5Mg alloy in NaCl media.* Corrosion Science, 2002. 44(6): p. 1163-1175.
46. Jones, R.H. and M.J. Danielson. *Role of hydrogen in stress corrosion cracking of low-strength Al-Mg alloys*. in *International Conference on Hydrogen Effects on Material Behavior and Corrosion Deformation Interactions*. 2002. Moran, WY.
47. Phull, B.S., *Evaluating Stress Corrosion Cracking*, in *ASM Handbook - Corrosion: Fundamentals , Testing and Protection*. 2003, ASM International. p. 575-616.
48. Holroyd, N.J.H. and G. Scamans, eds. *Environment-Sensitive Fracture: Evaluation and Comparison of Test Methods*. ASTM STP, ed. S.W. Dean, E.N. Pugh, and G.M. Ugiansky. 1984, ASM International.
49. Chang, J.C. and T.H. Chuang, *Stress-corrosion cracking susceptibility of the superplastically formed 5083 aluminum alloy in 3.5 pct NaCl solution.* Metallurgical and Materials Transactions a-Physical Metallurgy and Materials Science, 1999. 30(12): p. 3191-3199.
50. Popovic, M. and E. Romhanji, *Stress corrosion cracking susceptibility of Al-Mg alloy sheet with high Mg content.* Journal of Materials Processing Technology, 2002. 125: p. 275-280.
51. Davenport, A.J., et al. *Intergranular corrosion and stress corrosion cracking of sensitised AA5182*. in *10th International Conference on Aliminium Alloys (ICAA-10)*. 2006. Vancouver, CANADA: Trans Tech Publications Ltd.
52. Baer, D.R., et al., *Influence of Mg on the corrosion of Al.* Journal of Vacuum Science & Technology a-Vacuum Surfaces and Films, 2000. 18(1): p. 131-136.
53. Clausen, A.H., et al., *Flow and fracture characteristics of aluminium alloy AA5083-H116 as function of strain rate, temperature and triaxiality.* Materials Science and Engineering A, 2004. 364(1-2): p. 260-272.
54. Dowling, N.E., *Mechanical Behaviour of Materials. Engineering Methods for Deformation, Fatigue and Fracture*. 3rd ed. 2006: Prentice-Hall.
55. Callister, W.D., *Materials Science and Engineering: An Introduction*. 7th ed. 2007: John Wiley & Sons.

56. Davis, J.R., *Corrosion of Aluminum and Aluminum Alloys*. 1999: ASM International. 313.
57. Wang, Q.Y., N. Kawagoishi, and Q. Chen, *Effect of pitting corrosion on very high cycle fatigue behavior.* Scripta Materialia, 2003. 49(7): p. 711-716.
58. Hoeppner, D.W., *Model for Production of Fatigue lives based upon a pitting corrosion fatigue process*, in *Fatigue Mechnisms*, J.T. Tong, Editor. 1979, ASTM: Philidelphia, Pa.
59. Golden, P.J., A.F. Grandt, and G.H. Bray, *A comparison of fatigue crack formation at holes in 2024-T3 and 2524-T3 aluminum alloy specimens.* International Journal of Fatigue, 1999. 21(Supplement 1): p. 211-219.
60. Menzemer, C. and T.S. Srivatsan, *The effect of environment on fatigue crack growth behavior of aluminum alloy 5456.* Materials Science and Engineering a-Structural Materials Properties Microstructure and Processing, 1999. 271(1-2): p. 188-195.
61. Wei, R.P., *A model for particle-induced pit growth in aluminum alloys.* Scripta Materialia, 2001. 44(11): p. 2647-2652.
62. Pao, P.S., S.J. Gill, and C.R. Feng, *On fatigue crack initiation from corrosion pits in 7075-T7351 aluminum alloy.* Scripta Materialia, 2000. 43(5): p. 391-396.
63. Sankaran, K.K., R. Perez, and K.V. Jata, *Effects of pitting corrosion on the fatigue behavior of aluminum alloy 7075-T6: modeling and experimental studies.* Materials Science and Engineering A, 2001. 297(1-2): p. 223-229.
64. DuQuesnay, D.L., P.R. Underhill, and H.J. Britt, *Fatigue crack growth from corrosion damage in 7075-T6511 aluminium alloy under aircraft loading.* International Journal of Fatigue, 2003. 25(5): p. 371-377.
65. Dolley, E.J., B. Lee, and R.P. Wei, *The effect of pitting corrosion on fatigue life.* Fatigue & Fracture of Engineering Materials & Structures, 2000. 23(7): p. 555-560.
66. Jones, K., et al., *Effect of prior corrosion on short crack behavior in 2024-T3 aluminum alloy.* Corrosion Science, 2008. 50(9): p. 2588-2595.
67. Buchheit, R.G., et al., *The electrochemistry of intermetallic particles and localized corrosion in Al alloys.* Jom-Journal of the Minerals Metals & Materials Society, 2001. 53(7): p. 29-+.
68. Winsley, R. *Evaluation of the corrosion resistance of FSW AA5083-H116*. Phd Thesis, 2006. University of Birmingham.
69. ASTM Standard Designation G67-04 Standard Test Method for Determining the Susceptibility to Intergranular Corrosion of 5XXX Series Aluminum Alloys by Mass Loss After Exposure to Nitric Acid (NAMLT Test). ASTM International, 2004.
70. ASTM Standard Designation G46-97 (reapproved 2005) Standard Guide for Examination and Evaluation of Pitting Corrosion. ASTM International, 2005.